FACULTY OF SCIENCE
UNIVERSITY OF COPENHAGEN

A Chebyshev-Bogoliubov-de Gennes Approach to Quasiparticle Interference in the Nematic Phase of FeSe

Master's Thesis in Physics.
Niels Bohr Institute,
University of Copenhagen

Johannes H. J. Martiny
wgd717@alumni.ku.dk

Supervisor: Brian M. Andersen

Date: 30/08-2016

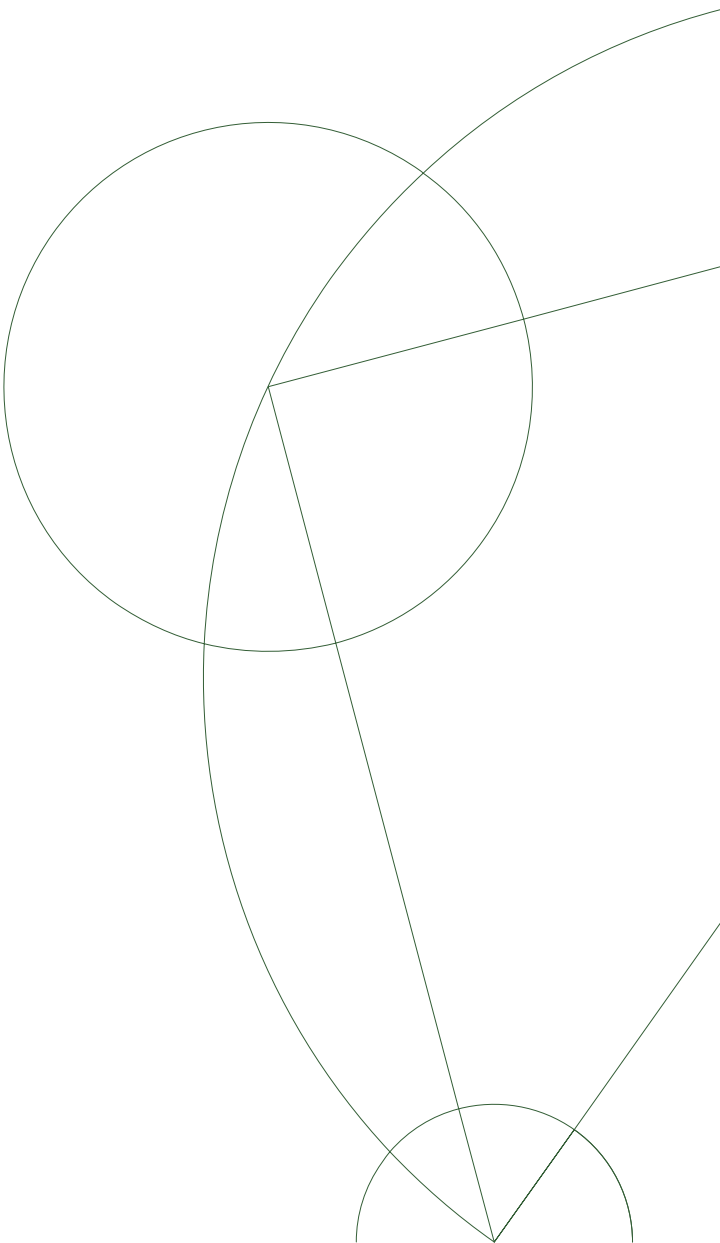

Abstract

The family of iron based superconductors hosts a narrow nematic phase of broken rotational symmetry at high temperatures. The proposed electronic origin of this phase is intimately linked to the unconventional properties of the low temperature magnetic and superconducting states. The structurally simple compound iron selenide (FeSe), which enables the study of the nematic phase due to the absence of long range magnetic order, has demonstrated highly anisotropic features in STM experiments thought to arise from quasiparticle interference (QPI).

In this master's thesis we investigate these features using a band structure model for the nematic phase of FeSe including an orbital order component, yielding non-degenerate d_{xz} and d_{yz} orbitals. We perform selfconsistent calculations of the local density of states (LDOS) on a lattice including a central impurity, thereby generating QPI features. This is accomplished using the Chebyshev-Bogoliubov-de Gennes method which enables the study of large lattices in finite time, and is here proven applicable to the study of QPI.

The obtained unidirectional QPI features can be mapped directly to nested scattering vectors of the C_2 symmetric Fermi surface pockets in the nematic phase, and mirror the experimental result under the additional assumption of orbitally selective scattering. Attempting to generate such selectivity in the impurity potential itself by including the effect of local magnetic order nucleated on the central impurity, we find that the effective scattering potential remains isotropic in the orbital basis, and that scattering from this potential yields QPI features inconsistent with experiment. This indicates that such a local order is not nucleated in FeSe. We propose that the orbital selectivity is instead generated by correlation induced lifting of the orbitally resolved quasiparticle weight degeneracy, which follows naturally from orbital order in the nematic phase.

Acknowledgements

First of all I would like to thank Brian for guidance on the direction of the project, good discussions on all things QPI, and for always being able to conjure a relevant review out of thin air.
I would also like to thank Astrid, Daniel, Maria and Morten of the High-Tc group, with a special thank you to Andreas Kreisel for answering countless band structure questions and for providing critical feedback on my results.
I have been aided greatly by correspondence with Peter S. Sprau, J.C. Seamus Davis, and Peter J. Hirschfeld.
A final thank you goes to the members of the CMT lunch club for providing an enjoyable break each and every day.

Contents

Chapter 1

Introduction to Iron Based Superconductors

1.1 Unconventional Superconductivity

The phenomenom known as superconductivity was first observed as an unexpected complete resistivity supression at a critical temperature (T_c) by Kammerlingh Onnes in 1911 [1], as evident in Figure 1.1 **(a)**. A consistent theory of the resistivity drop and concurrent magnetic flux repulsion was developed by Bardeen, Cooper and Schrieffer in 1957 [2], describing the formation of coherent electron (Cooper) pairs with opposite spin and momenta. The pairing 'glue' of this Cooper instability in the conventional case is the electron-phonon interaction, yielding an effective electron-electron (Coulomb) interaction with an attractive component [3, p. 7]

$$V_{eff}(q,\omega) = \frac{4\pi e^2}{q^2 + k_{TF}^2} + \frac{4\pi e^2}{q^2 + k_{TF}^2}\frac{\omega_q^2}{\omega^2 - \omega_q^2}. \tag{1.1}$$

The first part of this expression is the usual screened Coulomb interaction with the Thomas-Fermi screening length $\lambda_{TF} = k_{TF}^{-1}$ on the order of a few lattice constants [3], while the second (also shortranged) part is due to the electron-phonon interaction with acoustic phonons of linear dispersion $\omega_q \propto q$, and is attractive in a range $|\omega| < \omega_q \leq \omega_D$ set by the Debye frequency. In real space this interaction is the result of bypassing electrons shifting the slow moving ions of the lattice, creating an attractive region for other electrons. Due to the larger mass of the ions, other electron can take advantage of this region within the ion relaxation time. This creates a net attractive interaction between electrons at the same position but at shifted (retarded) times. The resulting Cooper pair must then be in an s-wave (even) pair state (to accomodate the similar position) and is then spin singlet (odd) due to fermion antisymmetry [4]. Disorder in the crystal lattice resulting in local scattering centers still allow the pair formation and only weakly suppresses the superconductivity. Magnetic impurities, on the other hand, break the single pairs and destroy superconductivity in small concentrations.

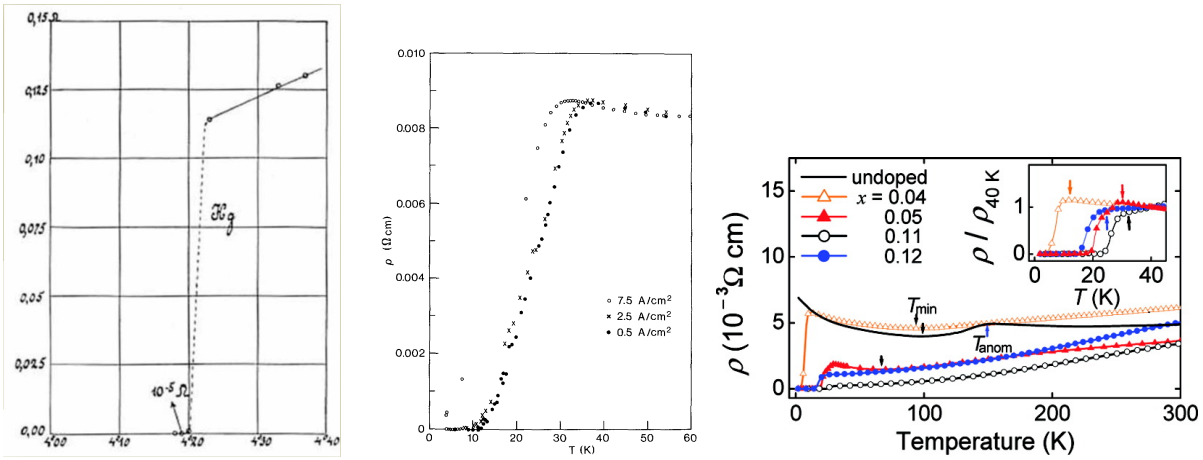

(a) Hg (b) $Ba_xLa_{5-x}Cu_5O_5$ (c) $LaO_{1-x}F_xFeAs$

Figure 1.1: Experimental resistivity curves displaying the transition to superconductivity at low temperatures, for three different families of superconductors. **(a)** Onnes initial discovery of superconductivity in mercury [5]. **(b)** Copper based superconductivity [6]. **(c)** The first demonstration of high T_c iron based superconductivity [7]. The inset shows the relative resistivity $\rho(T)/\rho(T = 40\text{K})$ at the SC transition for different values of the fluorine doping fraction.

Central to BCS theory is the emergence of (Bogoliubov) quasiparticles which are superpositions of electrons and holes with energies $E_k = \sqrt{\xi_k^2 + \Delta^2}$, with Δ the superconducting gap. The spectrum thus has an excitation gap of magnitude 2Δ, which disappears at the critical temperature, i.e. $\Delta(T_c) = 0$. Given an attractive pairing potential g with an effective cut-off $\epsilon_c = \omega_D$ we can then extract the critical temperaturee of SC instability from the lineralized BCS gap equation [3]

$$1 = -gN_0 \int_{-\epsilon_c}^{\epsilon_c} \frac{\mathrm{d}\xi}{\xi} \tanh\left(\frac{\xi}{2k_BT_c}\right) \tag{1.2}$$

$$= -gN_0 \ln\left(\frac{1.14\epsilon_c}{k_BT_c}\right), \tag{1.3}$$

with N_0 the density of states at the Fermi level, whence $k_BT_c = 1.14\epsilon_c e^{-1/|g|N_0}$.

BCS theory with electron-phonon interaction as the pairing glue proved capable of describing a multitude of superconducting materials. However, later discoveries of other superconducting compounds, including the superfluid helium 3 and the class of heavy fermion compounds containing rare earth elements were inconsistent with the s-wave electron-phonon pairing scenario. An interesting example is the class of copper based materials or "cuprates". The undoped compounds, containing quasi-2d Cu based planes and various spacer layers, are Mott insulators, i.e. the electrons are localized due to strong correlation effects. Superconductivity in these materials, emerging upon electron or hole doping, proved inconsistent with the electron-phonon

pairing mechanism since the electron-phonon interaction strength in these materials are insufficient to yield the very high T_c within BCS theory. Additionally, the gap symmetry (of Δ_k) is by now well-established as d-wave (more on this later) indicating a novel pairing mechanism [4].

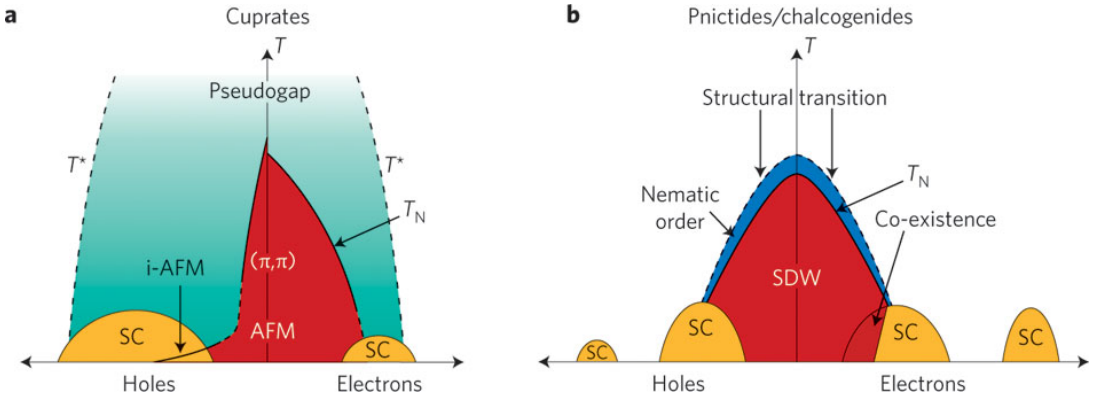

Figure 1.2: Typical phase diagrams for the cuprates and the FeSCs. In both families the superconducting emerges from the magnetically ordered state upon electron of hole doping. Reproduced from [8].

1.2 The Iron Based Superconductors

The iron based superconductors (FeSC) were first discovered in 2008 by Kamihara et al. [7] in fluoride doped LaOFeAs ($LaO_{1-x}F_xFeAs$). It should be noted that the discovery was not of superconductivity in iron, which has long been known to be superconducting at very low temperatures in a manner consistent with conventional BCS theory, but the discovery of two families of superconductors based on the structural parent compounds FeAs (the pnictides) or FeSe (the chalcogenides) with critical temperatures rivaling the cuprates. These new materials consist of stacked "planes"; trilayers with the selenium or arsenic ions placed above and below an iron square lattice in an alternating pattern as shown for different compounds in Fig. 1.3 **(a)**. Similarly to the cuprates, several other elements can be inserted in spacer layers in between these Fe(As/Se) layers forming new superconducting compounds. The highest T_c for bulk compounds in each family is found in such constructions, with the extremal value found in the fluorine doped pnictide SmFeAsO ($T_c = 56$K).

The usual description of the FeSC band structure is to construct a 3-D or 2-D model using density functional theory (DFT), deriving effective hopping integrals for a tight binding model of the Fe-Fe square lattice. The true unit cell of the planes of Fe(Se/As) is displayed in 1.3 **(b)** and contains two irons, as the out of plane element is staggered above and below the square lattice. It is common to create band structure models in the 1Fe unit cell instead, as the spectral weight at the Fermi surface consists of the $3d$ orbitals of the Fe lattice. The Brillouin zone (B.Z.) associated with this 1Fe unit cell is shown in Figure 1.3 **(c)**. The shared properties of all FeSCs

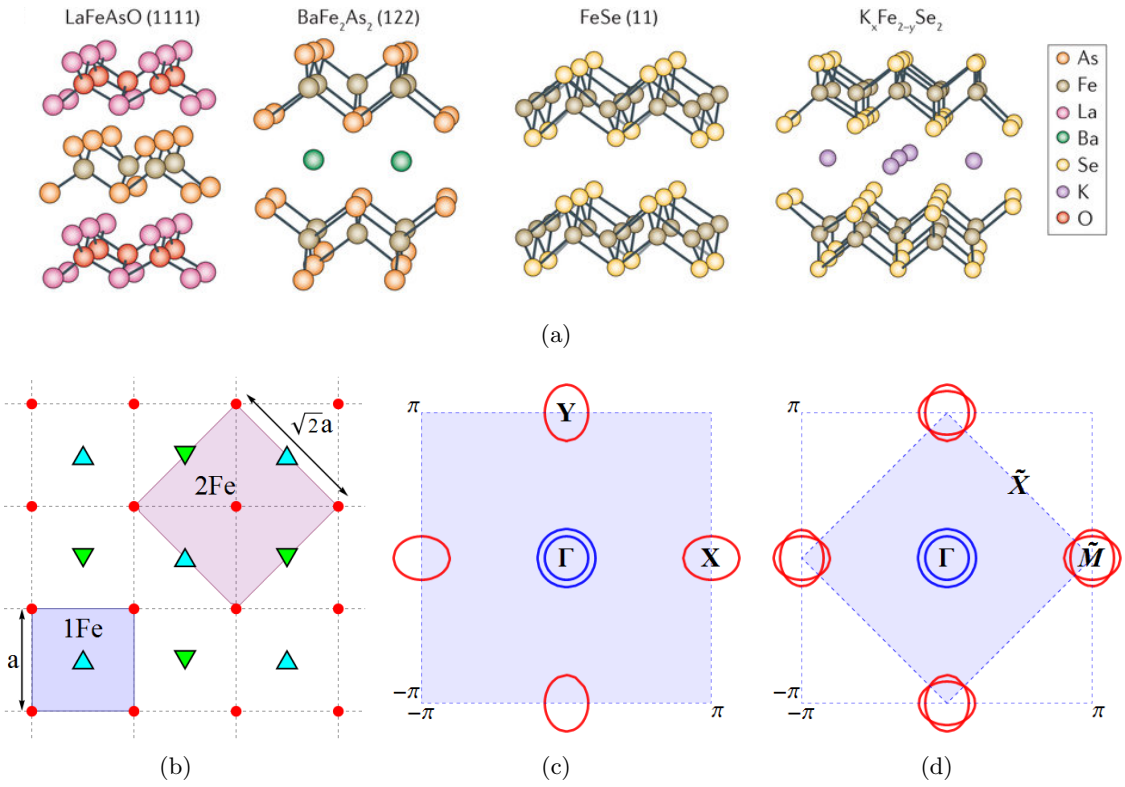

Figure 1.3: **(a)** A selection of iron based superconductors. Reproduced from [9]. **(b)** Structure of the Fe(As/Se) planes with the Fe lattice as red points. The 1Fe unit cell (shaded blue) fails to account for the out of planes elements. The true unit cell (shaded purple) contains 2Fe atoms, accounting for the staggered As/Se atoms above (cyan triangles) and below (green triangles) the square lattice. **(c)** The unfolded B.Z. corresponding to the 1Fe unit cell with hole pockets at the central Γ point and electron pockets at the X and Y points. **(d)** The folded B.Z. corresponding to the 2Fe unit cell. The folding vector (π, π) connects the old X and Y points, creating the "propeller" formation.

is a metallic band structure with one or more hole pockets at the center and electron pockets at the X and Y points. Corresponding to the 2Fe extension of the unit cell, the B.Z. is reduced in size and folds into the structure seen in Figure **(d)**. The (π, π) folding maps the X and Y points on to each other, creating propeller-like formations of the elliptical pockets. In order to promote correspondence with other simpler lattice models, ordering vectors of different phases are usually given in the notation of the 1Fe unit cell [10].

At high temperatures the FeSC are essentially correlated or "bad" metals characterized by a short mean free path, as evident in large electrical resistivities much larger than for a typical "good" metal such as chromium [9]. This bad metal behaviour is a sign of strong electron-electron correlation effects on the order of the electronic bandwidth. Tuning the ratio of these energy scales covers the limits of strong correlation inducing the Mott localized (and

thus insulating) state and weak correlations yielding delocalized or *itinerant* behavior, with the FeSC at various points inbetween. This tuning can be accomplished by reducing the bandwidth by simply increasing the iron-iron distance in the conducting planes by introducing new spacer layers. Such substitution has shown Mott localized behavior in the iron chalcogenides [9].

It is with this correlated yet itinerant picture in mind that we now turn to the low temperature phase diagram, as shown in Figure 1.2 **(b)**. The first phase transition of a prototypical compound is the structural transition into a nematic state with broken rotational symmetry, from tetragonal C_4 to orthorhombic C_2. The physical lattice parameter anisotropy is very small, with the two iron-iron lattice axes related by $a \approx 1.003b$. In most compounds a spin density wave (SDW) state emerges just below this structural transition. Upon electron or hole doping, or pressurizing the system, these initial phases decay in a dome-like fashion and reveal domes of superconductivity in competition with the magnetic phase and allowing a possible coexistence phase.

It is worth highlighting the similarity to the cuprates. In both families the superconducting state emerges upon electron or hole doping of the magnetically ordered parent compound, in cuprates from the antiferromagnetically ordered Mott insulating state and in the FeSC from a spin density wave (SDW) state. The doping or pressure phase diagram is also similar with emerging domes of superconductivity. The major differences is in the strength of the correlations, with strong correlations inducing the Mott localized insulating behavior in the cuprates and smaller correlations yielding itinerant bad metal behavior in the FeSCs, and also in the orbital degree of freedom which plays a major role in FeSC impurity physics.

1.2.1 Model of the magnetic phase

With intermediate correlation effects established as the starting point for modeling the FeSCs, the question arises of how to treat the ordered spins in the magnetic phase. We describe the ordering by the ordering vector(s) $\mathbf{Q}$, i.e. we write the magnetization

$$\boldsymbol{m}(\boldsymbol{r}) = \sum_i \boldsymbol{m}_i e^{i\boldsymbol{Q}_i \cdot \boldsymbol{r}}, \tag{1.4}$$

and refer to the phases simple by the dominant ordering vector (single-Q order) or multiple ordering vectors (double-Q order, etc.).
Correlation effects are usually described by the Hubbard model

$$H_{\text{Hubbard}} = -t \sum_{\langle ij \rangle, \sigma} c^\dagger_{i\sigma} c_{j\sigma} + U \sum_i \hat{n}_{i\uparrow} \hat{n}_{i\downarrow} \tag{1.5}$$

with $\hat{n}_i = c^\dagger_i c_i$ indicating the number operator on site i, the exchange integral U setting the repulsive interaction between spins on the same lattice site, and the ratio U/W of the Hubbard U and the electronic bandwidth setting the degree of correlation.
However, in the regime of strong correlations the electrons are localized and only retain spin

degrees of freedom, captured by the Heisenberg model

$$H_{\text{Heisenberg}} = -\sum_{\langle\langle ij\rangle\rangle} J_{ij}\boldsymbol{S}_i \cdot \boldsymbol{S}_j \tag{1.6}$$

with $\boldsymbol{S}_i = \sum_{\sigma\sigma'} c^\dagger_{i\sigma}\boldsymbol{\tau}_{\sigma,\sigma'}c_{i\sigma'}$, $\boldsymbol{\tau} = (\tau^1, \tau^2, \tau^3)$ being the vector of Pauli matrices, and with nearest and next nearest neighbor interactions J_{ij}. This model describes purely localized spins on a lattice but is also capable of reproducing the observed magnetic phases if the localization is relaxed by adding a tight binding term as above, resulting in a so called $t - J$ model.
Although most magnetic phases can be produced in variants of the above Heisenberg model, including mixed models with local moments and itinerant electrons, the metallic nature of the FeSCs favors the purely itinerant approach of the Hubbard model. The recent discovery of the superposition of stripe orders (double-Q phase) also favors this interpretation, as this magnetic structure emerges naturally from itinerant models [11].
The inclusion of the Hubbard U renormalizes the bare spin susceptibility (spin-spin correlation function), with the simple random phase approximation form

$$\chi(\boldsymbol{q},\omega) = \frac{\chi^0(\boldsymbol{q},\omega)}{1 - U\chi^0(\boldsymbol{q},\omega)} \tag{1.7}$$

with χ^0 the bare susceptibility (Lindhard function). This function has a clear divergence at Stoner transition, $U\chi^0(0) = 1$, leading to a ferromagnetically ordered state within linear response theory. Below this critical point, $U\chi^0(0) < 1$, the bare susceptibility is enhanced and a spin ordered state emerges at low temperature with momentum structure given by the dominant contribution to the Lindhard function

$$\chi^0(\boldsymbol{q},\omega) \propto \sum_{\boldsymbol{k}} \frac{f(\epsilon_{\boldsymbol{k}}) - f(\epsilon_{\boldsymbol{k}+\boldsymbol{q}})}{\omega + i\eta + \epsilon_{\boldsymbol{k}} - \epsilon_{\boldsymbol{k}+\boldsymbol{q}}}. \tag{1.8}$$

This expression is dominated by contributions where $\epsilon_{\boldsymbol{k}} \approx -\epsilon_{\boldsymbol{k}+\boldsymbol{q}}$ and thus involves regions of the Fermi surface where $\epsilon_{\boldsymbol{k}} \approx -\epsilon_{\boldsymbol{k}+\boldsymbol{Q}}$ for some nonzero $\boldsymbol{Q}$. We refer to this requirement as the nesting condition, with the nesting vector Q indicating the ordering vector of the spin density wave state. In this picture the possible ordered states can be derived by simply scanning the Fermi surface for vectors connecting parallel regions. We note that the model of equation 1.5 describes the simple 1 band case, which is insufficient in the fundamentally multiorbital FeSCs. When multiple orbitals are included the model expands to include intra orbital repulsion U', Hund's rule coupling J and the so called "pair-hopping" term J'. We will study this model extensively in later chapters.

The typical FeSC Fermi surface and primary nesting vectors are indicated schematically in Figure 1.4 **(a)**. We will focus on compounds with dominant nesting vectors of $(\pi, 0)$ and $(0, \pi)$ leading to a spontaneous C_4 symmetry breaking as we lower the temperature in the absence of any preceding nematicity, choosing one nesting vector and entering a 'stripe' phase. This phase is characterized by ferromagnetic alignment along one Fe-lattice axis and antiferromagnetic alignment along the other, as shown for $(\pi, 0)$ ordering in Figure 1.4 **(b)**. The preceding

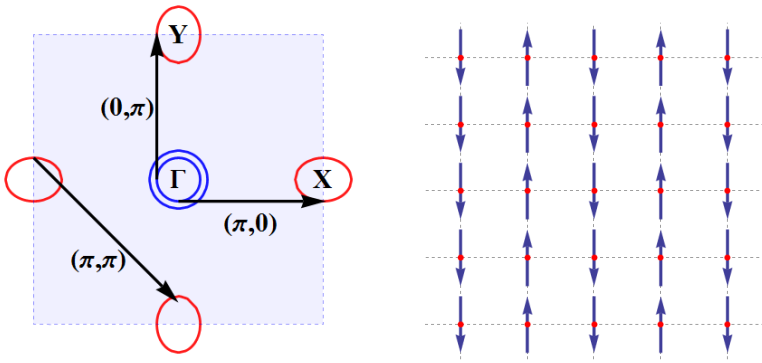

(a) (b)

Figure 1.4: **(a)** Unfolded FS with nesting arrows. **(b)** Magnetic structure in the stripe phase with ordering vector $\mathbf{Q} = (\pi, 0)$ on the Fe-Fe lattice.

nematic transition breaks the Fermi surface C_4 symmetry, thus choosing one of these ordering vectors over the other by increasing the nested Fermi surface region.

1.2.2 Gap symmetry

Moving into the superconducting phase we consider the generalized BCS gap equation, here shown for a single band system [10]

$$\Delta_{\boldsymbol{k}} = -\sum_{\boldsymbol{k}'} \Gamma(\boldsymbol{k}, \boldsymbol{k}') \frac{\Delta_{\boldsymbol{k}'}}{2E_{\boldsymbol{k}'}} \tanh\left(\frac{E_{\boldsymbol{k}'}}{2T}\right), \tag{1.9}$$

with $E_k = \sqrt{\epsilon_k^2 + \Delta_k^2}$, ϵ_k describing the bare band H^0, and Γ some interaction.
Setting $\Gamma(k, k')$ constant as above, the simplest solution is an isotropic gap $\Delta_{\boldsymbol{k}} = \Delta_0$, provided that the interaction is attractive, thus canceling the sign. However, an interaction peaked at some nonzero wave vector $\Gamma(\boldsymbol{k}, \boldsymbol{k}') \to \delta(\boldsymbol{k}, \boldsymbol{k} + \boldsymbol{Q})$ allows solution with a repulsive interaction provided the gap changes sign over the Fermi surface, i.e. $\Delta_{\boldsymbol{k}} = -\Delta_{\boldsymbol{k}+\boldsymbol{Q}}$. Within spin fluctuation theory such an interaction can be realized for a Fermi surface with parallel regions connected by some nesting vector $\boldsymbol{Q}$, leading to a divergence of the spin susceptibility and associated pairing interaction at this wave vector.
An example of such a gap structure is the d-wave solution with nonzero angular momentum ($l = 2$) induced by (π, π) nesting. This state is characterized by the line nodes in the gap function ($\Delta(\boldsymbol{k}, \pm\boldsymbol{k}) = 0$) required by the gap sign change. This nonzero angular momentum solution can be intuitively understood as electrons forming orbits to avoid close-ranged Coulomb repulsion.

The allowed gap structures get more complicated when multiple bands cross the Fermi level, forming distinct Fermi surface pockets such as is the case in the FeSCs. The typical Fermi surface consisting of central hole pockets and electron pockets at the X and Y points is shown in

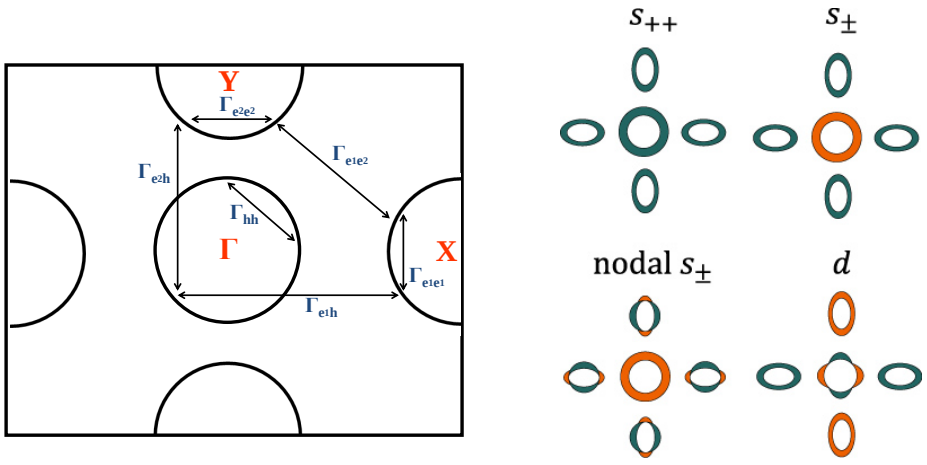

(a) (b)

Figure 1.5: **(a)** FS nesting and pairing interactions. **(b)** Proposed gap symmetries for the FeSC's. Reproduced from [12] and [10], respectively.

Fig. 1.5. In general a multi-band system will have a gap equation for each band containing intra and interpocket interactions $\Gamma^{\alpha\beta}$. The above nesting condition combined with the sign change will allow different solutions based on the dominant interaction. Dominant interactions between the electron pockets nested by (π, π) will naturally lead to d-wave solution while pairing interactions between hole and electron pockets nested by $(\pi, 0)$ or $(0, \pi)$ naturally favor s-wave solutions. An attractive interaction in this channel yields the usual s-wave isotropic solution, while a repulsive interaction forces a sign change of the gap function between hole and electron pockets. To account for this we label these as s^{++} and s^{+-}, respectively. The s^{+-} solution is predicted within spin fluctuation theory, yet other pairing mechanisms based on e.g. orbital fluctuations prefer the isotropic s^{++} solution, see e.g. Hirschfeld [13]. In terms of the multi-orbital Hubbard-Hund model mentioned above, orbital fluctuation mediated pairing is favored when the intra-orbital interaction set by U' is somehow enhanced.

Depending on the details of the intra and interband interactions, the sign changing s^{+-} gap structure may host nodes on the Fermi surface pockets. These nodes are deemed "accidental" in the sense that they are not mandated by symmetry as in the d-wave solution of the cuprates, and can be created or destroyed with pressure or doping with no associated phase transition [13]. An example of such a solution is given in the bottom left panel of Figure 1.5. We note that the d-wave solution should be favored in the extremely electron doped system with no central hole pockets, as the $(\pi, 0)$ nesting is absent, leaving only the (π, π) nesting of the electron pockets.

1.2.3 Nematic transition

It should be clear at this point that the initial C_4 to C_2 crystal symmetry reduction is intimately linked to the SDW and SC transitions. In the above phase diagram in Figure 1.3 **(b)**, the nematic region is seen to preempt and closely follow the SDW transition in the dome of doping behavior. This region is characterized by a large resistivity anisotropy [9] which is much larger than expected from the small anisotropy of the lattice parameters. This led to the hypothesis that the orthorhombic transition is driven by the electronic rather than lattice degrees of freedom (phonons).

Testing this hypothesis, Chu et al. [14] probed the nematic response to an applied strain in crystal samples of $Ba(Fe_{1-x}Co_x)_2As_2$ by gluing the sample to a piezostack controlled by an applied voltage. Defining a nematic order parameter by the relative resistivity along the direction of strain and $\eta = (\rho_b - \rho_a)/(\rho_a + \rho_b)$, a nematic susceptibility can be calculated as the derivative with respect to the strain $\epsilon = \Delta L/L$, as $\frac{d\eta}{d\epsilon}$. The measured nematic order parameter as a function of temperature and the associated susceptibility are plotted in Figure 1.6 **(a)-(b)**, revealing a diverging nematic susceptibility as we approach the structural instability from above. The $\frac{1}{T}$ Curie-Weiss like dependence is consistent with the prediction of a Ginzburg-Landau free energy consideration for an electronically driven phase transition, and not the constant dependence predicted based on a structural instability. The full calculation is too extensive to reproduce here, and we refer to the supplemental of [14]. Supporting this argument is the fact that the nematic transition follows the SDW dome in the phase diagram, indicating that a shared degree of freedom is responsible for both transitions [15].
We can then conclude that the structural transition is driven by the electronic and not the lattice degrees of freedom, and refer to the behaviour below T_s as "electronic nematic".

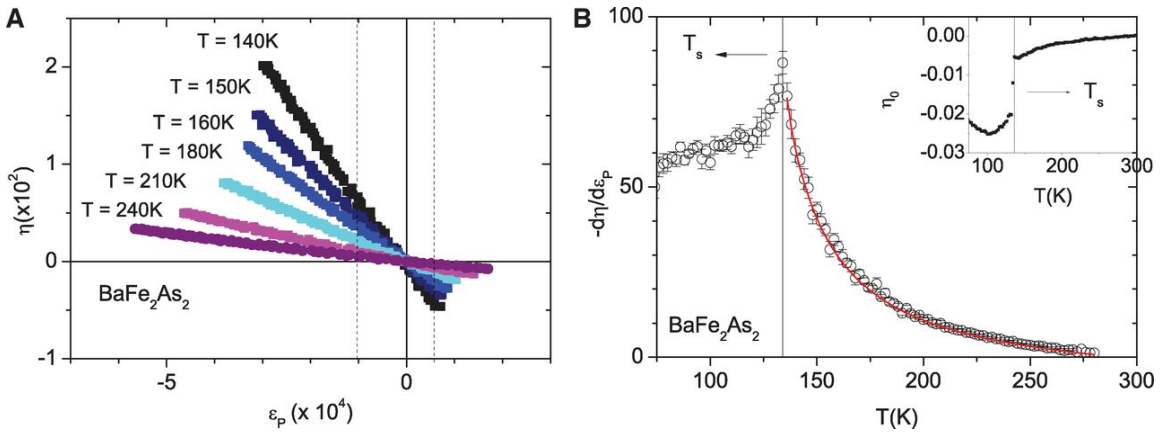

Figure 1.6: **(a)** The nematic order parameter as a function of strain at different temperatures above T_s, obtained through resistivity measurements under uniaxial strain. **(b)** Temperature dependence of the nematic susceptibility demonstrating a divergence as we approach T_s. Figures reproduced from [14].

The concept of electronic nematicity indicates a shared driving mechanism establishing mag-

netism and superconductivity, and the open question in then whether orbital or spin fluctuations are dominant. Orbital order is the result of divergent charge fluctuations resulting in different occupations of the d_{xz} and d_{yz} orbitals ($n_{xz} \neq n_{yz}$), while the spin-nematic scenario is the spontaneous symmetry breaking between $\boldsymbol{Q}_x = (\pi, 0)$ and $\boldsymbol{Q}_x = (0, \pi)$ ordering vectors in the dynamic spin suceptibility, a precursor for the stripe state. We note that these properties are connected since orbital order induces spin anistrophy and vice versa, and the associated order parameters are both nonzero in the nematic phase. Predicting the driving fluctuation is then a "chicken and egg" like problem [16]. An argument for the "spin-nematic" scenario is again the close correspondence between the SDW and nematic phases as a function of doping observed in multiple FeSCs [16]. This question is of paramount importance in relation to the pairing symmetry, where orbital fluctuations predict the s^{++} pairing state while spin fluctuations predict the s^{+-} (or, in some situations, the $d_{x^2-y^2}$) state [16]. Identifying the driving mechanism of the nematic transition thus provides a pathway to the understanding the spin density wave and superconducting phases of the FeSCs.

1.3 FeSe

Being the structural base for all iron chalcogenide superconductors, iron selenide (FeSe) could reasonably be expected to share most of their properties, yet for this compound the transition to a long ranged magnetic order is notably absent. The nematic transition from the high T tetragonal to low T orthorhombic phase is still present, but no spin density wave state manifests as the temperature is decreased. Lacking the competition with a preeminent magnetic phase, the superconducting dome has a tail at zero doping with a critical temperature $T_c \approx 8$K. The lack of a magnetically ordered phase enables studies of the entire nematic phase diagram, and allows experiment to probe the nematicity-superconductivity phase transition in the undoped compound.

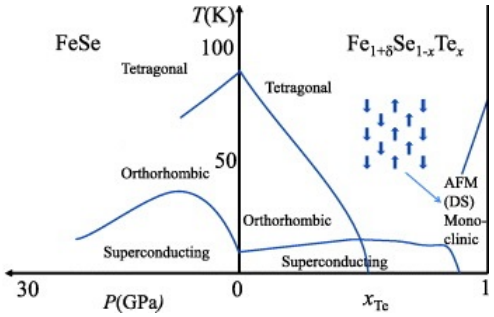

Figure 1.7: The phase diagram of FeSe showing the evolution with pressure and Te doping. The usual magnetic phase of the FeSCs is absent, allowing for superconductivity in the parent compound. Reproduced from [17].

The absence of SDW order in an FeSC would at first sight seem incompatible with the spin-nematic scenario described above, as we would expect the driving spin fluctuation to induce

magnetic order at some finite temperature. A recent inelastic nuclear scattering experiment, directly probing the spectral weight of the dynamic spin susceptibility, demonstrated large stripe spin fluctuations in the nematic state ($T = 11$K [18]). Scanning the temperature axis, the experiment revealed stripe fluctuations in the tetragonal phase ($T = 110$K) which are enhanced when crossing the structural transition, closely mirroring the degree of orthorhombicity. This close connection between spin fluctuations and nematicity is a clear indication of the spin-nematic scenario. Theoretical models based on bands obtained from DFT indicate that the lack or long range spin order is instead the result of frustration [19], i.e. the close competition between the different ordering vectors precludes any one order from being established. The structural transition favors one of these stripe orders, relaxing the frustration and accounting for the observed enhancement [18].

It must be emphasized that the absence of the SDW phase does not constitute the only reason to study FeSe, which displays several unconventional phenomena. The initial modest T_c of 8K rises to $\approx$ 40K with ion intercalation or pressure, and single layer FeSe deposited on $SrTiO_3$ reaches an extreme critical temperature of $\approx$ 100K. Additionally, as we shall see, several experiments probing the local density of states have revealed long range and highly anisotropic features thought to arise from quasiparticle interference. Investigations into the origin and the interpretation of these features and their relation to the nematic phase will be the main subject of this thesis, and we will present the experimental details and the precise nature of these effects in the following chapter.

1.4 Thesis Outline

In this thesis we will study oscillations in the local density of states arising from the interference of quasiparticles (QPI) in the nematic phase of FeSe. We will introduce this concept in **Chapter 2**, where we also present highly anisotropic features seen in scanning tunneling microscopy in this material. We will attempt to reproduce these QPI features by a real space selfconsistent method for the local density of states, which is the subject of **Chapter 3**, where we introduce the Chebyshev-Bogoliubov-de Gennes method. We then motivate our choice of tight binding model for FeSe in the nematic phase in **Chapter 4**.
With these two components in place we can calculate theoretical QPI spectra, which we will compare to experiment in **Chapter 5**. Here we will also introduce the concept of orbitally selective scattering as a means of reproducing the experimental data from our model.
In the rest of the thesis we will try to induce such scattering, initially by locally nucleating local magnetic order in **Chapter 6** so as to induce an effective impurity potential which is anisotropic in the orbital basis. QPI features from scattering on such a potential is then investigated in **Chapter 7**, where we find large discrepancies with experiment. This leads us to consider orbital selectivity from the quasiparticles themselves, by investigating the orbital components of the quasiparticle weight in **Chapter 8**.

Chapter 2

Friedel Oscillations from Impurity Scattering

Disorder is an inherent property of all bulk crystal structures. The addition of extra atoms in-between the regular structure (add-atoms), the vacancy of a lattice site, or the replacement of unintended elements due to outside contamination all eliminate the perfect crystal favored by theorists. Yet these oftentimes undetermined contaminants can also provide new information about the properties of the clean system, e.g. in superconductors where the tuning of magnetic and non-magnetic impurity concentrations yield gap suppression rates which, when modeled by Abrikosov-Gorkov theory, can be used to extract the symmetry of the gap function.
Apart from modifying the bulk properties of the solid in large concentrations, single impurities also modify the local system close to their interstitial or lattice site. The main local probe of such properties is the scanning tunneling microscope (STM). In this chapter we will investigate the modulation of the local density of states measured by the STM, and introduce the highly anisotropic features observed in recent FeSe experiments.

2.1 Tunneling Spectroscopy as a Local Probe of Disorder

The experimental setup for the STM consists of a sharp metal tip scanning across a cleaved layer of the material with an applied bias between tip and sample as shown in figure 2.1 **(a)**. A linear response calculation for the tunneling current induced by the applied voltage yields [20]

$$I = \int_{-\infty}^{\infty} \mathrm{d}\omega \sum_{\nu\mu} T_{\nu\mu} A_1(\nu,\omega) A_2(\mu,\omega+eV)(f(\omega+eV) - f(\omega)), \tag{2.1}$$

with A_1 the local density of states of the probed material, A_2 the LDOS of the tip, eV the energy of a single electron with charge e in the potential V, and $f(\omega) = (1+e^{\omega/k_BT})^{-1}$ the Fermi-Dirac distribution.
If we choose a metallic system with a continuum of states as the second material we can

approximate $\sum_\mu T_{\mu\nu} A_2(\mu, \omega + eV) \approx$ constant and the differential conductance becomes

$$\frac{dI}{dV} \propto \int_{-\infty}^{\infty} \mathrm{d}\omega \left(-\frac{\partial f(\omega + eV)}{\partial \omega} \right) \sum_\nu A_1(\nu, \omega) \tag{2.2}$$

$$\approx \sum_\nu A_1(\nu, -eV), \tag{2.3}$$

valid at low temperatures where the Fermi function tends to a step function (with a delta function derivative). The differential conductance extracted from measurements of the tunneling current during voltage sweeps thus yields the local density of states of the substrate. This procedure is shown in 2.1 **(b-e)**.

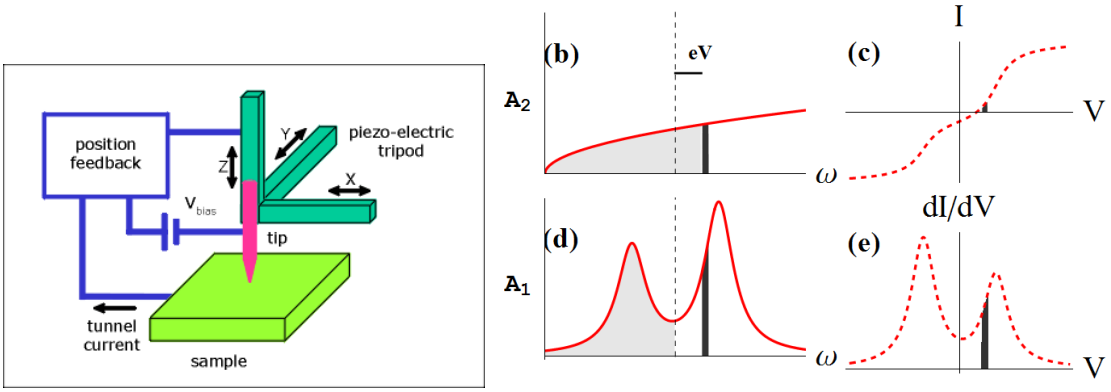

Figure 2.1: **(a)** Typical experimental setup for the STM. Reproduced and lightly edited from [21]. **(b,d)** Representative density of states for the tip metal (A_2) and some arbitrary sample (A_1). The metal LDOS can be approximated constant in small intervals such as the shaded region. The dotted line indicates the Fermi level of the sample. An applied bias shifts the electrochemical potential of the metal by eV. **(c)** Tunneling current as a function of bias obtained as the area under the graph in **(d)**, i.e. the integrated LDOS. **(e)** Differential conductance from the above current. Under the constant LDOS approximation for the metal, this quantity directly images the sample LDOS. **(b-e)** Inspired by the corresponding figure in [20].

The STM can be run in two major modes, either keeping the distance between substrate and the STM tip fixed and sweeping the voltage in order to obtain the local density of states at given energies, or by allowing the height to vary and keeping the voltage fixed, enforcing a constant current by a feedback loop. The resulting image of the tip height is called a topograph. The height is proportional to the charge density, since the constant current is proportional to the integrated density of states $\int_0^{eV} A(r, \omega)\, \mathrm{d}\omega$. This method attains atomic resolution, directly imaging the lattice on surface or cleaved layers.

2.2 Friedel Oscillations from Lattice Impurities

We now turn to the disordered system, and consider the STM obtained around a single impurity. From the above argument we naturally expect to see a charge modulation induced by the impurity, breaking the previously translational symmetry in the topograph. This large charge modulation is mostly contained to the nearest neighbor sites, which screen the charge excess or decrease on the central impurity site. However, a new feature is the appearance of long range interference patterns in the charge density, stemming from scattering on the impurity site. These modulations are also present in the differential conductance, i.e. the LDOS. We are interested in the structure of this LDOS modulation.
Let us consider a 1D system with an incoming wave $e^{ik_F x}$ [22]. Upon scattering the wave function is a superposition of incident and reflected wave $\psi(x) = e^{ik_F x} + re^{-ik_F x}$ with reflection coefficient r. The spatial charge distribution is then

$$|\psi(x)|^2 = 1 + |r|^2 + 2\,\mathrm{Re}(re^{i2k_F x}), \tag{2.4}$$

corresponding to a $2k_F$ modulation in the charge density. This is a 1D version of the result first presented by Friedel. In this simplified free particle picture, the experimental charge modulation directly translates to the Fermi wave vector.

For a more complicated 2D system this simple argument no longer holds, and the LDOS modulations seen in STM will have contributions from several wavelengths. The corresponding wave vectors are captured in the Fourier transform of the STM (FT-STM)

$$P(\boldsymbol{q},\omega) = \sum_i e^{-i\boldsymbol{q}\cdot\boldsymbol{r}_i} \frac{dI}{dV}(\boldsymbol{r}, eV = \omega) \tag{2.5}$$

$$\propto \sum_i e^{-i\boldsymbol{q}\cdot\boldsymbol{r}_i} A(\boldsymbol{r}_i,\omega) \tag{2.6}$$

$$= A(\boldsymbol{q},\omega) \tag{2.7}$$

with $\frac{dI}{dV}(\boldsymbol{r},\omega)$ the STM differential conductance with the tip at position $\boldsymbol{r}$ and with tip-sample bias $eV = \omega$. We find that the FT-STM measures the full spectral function. The quantity plotted in FT-STM is usually reported as the absolute value of $P(\boldsymbol{q},\omega)$. We will in the following chapters keep the convention of referring to the experimental results of the Fourier transform of the differential conductance as the FT-STM, and to our following theoretical calculation of the full spectral function as the FT-LDOS.

We can obtain an expression for $A(\boldsymbol{q},\omega)$ by a Green's function approach. Consider the non-interacting (bare) retarded Green's function

$$G^0(k,\omega) = \frac{1}{(\omega-\mu) - \epsilon_k + i\eta}, \tag{2.8}$$

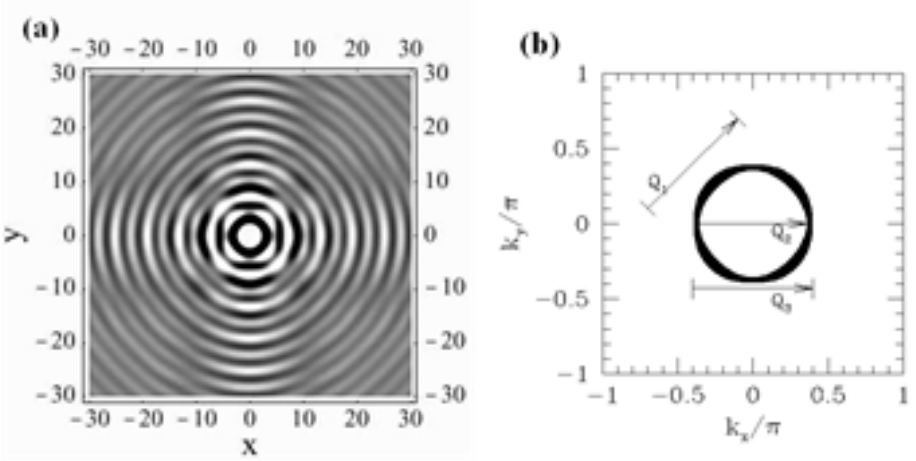

Figure 2.2: A central impurity in the lattice gives rise to modulations in the local density of states. **(a)** A free particle with a circular Fermi surface sparks Friedel oscillations with wave vector $2k_F$. **(b)** The corresponding Fermi surface for an almost-free electron propagating in a crystal. Reproduced from [23].

with ϵ_k the electronic dispersion. We consider the case of a single impurity acting as a local (delta function) repulsive potential corresponding to a constant potential in k-space $V(\boldsymbol{k}) = \sum_i e^{-i\boldsymbol{k}\cdot\boldsymbol{r}_i}\delta(r_i - 0)V_0 = V_0$. The following calculation for the system with multiple impurities is essentially equivalent, see e.g. Bruus and Flensberg [20].
Considering multiple scattering events we can write the full Green's function as

$$G(r_i, r_j, \omega) = G^0(r_i - r_j, \omega) + G^0(r_i - 0, \omega)T(\omega)G^0(0 - r_j, \omega) \tag{2.9}$$
$$\tag{2.10}$$

with the T-matrix the self energy arising from multiple scattering processes on the same impurity, i.e. the solution of the Dyson equation

$$T(\omega) = V_0 + V_0 G^0(0, \omega)T(\omega) \Rightarrow \tag{2.11}$$
$$T(\omega) = \frac{V_0}{1 - V_0 G^0(0, \omega)}. \tag{2.12}$$

We can now obtain the local density of states from the imaginary part of the real space Green's function

$$A(r_i, \omega) = -\frac{1}{\pi}\operatorname{Im} G(r_i, r_i, \omega) \tag{2.13}$$
$$= A^0(0, \omega) - \frac{1}{\pi}\operatorname{Im}\left[G^0(r_i - 0, \omega)T(\omega)G^0(0 - r_i, \omega)\right] \tag{2.14}$$
$$= A^0(0, \omega) + \delta A(r_i, \omega), \tag{2.15}$$

with $A^0(0,\omega) = -\frac{1}{\pi}\,\mathrm{Im}\,G^0(0,\omega)$ the homogeneous system LDOS. The full spectral function (FT-LDOS) is then

$$A(\boldsymbol{q},\omega) = \sum_{r_i} e^{-i\boldsymbol{q}r_i} A(r_i,\omega) \tag{2.16}$$

$$= A^0(\boldsymbol{q},\omega) - \frac{1}{\pi}\,\mathrm{Im}\left[\sum_{\boldsymbol{k}} G^0(\boldsymbol{k}+\boldsymbol{q},\omega)T(\omega)G^0(\boldsymbol{k},\omega)\right] \tag{2.17}$$

$$= A^0(\boldsymbol{q},\omega) + \delta A(\boldsymbol{q},\omega) \tag{2.18}$$

where the last equation defines the impurity induced change in the spectral function. Going to first order in the T-matrix Dyson equation yields the Born approximation $T \to V_{imp}$, i.e.

$$\delta A_{Born}(\boldsymbol{q}) = -\frac{1}{\pi} V_0 \sum_k \mathrm{Im}\left[G^0(\boldsymbol{k}+\boldsymbol{q},\omega)G^0(\boldsymbol{k},\omega)\right], \tag{2.19}$$

with a constant impurity scattering potential and where the q structure *arises entirely from the interference between quasiparticles* described by the bare Green's function convolution. This is the origin of the term quasiparticle interference and why we refer to the FT-STM or FT-LDOS peaks as "QPI features". We note that the Born approximation is valid for small impurity potentials, where the denominator of the T-Matrix is ≈ 1.
For a free electron gas this analytical expression directly yields a divergence in $A(q,\omega)$ at $q = 2k_F\sqrt{1+\omega/\mu}$ [23], closely mirroring the result by Friedel. This divergence is cut off in a real system when adding a finite mean free path l, yielding a Lorentzian peak at the same point with broadening described by the dimensionless quantity $(lk_F)^{-1}$.

For a more complicated system, such as the above cuprate superconductor, the above Friedel result does not hold. It turns out that we can relate the induced spectral function change to the Fermi surface ($E(k) = 0$) or constant energy contours ($E(k) \neq 0$) by means of the so-called joint density of states (JDOS) approximation. Taking the imaginary part of the Green's functions separately in the Born approximation we find

$$\delta A_{JDOS}(\boldsymbol{q},\omega) \propto \sum_k A^0(\boldsymbol{k}+\boldsymbol{q},\omega)A^0(\boldsymbol{k},\omega), \tag{2.20}$$

i.e. the spectral function is given by the convolution of the non-interacting spectral function itself. This convolution has dominant contributions at wave vectors connecting parallel parts of the Fermi surface with large spectral weight. We can see the appearance of the Friedel result: If the Fermi surface is a circle of radius k_F, the JDOS convolution is peaked at $2k_F$. This situation is shown for a more realistic Fermi surface in 2.2, including in **(a)** the observed STM modulation in the LDOS, and **(b)** the corresponding Fermi surface. The FT-LDOS is peaked at the displayed nesting vectors, which would yield a semi circular shape in $A(\boldsymbol{q},\omega)$ with radius $2k_F$.

The JDOS approximation has been used extensively in the cuprates, as it captures many

of FT-STM features when based on convolution of the Fermi surface, obtained experimentally from e.g. angle resolved photoemission spectroscopy (ARPES) [24]. The standard QPI analysis of the cuprates is shown in Figure 2.3. Here, in **(a)**, green lines indicate the normal state constant energy contours obtained from a tight binding model. In the SC state the constant energy contours marked in red form "banana" shapes centered on the nodal point where that gap amplitude $\Delta_k = 0$. These bananas expand in a linear fashion as the energy is increased from $\omega = 0$. The spectral function is peaked at the pointed ends of the bananas, which are connected by eight distinct vectors. The corresponding FT-STM in **(b)** has peaks corresponding to these vectors, and some of these points are reproduced in the JDOS based on the ARPES Fermi surface in **(c)**. We show here the FT-STM and JDOS result at a single bias, but an important part of the agreement is the fact that the length of the scattering vectors follow along as we change ω and change the length of the FS "bananas". The clearest example of this is the small intra banana vector q_7 which should move out as the banana expands when we increase the bias from $\omega = 0$. We will discuss these effect in more detail when we perform QPI calculation for this model.

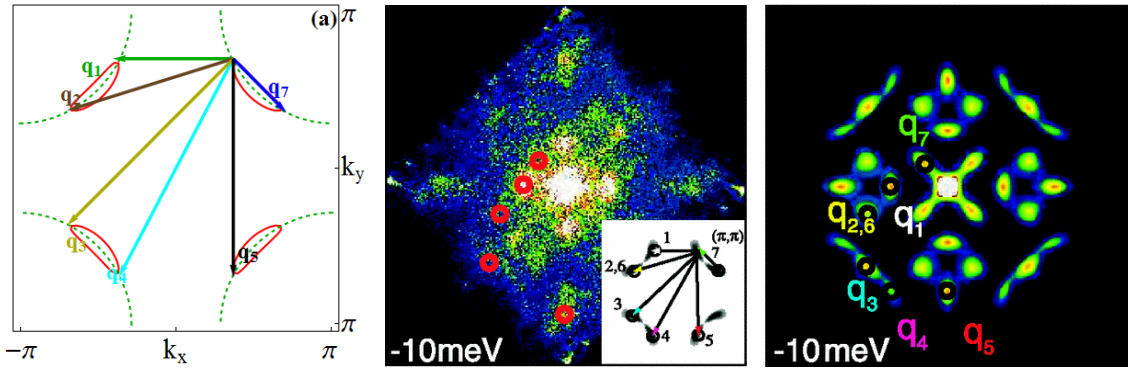

(a) (b) (c)

Figure 2.3: **(a)** A typical cuprate Fermi surface obtained from next nearest neighbour hopping and d-wave superconductivity. The spectral weight is maximal at the eight corner points, which are connected by six unique scattering vectors (mod $\pi/2$). **(b)** Fourier transform of the STM differential conductance measured on the surface of the cuprate superconductor $Bi_2Sr_2CaCu_2O_{8+}$ in the superconducting phase, showing several of these vectors as peak positions. **(c)** JDOS obtained from the spectral function $A^0(\boldsymbol{k}, \omega)$ as measured by ARPES, reproducing several of these features. **(b-c)** Reproduced from [24].

2.3 Unidirectional Features in STM Experiments on FeSe

We now turn to the main focus of this thesis, the highly C_2 features observed in FeSe STM experiments. Probing the gap structure of FeSe on a SiC substrate, C. L. Song et al [25, 26] found evidence of twofold symmetric features in STM topographies. In the experiments, a thin film is constructed by molecular beam epitaxy under excess Se flux, and the STM topography reveals a square lattice of Se atoms ($a_{Se} = 3.8$). This lattice is shown in figure 2.4 **(a)**. Defects in the lattice, visible as the bright spot in figure 2.4 **(b)**, were found to not only exhibit local effects on the immediate nearest neighbor sites, but exhibit surrounding regions of suppressions in the topography extending to 16 Fe-Fe lattice constants (a_{Fe}) only visible along the orthorhombic Fe-Fe axis. The extended and highly anisotropic nature of these suppressions indicate an electronic and not structural origin, which was conjectured to arise from quasiparticle interference.

More detailed studies including multiple orthorhombic domains reproduced the twofold symmetric suppression features and found these to be unique to the most common defect type resembling a dumbbell-like dimer along the Se-Se direction. Several of these are shown in Figure 2.4 **(c)**, wherein the diagonal stripe is a twin boundary separating the region of $|a_{Fe}| > |b_{Fe}|$ from the region with $|a_{Fe}| < |b_{Fe}|$. The Se-Se top layer gives rise to nonequivalent iron positions labeled by μ, ν in figure 2.4 **(d)** with corresponding inequivalent orientation of the dumbbell dimer. Remarkably, the elongated region discussed above is insensitive to this local orientation and always orders along the orthorhombic iron axis. This feature is even more prominent when we consider the domain on the other side of the twin boundary, where the long range feature is rotated to match the flipping of the orthorhombic iron axis. This indicates that the dimer feature is a result of the local impurity structure, while the long ranged feature seems electronic in origin.

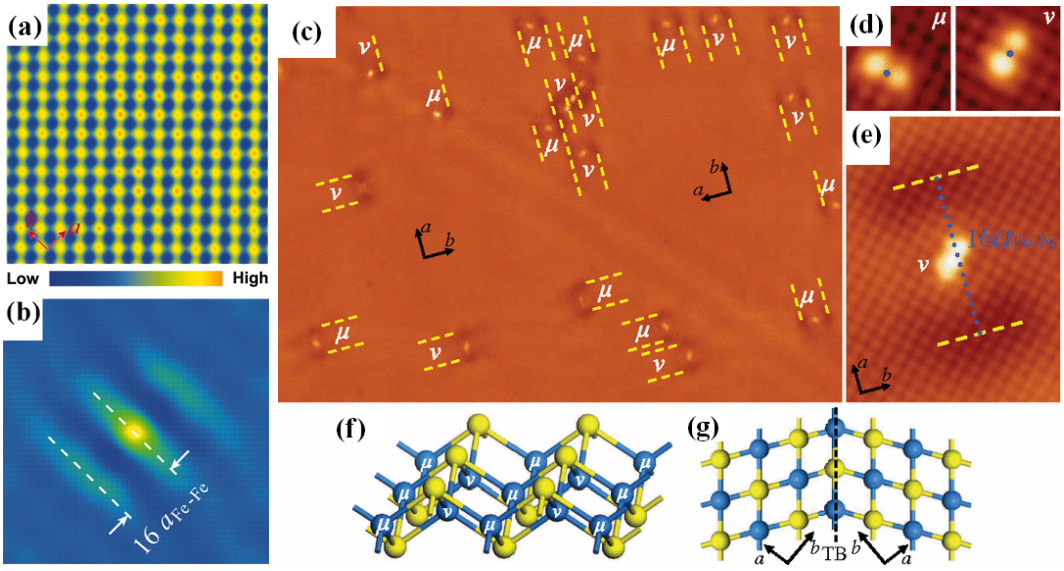

Figure 2.4: **(a)** STM topography showing the Se-Se lattice. **(b)** Twofold symmetric feature centered on a lattice defect extending along the Fe-Fe orthorhombic direction. **(c)** STM topography of FeSe films displaying multiple dumbbell impurity formations oriented along the Se-Se direction ($V = 10mV$, $I = 0.1nA$). **(d)** Zoom dumbbell dimers centered on inequivalent Fe sites ($V = 6mV$, $I = 0.1nA$). **(e)** Zoom of **(c)** displaying the long range (16 Fe lattice constants) and highly C_2 suppression feature. **(f)** Lattice structure indicating the inequivalent Fe positions. **(g)** Structure of a twin boundary separating orthorhombic domains. The long range feature in **(e)** is aligned along the orthorhombic axis and is rotated across the twin boundary. **(a-b)** reproduced from [26] and **(c-g)** from [25].

Several experimental groups have recently performed more detailed STM studies of these unidirectional features, investigating the evolution with the applied bias voltage in the STM. Similarly to the "octet" model in the cuprates, the quantities of interest are the differential conductance and its Fourier transform (FT-STM). Examples of such quantities at an energy $\omega = -24$meV are shown in Figure 2.5 **(a)**, showing the STM mapped surface in a single orthorhombic domain with a multitude of dumbbell dimers at the center of unidirectional suppressions in the differential conductance. The Fourier transform amplitude of the entire real space system is shown on the right, displaying a highly C_2 pattern of small q peaks.

Figure 2.6 **(a-f)** displays a zoom of this differential conductance at different values of the bias voltage V, corresponding to the local density of states at a given energy $\omega = eV$. The long range LDOS modulation is present at high energies $\omega > 50$meV, and is seen to move inwards in a linear fashion along the iron x axis, crossing zero bias at the center only to reemerge and move along the orthogonal iron y axis in **(n-p)**. Note that the SC gap magnitude in FeSe $\Delta \approx 2$meV is much smaller than the considered energies, indicating that this feature is independent of details of the gap structure details. The small gap enables us to obtain QPI patterns without any SC pairing in the Hamiltonian, as long as we refrain from comparing the spectra in the $[-2, 2]$meV energy range.

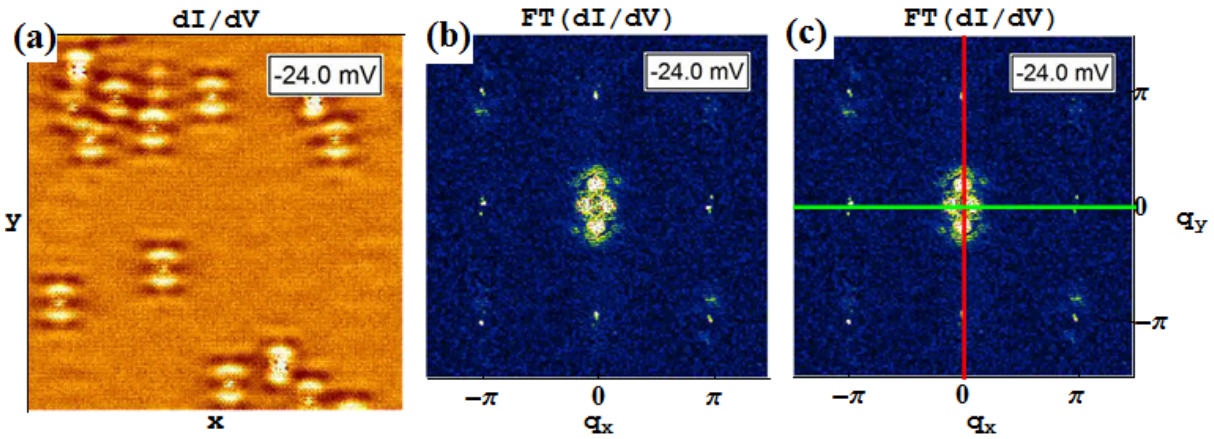

Figure 2.5: **(a)** Differential conductance on a cleaved FeSe layer at −24meV. **(b)** Fourier transform amplitude of the differential conductance (FT-STM) showing the anisotropic small-q modulation. **(c)** Directions used in constructing the line cuts below. Modified from Hanaguri APS 2014 talk [27] (unpublished).

The structure of the LDOS modulation is captured in the Fourier transform amplitude, displayed in 2.6 **(h-m)**. At negative energies the FT-STM features extend outwards along q_y, but as the energy moves towards $\omega = 0$ the q_y peaks disperse inwards, collapsing at the Γ point. For positive energies a new set of peaks move out unidirectionally along q_x instead. These findings were reproduced in a similar experiment performed by Sprau et al. [28].
We aim to connect these anisotropic features to the band structure in the nematic phase and are hence interested in the C_2 features extending along the orthogonal x and y Fe lattice directions. This motivates the inclusion on line cuts along these directions through the central Γ point. The paths used in these cuts are shown in Figure 2.5 **(c)**, extending along $(q_x, 0)$ in red and along $(0, q_y)$ in green. The result of performing this analysis at all measured energies is the plots in 2.6 **(t-u)**, clearly demonstrating the inequality of the FT-STM peak position along q_x and q_y (the cuts along these directions are dissimilar) and showing branches (red arrows) of the FT-STM peaks dispersing with energy.
These branches can be seen in the upper left (and upper right) part of **(t)**, indicating the peaks moving out along q_x for $\omega > 0$ and in the lower part of **(u)** where peaks move out along q_y. We note that the QPI features are very weakly dispersing along q_x for negative energies (lower part of **(t)**) and very weakly dispersing along q_y for high energies (upper part of **(u)**). A satisfactory model for the nematic phase should capture not only the dispersing branches but also the non-dispersing features in these regions. The similar line cuts from Sprau et al. [28] are included in Figure 2.7, showing similar unidirectional features. Note that the this is for a slightly zoomed region compared to the Hanaguri data, with $k \in [-0.2, 0.2]$ and $\omega \in [-0.35, 0.35]$meV.
In terms of the above JDOS picture such an anisotropy in peak positions indicates a strongly C_2 Fermi surface with associated inequivalent position of the dominant scattering vectors. This is the basis of the analysis performed in later chapters, where we will compare these STM-FT line cuts to similar features in $|A(q, \omega)|$ obtained from a band structure model of the nematic phase, which correlate in the above manner with the constant energy contours.

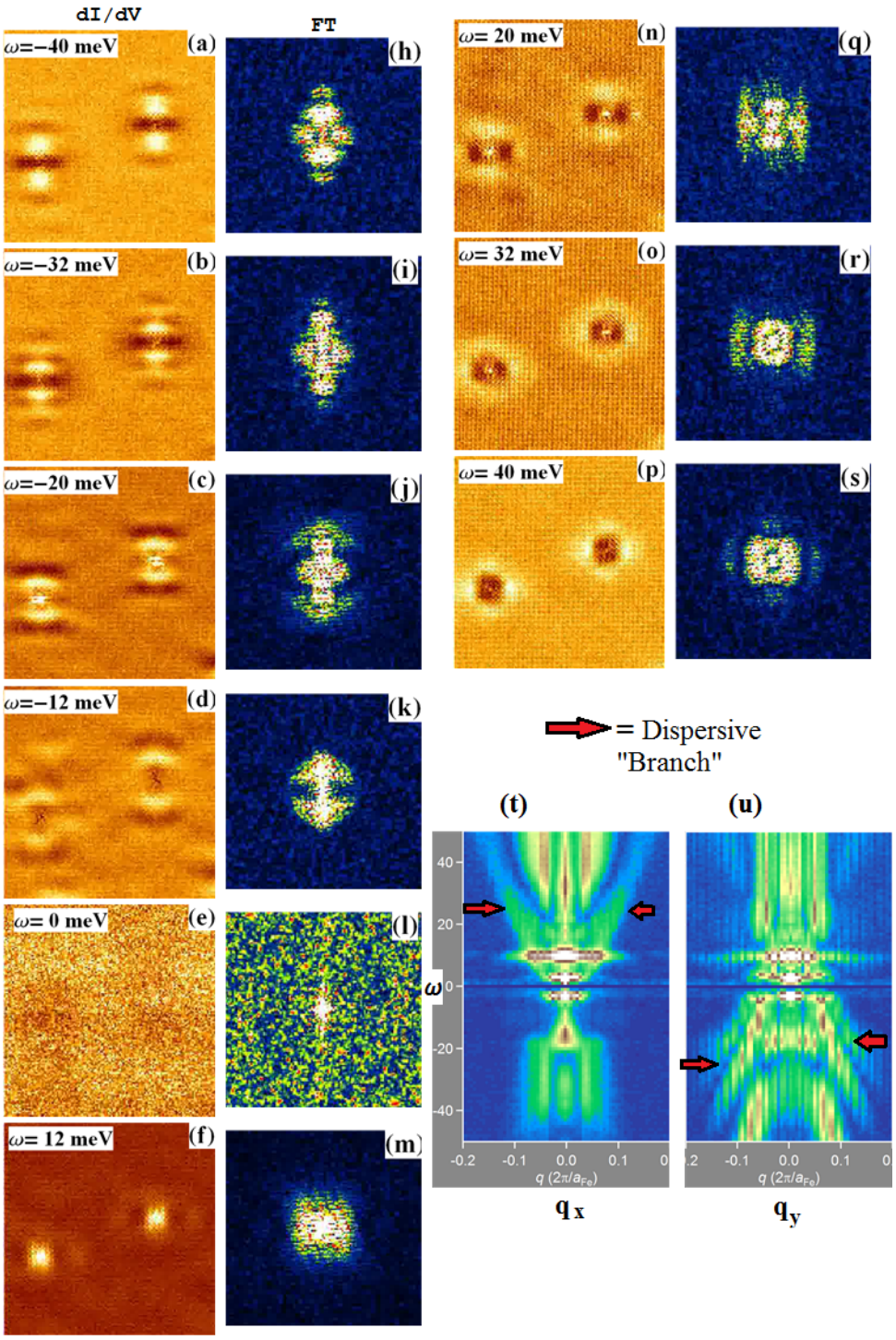

Figure 2.6: **(a-f)** STM differential conductance on the FeSe surface from Hanaguri et al. [27], **(h-m)** the associated Fourier transform amplitude. **(t)** Line cuts from Hanaguri et al. [27] along $(q_x, 0)$ and **(u)** $(0, q_y)$, i.e through the center along each direction. These line cuts capture the unidirectionality of the peak dispersion.

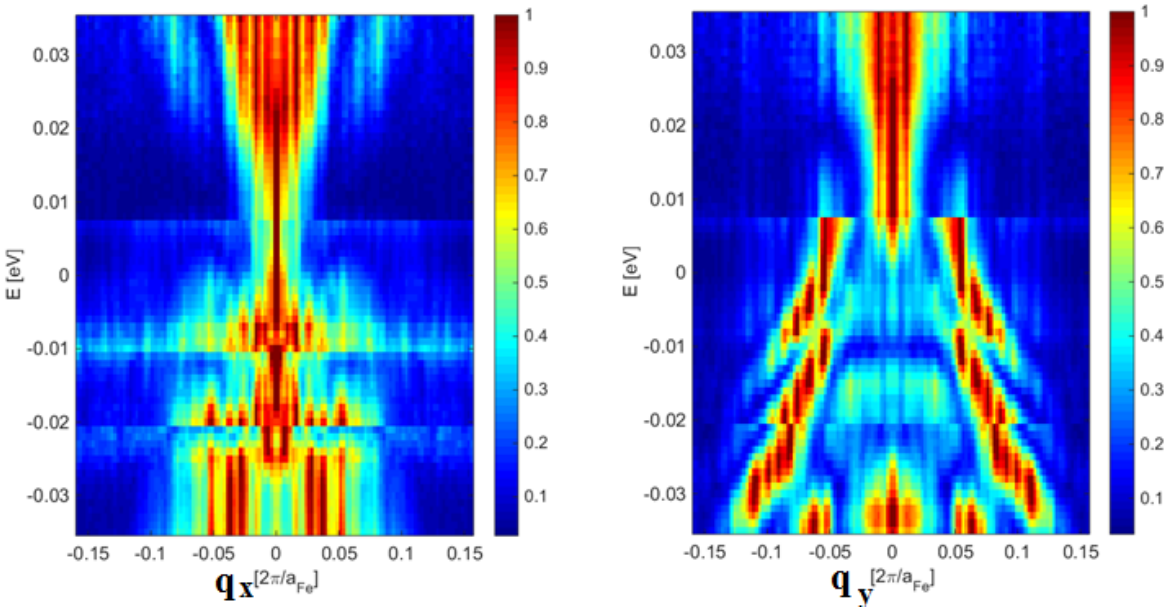

Figure 2.7: Similar line cuts to the above obtained by Sprau et al. [28], displaying the same unidirectional features.

2.3.1 Nature of the lattice defect

The system response to a lattice defect is the quasiparticle interference pattern we have introduced above, with structure determined by the band structure of the clean system. The local properties of the impurity have so far been neglected, yet enters directly into the LDOS modulation in the structure of the T-matrix. In order to extract information about the clean system we need to filter out effects due to the precise type of defect and determine whether the response can be captured by a point-like local potential.
The dominant local impurity feature in FeSe is the dumbbell-like structure along the Se-Se lattice, seen as a double peak in the topograph in Figure 2.4. This feature is present in cleaved planes of bulk FeSe, as well as single and multiple layer planes on different substrates (SiC/SrTiO3). A recent DFT study [29] investigated the formation energy of all relevant types of lattice defects in monolayer and bilayer FeSe. These included Se addatoms, Se_2 dimers, Se-Fe antisites, Se interstitials and Fe vacancies, with the latter three centered on an iron site. Of these, the iron vacancy was found to be energetically favorable and reproduced the dumbbell like pattern by perturbing neighbouring Se orbitals. This last feature is compared with a topograph image in Figure 2.8. The C_2 symmetric dumbbell feature is also found in other FeSCs, e.g. in NaFeAs [30].

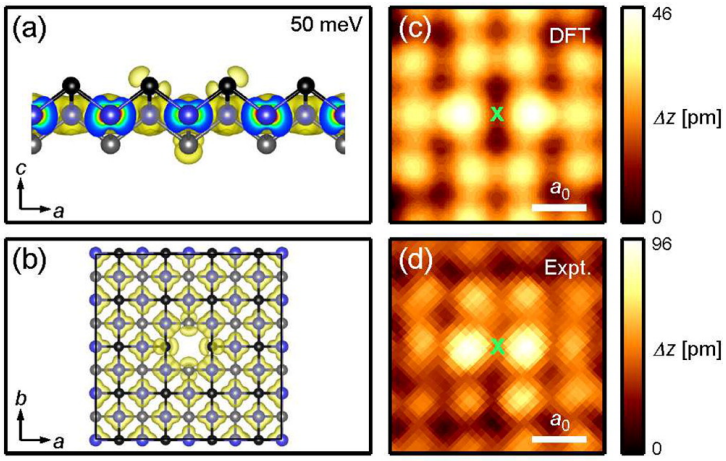

Figure 2.8: The iron site impurity type appears to be an iron vacancy. **(c)** Dumbbell dimer obtained from the iron vacancy DFT calculation. The iron vacancy is marked by the green x. **(d)** Dumbbell in STM topography. Reproduced from [29].

2.4 Summary

In this chapter we have introduced the quasiparticle interference patterns emerging from impurity scattering. A lowest order interpretation of these patterns maps directly to the constant energy contours of the clean system, as seen in the octet model for the cuprates. This interpretation maps the FT-STM peaks to dominant scattering vectors connecting points on the Fermi surface with large spectral weight. A reduction in the Fermi surface symmetry from C_4 to C_2 then directly maps to a reduction in the FT-STM symmetry, a feature observed by multiple groups in FeSe. These unidirectional features along q_x and q_y, which disperse with the applied bias, are best captured in line cuts of the QPI spectra along these directions. In order to generate comparison QPI spectra we will need a way of doing selfconsistent calculations of the LDOS in large real space systems, which we will then Fourier transform to generate $A(q, \omega)$. This is explored in the following chapter, reproducing the octet model of dispersing peaks.

Chapter 3

The Chebyshev-Bogoliubov-de Gennes Method

So far we have seen how the distinct peaks seen in FT-STM experiments on the cuprates can be explained in terms of a one band tight binding model of a d-wave superconductor. This model is computationally simple and comparison with FT-LDOS with the required resolution be obtained from the usual Bogoliubov- de Gennes method. This is in stark contrast to the FeSCs, where, as we shall see, a valid description of the electronic structure necessitates the inclusion of all five d-orbitals. This would limit the system size to a maximum of $\approx 20 \times 20$ in the usual BdG formalism, limiting the resolution to $2\pi/20$. This is insufficient for the small $\boldsymbol{q}$ modulations observed in FeSe.
The inspiration for our efforts into doing QPI in real space in spite of these limitations is the work done by Covaci et al. [31]. These authors successfully used the Chebyshev expansion scheme to perform selfconsistent mean field calculations of the local density of states in large inhomogeneous systems. Using the usual 1-band mean field BCS Hamiltonian, lattice systems as extensive as 500×500 sites were used to model superconductor-metal junctions. The obtained LDOS at the metal surface featured sharp sub gap bound states associated with the Andreev scattering at the interface as could be expected for such a system. The number of coefficients used in the expansion procedure required to fully converge the LDOS was extensive, as evident in Figure 3.1 **(a)**, but the minimal computational resources needed for the CBdG procedure enabled the study nonetheless. This indicates that the resolution needed to distinguish the small $\boldsymbol{q}$ features in the FeSe QPI can be obtained using this method in real space.

In this chapter we will describe how to perform selfconsistent mean field calculations using Chebyshev expansion of the Green's function. This method and the usual Bogoliubov-de Gennes (BdG) diagonalization approach yield nearly identical results yet the Chebyshev procedure will enable the study of large systems, something not possible within the BdG scheme due to memory and time constraints of the diagonalization. We will initially perform the exact expansion for an arbitrary function and then turn to the applicability and implementation of approximation schemes. This method will then be applied to expansions of arbitrary correlation function including the two-body Green's function. In this application the approximation to the infinite series will yield consistent results for the mean fields as it amounts to a simple controlled

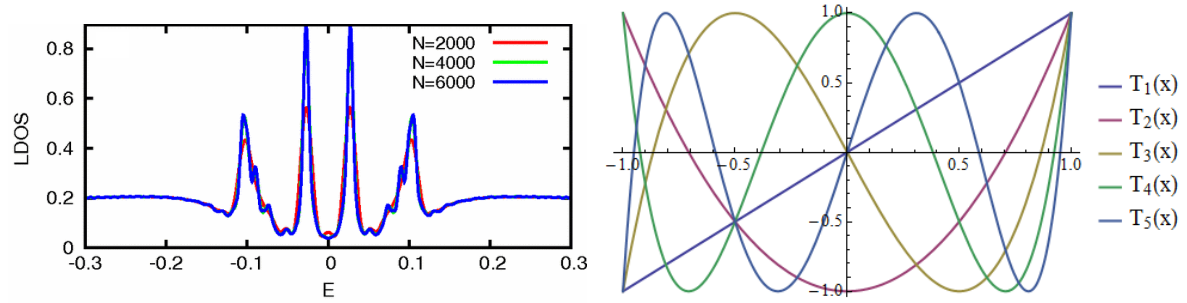

(a) (b)

Figure 3.1: **(a)** The CBdG obtained LDOS on the surface of a metal in a 2D superconductor-metal system for increasing amounts of expansion coefficients. The CBdG method reproduces the expected sub gap peaks associated with Andreev reflection. **(b)** The first few Chebyshev polynomials used in the CBdG expansion scheme. **(a)** Reproduced from [31].

broadening of the spectral function.

3.1 Chebyshev Polynomials

Given a positive weight function $w_\gamma : [a, b] \to \mathbb{R}_+$ we define the inner product with respect to the two functions $f, g : [a, b] \to \mathbb{R}$,

$$\langle f|g\rangle_\gamma = \int_a^b w_\gamma(x) f(x) g(x) dx. \tag{3.1}$$

To each such inner product and associated weight function a family of orthogonal polynomials $(p)_n$ exists, i.e.

$$\langle p_n|p_m\rangle = \delta_{n,m} \cdot \langle p_n|p_n\rangle \,. \tag{3.2}$$

We define the Chebyshev polynomials of the first and second kind as the orthogonal polynomials with respect to the first and second inner product with weight functions $w_1(x) = (\pi\sqrt{1-x^2})^{-1}$ and $w_2(x) = \pi\sqrt{1-x^2}$ defined on the interval $[-1, 1]$, i.e. as the family of polynomials fulfilling the respective orthogonality requirements

$$\langle T_n|T_m\rangle_1 = \int_{-1}^{1} \frac{1}{\pi\sqrt{1-x^2}} T_n(x) T_m(x)\, \mathrm{d}x = \delta_{n,m} \cdot \langle T_n|T_n\rangle_1 \tag{3.3}$$

$$\langle U_n|U_m\rangle_2 = \int_{-1}^{1} \pi\sqrt{1-x^2}\, U_n(x) U_m(x)\, \mathrm{d}x = \delta_{n,m} \cdot \langle U_n|U_n\rangle_2 \,, \tag{3.4}$$

where T_n, U_n indicate the Chebyshev polynomials of the first and second kind, respectively. We are mainly concerned with polynomials of the first kind.

A substitution $x = \cos\theta$ in the first integral eliminates the weight function, yielding the relation

$$\frac{1}{\pi}\int_0^\pi T_n(\cos(\theta))T_m(\cos(\theta))d\theta = \delta_{n,m}\cdot\langle T_n|T_n\rangle_1\,, \tag{3.5}$$

The simplest representation of the Chebyshev polynomials of the first kind is thus seen to be $T_n(x) = \cos(n\arccos(x))$, as this choice immediately yields the orthogonality relation of the trigonometric functions $\cos(nx)$, with $\langle T_n|T_n\rangle_1 = \frac{1}{\pi}\int_0^\pi \cos(nx)^2\,\mathrm{d}x = \frac{1+\delta_{0,n}}{2}$.
We may express these explicitly by use of the substitution $x = \cos(\theta)$ and by adding the identities $\cos(n\theta) \pm i\sin(n\theta) = (\cos(\theta) \pm i\sin(\theta))^n$ in order to obtain

$$\begin{aligned} T_n(\cos(\theta)) &= \cos(n\theta) && (3.6)\\ &= \frac{1}{2}\left[(\cos(\theta)+i\sin(\theta))^n + (\cos(\theta)-i\sin(\theta))^n\right] && (3.7)\\ \Rightarrow T_n(x) &= \cos(n\arccos(x)) && (3.8)\\ &= \frac{1}{2}\left[(x+\sqrt{x^2-1})^n + (x-\sqrt{x^2-1})^n\right]. && (3.9)\end{aligned}$$

Note that this relation is off by a factor of two for the zeroth polynomial, which we define as $T_0(x) = 1$. The expression might appear ill-defined as giving real polynomials, but evaluation for $n \in \mathbb{N}$ exactly cancels the imaginary parts. This representation yields the explicit form of the polynomials

$$T_0(x) = 1, T_1(x) = x, T_2(x) = 2x^2 - 1, ..., \tag{3.10}$$

and the recursion relation

$$T_{n+1}(x) = 2xT_n(x) - T_{n-1}. \tag{3.11}$$

Provided this family of orthogonal polynomials we may naively expand a given function $f : [-1,1] \to \mathbb{R}$ defined on the same interval as the weight function in a series

$$f(x) = \sum_{n=0}^{\infty}\langle f|T_n\rangle_1\,T_n(x). \tag{3.12}$$

For calculation of the expansion coefficients, however, the following expansion turns out to be superior.
Expanding in the modified polynomials $\phi_n(x) = T_n(x)(\sqrt{1-x^2})^{-1}$ which are orthogonal with respect to the second inner product, so as to eliminate the weight function in the integral, we

obtain

$$f(x) = \sum_{n=0}^{\infty} \langle f|\phi_n\rangle_2 \, \phi_n(x) \tag{3.13}$$

$$= \frac{2-\delta_{0,n}}{\sqrt{1-x^2}} \sum_{n=0}^{\infty} \mu_n T_n(x), \tag{3.14}$$

with expansion coefficients

$$\mu_n = \int_{-1}^{1} f(x) T_n(x) dx. \tag{3.15}$$

Some results for Chebyshev polynomials of the second kind will be of interest in the following section, the explicit form

$$U_n(x) = \frac{\sin((n+1)\arccos(x))}{\sin(\arccos(x))}, \tag{3.16}$$

and the integral[32]

$$\mathcal{P}\int_{-1}^{1} \frac{T_n(y)}{(y-x)\sqrt{1-y^2}} \, \mathrm{d}y = \pi U_{n-1}(x), \tag{3.17}$$

where $\mathcal{P}$ is the principal value.

3.2 Finite Order Expansion

3.2.1 Series truncation by kernel convolution

We have thus far shown the infinite order Chebyshev expansion. In practice we need to approximate by a series of order N. Consider the delta function finite order expansion shown in figure 3.2 where a simple truncation of the series is plotted as the dotted line (Dirichlet kernel). The visible oscillations appear whenever the function is not continuously differentiable [33]. In order to suppress these oscillations we turn to approximation theory.
Our general procedure is the convolution of the Chebyshev series with a kernel on the form

$$K_N(x,y) = (2-\delta_{0,n}) \sum_{n=1}^{N-1} g_n \phi_n(x)\phi_n(y), \tag{3.18}$$

defined in terms of the usual orthogonal expansion polynomials and some coefficients g_n, yielding

$$f_{KPM}(x) = \langle K_N(x,y)|f(y)\rangle_2 \tag{3.19}$$

$$= \int_{-1}^{1} \pi\sqrt{1-y^2} K_N(x,y) f(y) \, \mathrm{d}y \,, \tag{3.20}$$

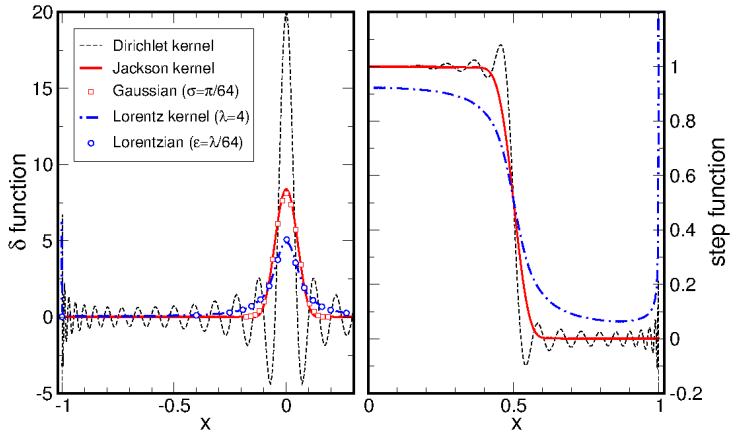

Figure 3.2: Approximations of delta and step functions using different kernels. The simple truncation of the series (Dirichlet kernel) causes oscillations in the expanded function. The oscillations are damped when a different kernel is chosen. Reproduced from [33].

where the notation KPM refers to the Kernel Polynomial Method and denotes our approximation of f. Note that the kernel is uniquely determined from the choice of N and g_n.
The simplest example is the Dirichlet kernel with $g_n = 1$ for all $n \in \mathbb{N}$ which simply yields the truncation of the series

$$f_{KPM}^D = \langle K_N^D(x,y)|f(y)\rangle_2 \tag{3.21}$$

$$= \int_{-1}^{1} \pi\sqrt{1-y^2}(\sum_{0}^{N-1} \phi_n(x)\phi_n(y))f(y)\,\mathrm{d}y \tag{3.22}$$

$$= \frac{1}{\pi\sqrt{1-x^2}}\int_{-1}^{1}(T_0(x)T_0(y) + 2\sum_{1}^{N-1} T_n(x)T_n(y))f(y)\,\mathrm{d}y \tag{3.23}$$

$$= \frac{1}{\pi\sqrt{1-x^2}}(\mu_0 T_0(x) + 2\sum_{n=1}^{N-1} \mu_n T_n(x)), \tag{3.24}$$

recalling the definition of the expansion coefficients. By definition of the Chebyshev expansion, this truncated series converges to the function f in the $|f|_2 = \langle f|f\rangle_2^{\frac{1}{2}}$ norm, i.e., $||f - f_{KPM}||_2 \to 0$ for $N \to \infty$.
We wish to compute the density of states which in the noninteracting case is a sum of delta functions. The convergence found using the simple truncation is then insufficient. Instead we require that the LDOS approximation be positive, normalized and that the convergence is uniform in the sense

$$||f - f_{KPM}||_\infty^\eta = \max_{-1+\eta<x<1-\eta} |f(x) - f_{KPM}(x)| \to 0, \text{ for } N \to \infty. \tag{3.25}$$

These requirements translates to three conditions on the choice of Kernel [33]

1. The kernel is positive, $K_N(x,y) > 0 \; \forall \; (x,y) \in [-1,1]$
2. Normalized, i.e. $\int_{-1}^{1} K_0(x,y)dx = \phi(0) \;\; \Leftrightarrow g_0 = 1$
3. The second coefficient $g_1(N)$ approaches 1 for $N \to \infty$

The first property preserves positivity in the approximation and the second property preserves integrals over approximated functions, i.e. $\int_{-1}^{1} f_{KPM}(x)\,\mathrm{d}x = \int_{-1}^{1} f(x)dx$.
Splitting this integral into terms, this second property follows from the lowest order term

$$\int_{-1}^{1}\int_{-1}^{1} \pi\sqrt{1-y^2}K_0(x,y)f(y)\,\mathrm{d}y\,\mathrm{d}x = \int_{-1}^{1} \pi\sqrt{1-y^2}\phi_0(y)f(y)\,\mathrm{d}y \tag{3.26}$$

$$= \int_{-1}^{1} f(y)\,\mathrm{d}y\,, \tag{3.27}$$

and from the disappearance of all higher order terms

$$\int_{-1}^{1} K_n(x,y)\,\mathrm{d}x = 2\int_{-1}^{1} \phi_n(x)\,\mathrm{d}x \tag{3.28}$$

$$= \int_{-1}^{1} \frac{T_n(x)}{\pi\sqrt{1-x^2}}\,\mathrm{d}x \tag{3.29}$$

$$= \frac{1}{\pi}\int_{-\pi}^{0} \cos(nx)\,\mathrm{d}x = 0. \tag{3.30}$$

Following [33] we can now infer a general class of allowed expansion coefficients which preserve positivity, on the form (proof, see Appendix A.1)

$$g_n = \sum_{\nu=0}^{N-1} a_\nu a_{\nu+n}, a_\nu \in \mathbb{R}. \tag{3.31}$$

3.2.2 The Lorentz kernel

In order to find the imaginary part of the Greens function and thus the full Greens function (see Section 3.4.2) we take the limit

$$\frac{-1}{\pi}\lim_{\eta\to 0}\mathrm{Im}\,\frac{1}{x+i\eta} = \lim_{\eta\to 0}\frac{1}{\pi}\frac{\eta}{x^2+\eta^2} \tag{3.32}$$

$$= \delta(x), \tag{3.33}$$

i.e. we take the limit of a Lorentzian. When approximating Greens function we thus consider a kernel which broadens a delta function into a Lorentzian.
Choosing $a_\nu = e^{-\lambda\nu/N}$ we obtain (proof, see Appendix A.2)

$$g_n^L = \frac{\sinh[\lambda(1-n/N)]}{\sinh(\lambda)}, \tag{3.34}$$

where the relation of the control parameter λ to the width of the Lorentzian is $\eta = \lambda/N$.

3.3 Implementation

3.3.1 Integrals over expanded functions

Naive use of the Chebyshev expanded function when performing integrals over expanded functions is computationally sub optimal and we thus consider the following Fourier reconstruction. Consider a Chebyshev expanded function with Kernel improved coefficients $\mu_n \to \mu_n g_n$

$$f(x_k) = \frac{1}{\pi\sqrt{1-x_k^2}}\left(\mu_0 + 2\sum_{n=1}^{N-1}\mu_n T_n(x)\right), \tag{3.35}$$

In order to calculate the order parameter integrals numerically we can naively perform the energy integration over the Green's function components and associated Fermi functions. For the expanded function defined above (and as we will see, the Green's function components) we can replace these integrals by sums by constructing the function on a set of discrete values or "abscissas"

$$x_k = \cos\left(\frac{\pi(k+1/2)}{\tilde{N}}\right),\ k = 0, \ldots, (\tilde{N}-1). \tag{3.36}$$

The number of abscissas is arbitrary and we choose the value $\tilde{N} = 2N$ from [33].
Evaluation of the expanded function can now be considered as a cosine transform

$$\gamma_k = \pi\sqrt{1-x_k^2}f(x_k) \tag{3.37}$$

$$= \mu_0 + 2\sum \mu_n \cos\left(\frac{\pi n(k+1/2)}{\tilde{N}}\right), \tag{3.38}$$

using the definition of $T_n(x) = \cos(n\arccos(x))$.
Defining

$$\lambda_n = \begin{cases} (2-\delta_{n,0})\mu_n \exp\left(\frac{i\pi n}{2\tilde{N}}\right) & 0 \le n < N \\ 0 & \text{otherwise,} \end{cases} \tag{3.39}$$

we consider the discrete Fourier transform

$$\tilde{\lambda}_k = \sum_{n=0}^{\tilde{N}-1}\lambda_n \exp\left(\frac{2\pi i n k}{\tilde{N}}\right). \tag{3.40}$$

The abscissa values γ_k are then found from

$$\gamma_{2j} = \mathrm{Re}\,\tilde{\lambda}_j \tag{3.41}$$

$$\gamma_{2j+1} = \mathrm{Re}\,\tilde{\lambda}^*_{\tilde{N}-1-j}. \tag{3.42}$$

This scheme is sufficient for the imaginary part of the Green's function, the real part can be obtained by including $\mathrm{Im}\,\tilde{\lambda}_j$.
Integrals can now be converted to sums following Chebyshev-Gauss quadrature

$$\int_{-1}^{1} f(x)g(x)\,\mathrm{d}x = \int_{-1}^{1} \frac{\sqrt{1-x^2}f(x)g(x)}{\sqrt{1-x^2}}\,\mathrm{d}x \tag{3.43}$$

$$\approx \frac{\pi}{\tilde{N}} \sum_{k=0}^{\tilde{N}-1} \sqrt{1-x_k^2} f(x_k)g(x_k) \tag{3.44}$$

$$= \frac{1}{\tilde{N}} \sum_{k=0}^{\tilde{N}-1} \gamma_k g(x_k). \tag{3.45}$$

3.4 Application

3.4.1 (test)-model

We consider a 2D lattice including a multiorbital tight-binding hopping term and a BCS term

$$H = H_0 + H_{BCS} \tag{3.46}$$

$$= -\sum_{i,j\mu,\nu,\sigma} t_{ij}^{\mu\nu} c_{i\mu\sigma}^\dagger c_{j\nu\sigma} - \sum_{i,\nu,\sigma} \mu^\nu c_{i\nu\sigma}^\dagger c_{i\nu\sigma} - \sum_{i,j,p,t} \Delta_{ij}^{pt} c_{ip\uparrow}^\dagger c_{jt\downarrow}^\dagger + \mathrm{h.c.}, \tag{3.47}$$

with $\Delta_{ij}^{pt} = \sum_{qs} \Gamma_{ijpqst} \langle c_{js\downarrow} c_{iq\uparrow} \rangle$. We write the Hamiltonian in Nambu space

$$H = (c_{i\uparrow}^\dagger ... c_{i\downarrow} ...) \mathcal{H} \begin{pmatrix} c_{j\uparrow} \\ \vdots \\ c_{j\downarrow}^\dagger \\ \vdots \end{pmatrix}, \tag{3.48}$$

where $\mathcal{H}$ is a $2n_{band}N_x^2 \times 2n_{band}N_x^2$ matrix with eigenvectors consisting of the (spin up) particle and (spin down) hole amplitudes on each lattice site, and N_x^2 is the number of sites (on a square lattice).

To facilitate the expansion using functions defined on the interval $(-1, 1)$ we rescale the

Hamiltonian, obtaining rescaled eigenvalues $\tilde{E} \in (-1, 1)$eV, in the following manner

$$\tilde{\mathcal{H}} = (\mathcal{H} - b)/a, \text{ with} \tag{3.49}$$

$$b = (E_{max} + E_{min})/2, \text{ and } a = (E_{max} - E_{min})/\eta, \tag{3.50}$$

where η is a small parameter introduced to avoid the divergence at the edges of the interval. Underestimating E_{min}, E_{max} will cause the expansion coefficients to diverge. No change was found in the mean field or converge properties by approximating the extremal energies by the largest energy scale, in agreement with [34].

We wish to construct the selfconsistent quantities (n_σ, Δ) without an exact diagonalization of this Hamiltonian as this procedure precludes the study of large spatially inhomogeneous systems due to time and memory constraints. Instead we expand the Green's functions in a series of Chebyshev polynomials.

The Green's functions of interest for our test model are the 4 components of the Gorkov Green's function

$$\bar{G}_{ij}(\omega) = \lim_{\eta \to 0} \langle 0| \begin{pmatrix} c_{i\uparrow} \\ c^\dagger_{i\downarrow} \end{pmatrix} \frac{1}{\omega + i\eta - \mathcal{H}} (c^\dagger_{j\uparrow} c_{j\downarrow}) |0\rangle \,. \tag{3.51}$$

We will initially consider the more general case of arbitrary correlation functions, but limit ourselves to the zero temperature case.

3.4.2 Zero temperature correlation functions

We define the zero temperature frequency space correlation function by [33]

$$\langle AB \rangle^\pm_\omega = \lim_{\eta \to 0} \langle 0|A \frac{1}{\omega + i\eta \mp \tilde{\mathcal{H}}} B|0\rangle \tag{3.52}$$

$$= \lim_{\eta \to 0} \frac{1}{D} \sum_{k=0}^{D-1} \frac{\langle 0|A|k\rangle \langle k|B|0\rangle}{\omega + i\eta \mp E_k}, \tag{3.53}$$

where we have introduced the identity in the orthonormal basis of eigenstates $|k\rangle$, $\frac{1}{D}\sum_{k=0}^{D-1} |k\rangle \langle k| = 1$. Consider the imaginary part

$$\mathrm{Im}\langle AB \rangle^\pm_\omega = -\frac{1}{D} \sum_k^{D-1} \langle 0|A|k\rangle \langle k|B|0\rangle \lim_{\eta \to 0} \frac{\eta}{(\omega \mp E_k)^2 + \eta^2} \tag{3.54}$$

$$= -\pi \frac{1}{D} \sum_k^{D-1} \langle 0|A|k\rangle \langle k|B|0\rangle \, \delta(\omega \mp E_k), \tag{3.55}$$

where the delta function is obtained as the limit of a Lorentzian, $\lim_{\eta \to 0} \ \eta(\pi(x^2 + \eta^2))^{-1} = \delta(x)$. We may immediately perform the expansion in Chebyshev

polynomials

$$\mathrm{Im}\langle AB\rangle^{\pm}_{\tilde{\omega}} = -\frac{1}{\sqrt{1-\tilde{\omega}^2}}((2-\delta_{0,n})\sum_{n=0}^{\infty}\mu_n T_n(\tilde{\omega}), \tag{3.56}$$

with expansion coefficients

$$\begin{aligned}
\mu_n &= \frac{1}{\pi}\int_{-1}^{1}\mathrm{Im}\langle AB\rangle^{\pm}_{\tilde{\omega}} T_n(\tilde{\omega})d\tilde{\omega} && (3.57)\\
&= \int_{-1}^{1}\frac{1}{D}\sum_{k}^{D-1}\langle 0|A|k\rangle\langle k|B|0\rangle\,\delta(\tilde{\omega}\mp E_k)T_n(\tilde{\omega})d\tilde{\omega} && (3.58)\\
&= \frac{1}{D}\sum_{k=0}^{D-1}\langle 0|A|k\rangle\langle k|B|0\rangle\,T_n(\pm E_k) && (3.59)\\
&= \langle 0|A\;T_n(\pm\tilde{\mathcal{H}})\frac{1}{D}\sum_{k=0}^{D-1}|k\rangle\langle k|B|0\rangle && (3.60)\\
&= \langle 0|A\;T_n(\pm\tilde{\mathcal{H}})B|0\rangle\,, && (3.61)
\end{aligned}$$

setting $E_0 = 0$ and using $|k\rangle\,T_n(E_k) = T_n(\tilde{\mathcal{H}})\,|k\rangle$ which follows since T_n is a polynomial. Explicit calculation of these coefficients will be covered in the following section on Green's functions.

We will not require the full correlation function, but we include it here for completeness. The real part is found from the imaginary part through the Kramer Kronig relation

$$\begin{aligned}
\mathrm{Re}\,\langle A;B\rangle^{\pm}_{\tilde{\omega}} &= -\frac{1}{\pi}\mathcal{P}\int_{-1}^{1}\frac{\mathrm{Im}\,\langle A;B\rangle^{\pm}_{\tilde{\omega}'}}{\tilde{\omega}-\tilde{\omega}'}d\tilde{\omega}' && (3.62)\\
&= -\frac{1}{\pi}\mathcal{P}\int_{-1}^{1}\frac{\mu_0+2\sum_{n=1}^{\infty}\mu_n T_n(\tilde{\omega}')}{(\tilde{\omega}'-\tilde{\omega})\sqrt{1-\tilde{\omega}'^2}}d\tilde{\omega}' && (3.63)\\
&= -2\sum\mu_n U_{n-1}(\tilde{\omega}), && (3.64)
\end{aligned}$$

with $\mathcal{P}$ indicating the Cauchy principal value, and by use of the previously introduced integral.

The full correlation function is then

$$\langle A;B\rangle^{\pm}_{\tilde{\omega}} = \mathrm{Re}\,\langle A;B\rangle^{\pm}_{\tilde{\omega}} + i\,\mathrm{Im}\,\langle A;B\rangle^{\pm}_{\tilde{\omega}} \tag{3.65}$$

$$= \frac{-i\mu_0}{\sqrt{1-\tilde{\omega}^2}} - 2\sum_{n=1}^{\infty}\mu_n(U_{n-1}(\tilde{\omega}) + i\frac{T_n(\tilde{\omega})}{\sqrt{1-\tilde{\omega}^2}}) \tag{3.66}$$

$$= \frac{-i}{\sqrt{1-\tilde{\omega}^2}}(\mu_0 + 2\sum_{n=1}^{\infty}\mu_n(-i\sqrt{1-\tilde{\omega}^2}U_{n-1}(\tilde{\omega}) + T_n(\tilde{\omega}))) \tag{3.67}$$

$$= \frac{-i}{\sqrt{1-\tilde{\omega}^2}}(\mu_0 + 2\sum_{n=1}^{\infty}\mu_n(-i\sin(x)\frac{\sin(nx)}{\sin(x)} + \cos(nx))) \tag{3.68}$$

$$= \frac{-i}{\sqrt{1-\tilde{\omega}^2}}(\mu_0 + 2\sum_{n=1}^{\infty}\mu_n\exp(-in\arccos(\tilde{\omega}))). \tag{3.69}$$

3.4.3 Zero temperature Green's functions

The normal components of the Gorkov Green's function may be expanded as derived above,

$$\bar{G}^{11}_{ij}(\tilde{\omega}) = \lim_{\eta\to 0}\langle c_{i\uparrow}|\frac{1}{\omega + i\eta - \tilde{\mathcal{H}}}|c^{\dagger}_{j\uparrow}\rangle \tag{3.70}$$

$$= \frac{-2i}{\sqrt{1-\tilde{\omega}^2}}\sum_{n=0}^{N}a^{11}_n(i,j)\exp(-in\arccos(\tilde{\omega})), \tag{3.71}$$

with $|c^{\dagger}_{j\uparrow}\rangle = c^{\dagger}_{j\uparrow}|0\rangle$, and coefficients (following the notation of Covaci et. al., expansion coefficients of the Green's functions are denoted a_n)

$$a^{11}_n(i,j) = \frac{1}{1+\delta_{0,n}}\langle c_{i\uparrow}|T_n(\tilde{\mathcal{H}})|c^{\dagger}_{j\uparrow}\rangle\,, \tag{3.72}$$

$$a^{12}_n(i,j) = \langle c^{\dagger}_{i\uparrow}|T_n(\tilde{\mathcal{H}})|c^{\dagger}_{j\uparrow}\rangle^{*}\,. \tag{3.73}$$

The expansion coefficients are obtained recursively using the previously introduced recursion relation of the Chebyshev polynomials.
Setting $|j_n\rangle = T_n(\tilde{\mathcal{H}})\,|c^{\dagger}_{j\uparrow}\rangle$, we find

$$|j_0\rangle = |c^{\dagger}_{j\uparrow}\rangle \tag{3.74}$$

$$|j_1\rangle = \tilde{\mathcal{H}}\,|c^{\dagger}_{j\uparrow}\rangle \tag{3.75}$$

$$|j_{n+1}\rangle = 2\tilde{\mathcal{H}}\,|j_n\rangle - |j_{n-1}\rangle\,, \tag{3.76}$$

and the full expansion coefficients are obtained by $a^{11}_n(i,j) = \langle c_{i\uparrow}|j_n\rangle\,, a^{12}_n(i,j) = \langle c^{\dagger}_{i\uparrow}|j_n\rangle$.
Once we have computed the $|j_n\rangle$ the coefficients for all i are then readily available. The most time consuming step in the process is the sparse matrix vector multiplication $\tilde{\mathcal{H}}\,|j_n\rangle$, which is performed $N \times N_x^2$ times.

3.5 Selfconsistency

We now turn to calculation of the mean fields. The local density of states is

$$A_i^{\uparrow(\downarrow)}(\tilde{\omega}) = -\frac{1}{\pi}\,\mathrm{Im}\,G_i^{11(22)}(\tilde{\omega}), \tag{3.77}$$

and electron density is obtained selfconsistently from the Green's functions

$$n_i = -\frac{1}{\pi}\int_{-1}^{1} d\tilde{\omega}\left(\mathrm{Im}\,G_{ii}^{11}(\tilde{\omega}) + \mathrm{Im}\,G_{ii}^{22}(\tilde{\omega})\right) f(\tilde{\omega}). \tag{3.78}$$

$$\tag{3.79}$$

Restricting ourself to intraorbital pairing, the SC mean field is (see Appendix A.3)

$$\Delta_{ij}^{pt} \propto \langle c_{js\downarrow} c_{is\uparrow}\rangle \tag{3.80}$$

$$= -\frac{1}{2\pi}\int_{-1}^{1} d\omega\ \ \mathrm{Im}\,G_{ij}^{12}(\tilde{\omega})(1-2f(\omega)). \tag{3.81}$$

Defining $\tilde{N} = 2N$, and

$$\tilde{\omega}_k = \cos\frac{\pi(k+1/2)}{\tilde{N}}, \quad k = 0, ..., (\tilde{N}-1) \tag{3.82}$$

$$\gamma_k^{\alpha}(ij,\nu) = -\sqrt{1-\tilde{\omega}_k^2}\,\mathrm{Im}\,G_{ij,\nu}^{1\alpha}(\tilde{\omega}_k), \tag{3.83}$$

with $\alpha = 1, 2$, the integrals are evaluated using Chebyshev Gauss quadrature.
This yields

$$n_i^{\nu} = \frac{2}{\tilde{N}}\sum_k \gamma_k^{\alpha=1}(i,\nu) f(\tilde{\omega}_k), \tag{3.84}$$

$$\langle c_{js\downarrow} c_{is\uparrow}\rangle = -\frac{1}{2\tilde{N}}\sum_k \gamma_k^{\alpha=2}(ij,s)(1-2f(\tilde{\omega}_k)). \tag{3.85}$$

This way of efficiently calculating the mean fields shifts the computational bottleneck on to the calculation of the expansion coefficients themselves, i.e. the previously introduced sparse matrix products. These mean fields have been checked against BdG calculations with the same Hamiltonian, which they match to within $(\Delta^{CBdG} - \Delta^{BdG})/(\Delta^{CBdG} + \Delta^{BdG}) < 10^{-3}$, with Δ any mean field, for a sufficient number of expansion coefficients.
The selfconsistent calculation is performed in the usual manner. First initial guesses for the mean fields including the initial density distribution $(\Delta(r), n(r))$ are made and used as input in the Hamiltonian, together with the initial guess for the chemical potential. A desired average density (doping level) is fixed $n_{avg} = \frac{1}{N}\sum_i n(r_i)$, with N the number of lattice sites. Then the expansion coefficients are calculated for all necessary Green's functions and used to calculate these same quantities $(\Delta^{calc}(r), n^{calc}(r))$. The mean fields and the chemical potential are then

updated

$$\Delta(r) = \alpha\Delta(r) + (1-\alpha)\Delta^{calc}(r) \tag{3.86}$$

$$\mu = \mu + \alpha(n_{avg} - n_{avg}^{calc}), \tag{3.87}$$

with $\alpha \leq 1$ setting the speed of convergence, with $\alpha = 0.6$ in our case. These updated values are then used as input ("guesses") as the process is repeated. The algorithm is terminated when the mean fields are converged and the average density is as required, i.e. when the difference $(\Delta - \Delta^{calc})/(\Delta + \Delta^{calc}) < \delta$, where δ is some small number (we choose $\delta = 10^{-5}$).

3.6 Proof of Concept

With the CBdG formalism established we perform initial tests in the simpler one band models. For the benefit of later QPI studies we are primarily interested in the LDOS, which is the limiting factor in terms of required expansion coefficents [33]. Consider the one band tight binding model of a superconductor

$$H = -t\sum_{\langle ij\rangle} c_{i\sigma}^{\dagger} c_{j\sigma} + H_{SC}, \tag{3.88}$$

with $\langle ij\rangle$ indicating nearest neighbour hopping and H_{SC} corresponding to different gap structures. The system considered are the metal $H_{SC} = 0$, the s-wave superconductor $H_{SC} = \Delta^s \sum_i c_{i\uparrow}^{\dagger} c_{i\downarrow}^{\dagger} + h.c.$, and the d-wave superconductor $H_{SC} = \sum_{\langle ij\rangle} \Delta^d(ij) c_{i\uparrow}^{\dagger} c_{j\downarrow}^{\dagger} + h.c.$, with Δ_d changing sign between hoppings along x and y. Figure 3.3 shows the LDOS on a central site in a 20×20 square lattice in these systems. The LDOS is as expected with a van Hove singularity for the metallic system at $\omega = \mu = 0$, a full gap for the s-wave superconductor, and a nodal gap (linear decrease in the LDOS) for the d-wave superconductor.

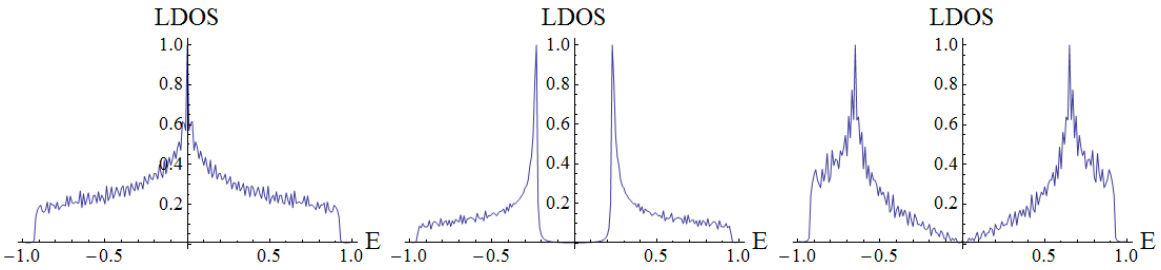

Figure 3.3: Normalized LDOS in the three systems obtained using the CBdG method with the Lorentz kernel. The system is a square lattice of 20×20 sites and the broadening is $\lambda = 20$. **(a)** Normal state (cosine band), **(b)** s-wave superconductor $\Delta_s = t = 1$. **(c)** d-wave superconductor $\Delta_d = t = 1$.

Our QPI implementation of the CBdG method has never been done before, and as such we require a "proof of concept" in a well known system before we move on to the complicated

physics of the FeSCs. This is obtained by reproducing the octet model. The Hamiltonian is an extension of the above including next-nearest neighbour hopping ($t'/t = -0.3$), the d-wave SC term, and an added impurity term

$$H_{imp} = V_0 \sum_{\sigma} c^{\dagger}_{i^*\sigma} c_{i^*\sigma}, \tag{3.89}$$

describing a local repulsive potential ($V_0 = 1$ eV) at the center of the lattice, chosen as 61×61 sites. This local potential disrupts the homogeneous system and the selfconsistent solution includes modulation in the density and the SC gap magnitude, which are displayed in Figure 3.4 **(a)**-**(b)**. The LDOS also includes modulations, as evident in Figure 3.5 **(a)**-**(b)** at two

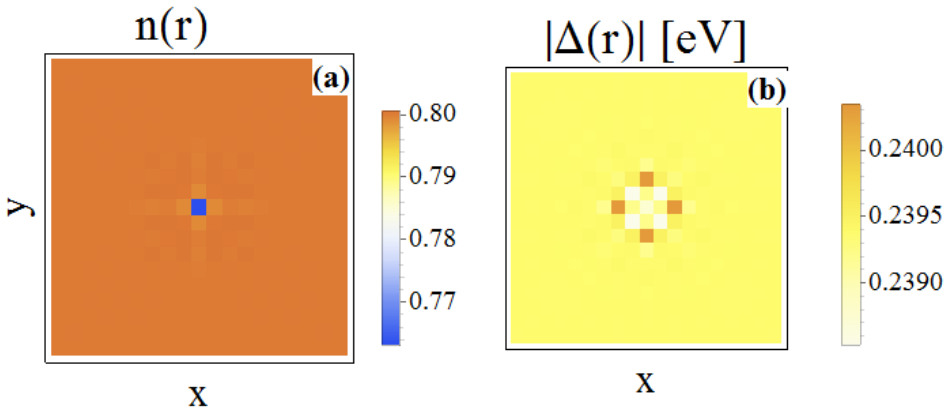

Figure 3.4: A central impurity disrupts **(a)** the density and **(b)** the superconducting mean field in a d-wave superconductor.

distinct energies, with the corresponding FT-LDOS ($P(\boldsymbol{q}, \omega)$) in **(c)**-**(d)** demonstrating distinct peaks and clear C_4 symmetry, as expected. Within the JDOS approximations, these peak positions should be compared with a calculation of the constant energy contours at the same energies which reveal the expected banana shapes of different sizes in Figure 3.5 **(e)**-**(f)**. As we increase ω the banana expands and the octet model scattering vectors grow in length and are slightly rotated. This is reproduced in the FT-LDOS, where e.g. the peak corresponding to the intra banana vector q_7 clearly disperses. This is also seen for q_4, which is rotated and slightly elongated. Peaks similar to the other scattering vectors are also present, and the peak-scattering vector is very well-captured at both displayed energies.

3.7 Summary of the CBdG-QPI Method

The Chebyshev-Bogoliubov-de Gennes method presented yields results similar to the usual diagonalization procedure of BdG, but shifts the resource demanding part of the calculation to the sparse matrix products used in expanding the Green's function. This is computationally simpler, allowing calculations in larger system sizes, but leaves a degree of freedom in the choice of number of expansion coefficients, and the damping parameter used to suppress Gibbs oscillations. We have demonstrated that a small number of ≈ 3000 such coefficients are sufficient to attain a reproduction of complicated LDOS features, and that the arbitrary damping corresponds to a simple controlled broadening of the spectral function. QPI calculations based on this procedure reproduce the octet model.
Based on this reproduction we conclude that the CBdG method is capable of capturing the small modulations in the LDOS needed for QPI purposes. With this check complete we can move on to investigating models for the FeSe band structure in the nematic phase and the resulting QPI. We note that the number of expansion coefficients and choice of broadening will continue to be adjusted based on the complexity of the considered systems, and we will present such considerations when using the method in later chapters.

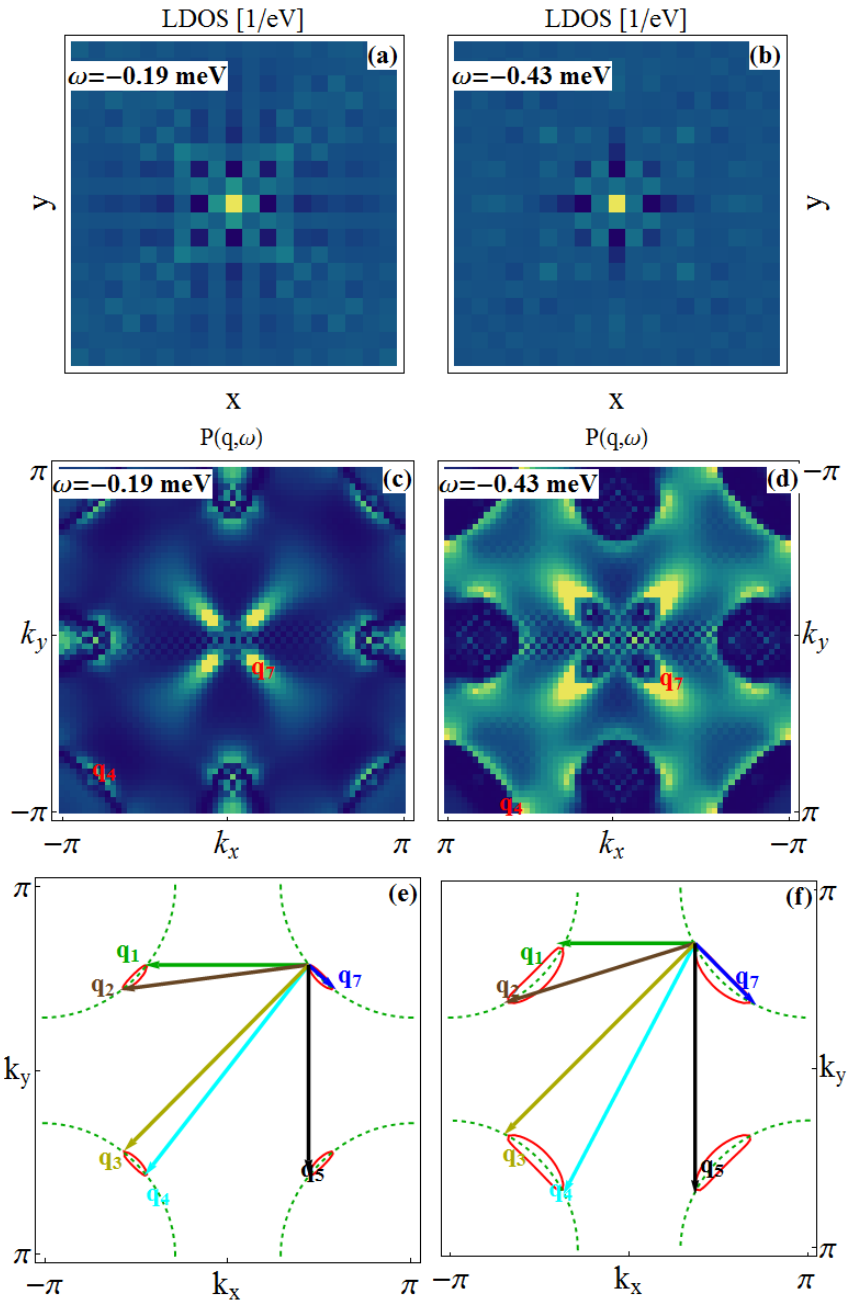

Figure 3.5: Our implementation of the CBdG-QPI method reproduces the octet model. **(a)-(b)** The LDOS obtained from a fully converged selfconsistent CBdG calculation. The color scale moves from blue (small) to yellow (large). **(c-d)** Corresponding FT-LDOS absolute value ($P(q,\omega)$), displaying distinct dispersing peaks and C_4 symmetry. **(e-f)** Constant energy contours ($E(k) = \omega_0$) of the utilized Hamiltonian. Quasiparticle excitations appear in the form of banana centered on the nodal direction, with 6 distinct dominant scattering vectors which disperse as the banana grows. The peak positions map directly to $P(q,\omega)$ above.

Chapter 4

Electronic Structure of FeSe

In this chapter we will consider how to model the band structure of FeSe. Several candidates for the minimal band structure in the tetragonal phase have been proposed with each their own set of approximations and varying in the number of included d-orbitals [35]. The band structure is modified in the nematic phase, where direct probes of the band structure have demonstrated large splittings between previously degenerate points. Tuning the band structure to include these effects necessitates the introduction of orbital order, the splitting of the d_{xz} and d_{yz} orbitals. The symmetry of this ordering component is in dispute, with multiple interpretations of ARPES data available. We will present arguments for the band presented by Kreisel et al. [19], which is used in all following QPI calculations.

4.1 Tight Binding Model

FeSe forms a quasi-2d structure of correlated layers of irons in a square lattice with selenium interspersed, alternating above and below the iron plane. The low energy states arise from the iron $3d^6$ electrons and hence we consider hoppings between irons on a square lattice. The question remains of how many d orbitals to include in the minimal description. In free space the orbitals are degenerate, but in a crystal the crystal field lifts this degeneracy, typically favoring either the three t_{2g} or two e_g orbitals depending on whether the environment is tetrahedral or octohedral. This effect is diminished in the FeSCs, including FeSe, as the staggered position of the Se atoms force an intermediate regime with reduced splitting [35]. The main Fermi surface contribution is still from the t_{2g} orbitals but the remaining e_g orbitals are not far removed. Additionally these partially gapped orbitals will prove relevant as "reservoirs" for impurity bound states when we turn to disorder effects, leading us to consider all five d-orbitals ($d_{xy}, d_{x^2-y^2}, d_{xz}, d_{yz}, d_{z^2}$). In the 1Fe unit cell this corresponds to a five band model, while the two irons in the 2Fe unit cell doubles this to a ten band model. We refer to these models by the five/ten band model in the following, even though we work in orbital space.
The conventions used for the unit cells are shown in Figure 4.1, with the 1Fe unit cell (T_x, T_y)

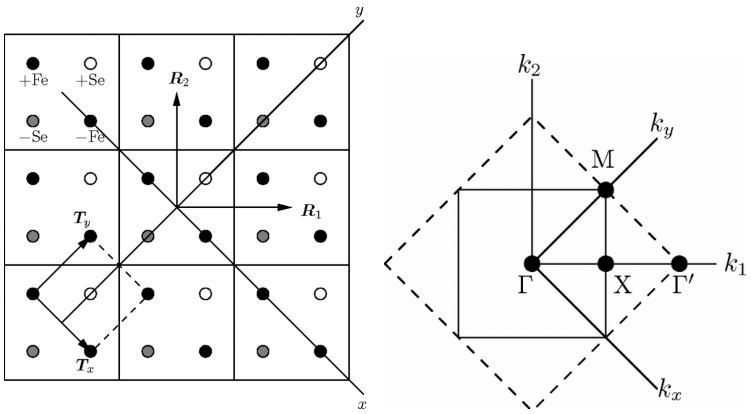

Figure 4.1: **(a)** The utilized convention in the two iron unit cell. (T_x, T_y) label positions in the 1 Fe unit cell, while (R_x, R_y) label positions in the 2 Fe unit cell. This 1Fe-2Fe convention is important when scaling between five and ten band models. **(b)** The 1Fe (unfolded) and 2Fe (folded) B.Z. Reproduced from [36].

and 2Fe unit cell (R_x, R_y) directions and corresponding reciprocal unit vectors related by

$$k_1 = k_x + k_y \tag{4.1}$$
$$k_2 = -k_x + k_y. \tag{4.2}$$

We will initially consider the band structure in the tetragonal phase. The usual starting point for tight binding models is the calculation of hopping integrals by density functional theory, i.e. Hamiltonian

$$H_0 = \sum_{ij,\mu\nu} t_{ij}^{\mu\nu} c_{i\mu\sigma}^{\dagger} c_{\nu\sigma} - \mu_0 \sum_{i\mu} c_{i\mu}^{\dagger} c_{i\mu}, \tag{4.3}$$

where $1 \leq \mu, \nu \leq 10$, describing hopping in and out of the 2Fe unit cell. Such a band was developed for the FeSCs by Eschrig and Koepernik [36], treating FeSe in the tetragonal phase as the building block for more complex FeSCs. This band was then compared with direct and indirect probes of the band structure in FeSe by Mukherjee et al. [37], such as ARPES and quantum oscillation measurements. A large discrepancy was evident in these comparison, with the bandwidth of the calculated and the experimental bands off by a factor of 6. This discrepancy is due to the correlated nature of FeSe, where the correct description includes interactions which we will later model by the Hubbard-Hund model. In the presence of interactions, the Green' function acquires a self energy

$$G^R(k,\omega) = \frac{1}{\omega - \epsilon_k - \sum(k,\omega) + i\eta} \tag{4.4}$$
$$= \frac{1}{\omega - \epsilon_k - \mathrm{Re}\sum(k,\omega) + i(\eta - \mathrm{Im}\sum(k,\omega))}, \tag{4.5}$$

and we see that this self-energy effectively renormalizes the bare ϵ_k of the non-interacting system. This can be included in the tight binding model by renormalizing $\epsilon_k \to \widetilde{\epsilon}_k$, which corresponds to renormalizing the hoppings in the tight binding model $t_{ij} \to \widetilde{t}_{ij}$. Such a new tight binding model was developed in Mukherjee et al. [37] by renormalizing the effective mass (H_{TB}/z, $z = 6$) and shifting specific hopping integrals by hand to better match experiment. It was additionally found that correspondence with the single hole pocket observed at the Γ points necessitated the inclusion of spin orbit coupling, i.e. a term in the Hamiltonian on the form

$$H_{SO} = \lambda \sum_i L \cdot S, \tag{4.6}$$

with $\lambda = 20$meV. The corresponding modifications to the orbital basis tight binding model is determined in Appendix B.1.
This band was then further modified by Kreisel et al. [19] to match the previously mentioned measurements of magnetic $(\pi, 0)$ stripe fluctuations in neutron scattering experiments [18]. These shifts moved the leading magnetic instability from (π, π) to $(\pi, 0)$. This specific feature will be of great importance for our later studies of QPI patterns in the interacting system.

The ten band model can be down-folded to an effective five band model, describing hopping from each iron. This is accomplished by transforming the basis as described above, translating some of the ten band intra unit cell hoppings (onsite) to nearest neighbour hoppings in the ten band model. Special care should be taken to account for the different environment of the irons on each sublattice. The upper left $+Fe$ has selenium atoms above the plane to the north and south, while the $-Fe$ position has selenium atoms above the plane to the east and west. In effect, the irons on the $+Fe$ and $-Fe$ sublattices have electronic environments related by flipping the z axis $z \to -z$. The z coordinate dependence of each orbital is captured in the orbital names, i.e. the affected orbital are the d_{xz} and d_{yz} orbitals, which are odd under this inversion. This changes the sign of any hopping from an even to an odd orbital which changes sublattice.

Figure 4.2 **(a)** shows band structure cuts of the thus obtained five band model between high symmetry points of the 1Fe B.Z., with special attention to points with dominant d_{xz} (red) and d_{yz} (blue) character. These plots are obtained by diagonalizing the Hamiltonian in orbital space (moving to band space), i.e. given a set of hoppings $t_{ij}^{\mu,\nu}$ we first write the Hamiltonian in orbital space

$$H_0 = \sum_{k,\mu,\nu} \epsilon_k^{\mu\nu} c_{k\mu}^\dagger c_{k\nu} \tag{4.7}$$

with $\epsilon_k^{\mu\nu} = \sum_{\delta r_j} t_{ij}^{\mu\nu} e^{ik\delta r_j}$. This 5×5 matrix is then diagonalized for each k point in the cut, yielding the eigenvalues (plotted) and the eigenvalues consisting of the orbital weight of each value. The color is then determined by the largest of these components.

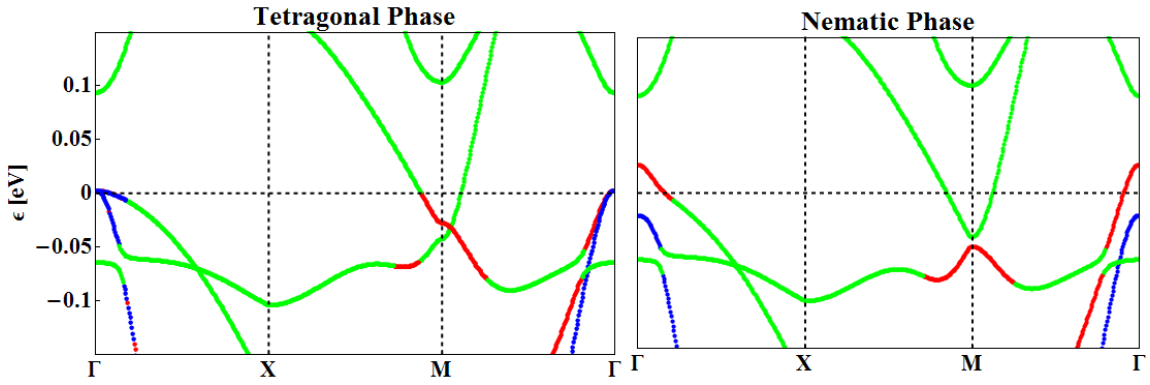

Figure 4.2: Band structure cuts along high symmetry points in the 1Fe B.Z., with regions of dominant contributions from the xz (red) and yz (blue) orbitals marked. **(b)** In the nematic phase these regions are split due to the inclusion of orbital order terms in the tight binding model, matching band structure cuts from ARPES.

4.2 Orbital Order in the Nematic Phase

We can calculate the Fermi surface content by obtaining first the matrix elements of ϵ_k from the tight binding model, and then calculating the 5×5 bare spectral function

$$\mathbf{A}^0(k,\omega) = -\frac{1}{\pi}\,\mathrm{Im}\left[\frac{1}{\omega - \epsilon_k + i\eta}\right]. \tag{4.8}$$

Spectral weight on the Fermi surface is then obtained as $A^0(k,0) = \mathrm{Tr}\,\mathbf{A}^0(k,0)$. The emerging Fermi surface in the tetragonal phase displayed in figure 4.3 **(a)** is typical of the FeSCs, with a shallow central hole pocket and four outer elliptical electron pockets. As required, the FS displays perfect C_4 symmetry.
In the low temperature nematic region, the situation is quite different. Here, ARPES experiments indicate that the d_{xz} and d_{yz} orbital degeneracy is lifted, with a maximal splitting of the bands at both the Γ and X/Y points of ≈ 50meV [19]. Such a change in the band structure can be obtained by introducing orbital order, i.e. terms in the Hamiltonian on the form

$$H_{OO} = \Delta^s \sum_k (n_{k,xz} - n_{k,yz}) \tag{4.9}$$

$$+ \Delta^d \sum_k \left(\cos(k_x) - \cos(k_y)\right)(n_{k,xz} + n_{k,yz}) \tag{4.10}$$

with $\Delta^s = 50$meV and $\Delta^d = 50$meV. The first of these terms is k-independent and simply shifts down the d_{yz} orbital, accounting for the splitting seen at the Γ point in the nematic phase band cut in Figure 4.2. The second (bond-centered or d-wave) term is included in order to account for the reversed sign splitting at the X and Y points observed in ARPES [38]. The FS is now C_2 symmetric as evident in Figure 4.3 **(b)**, since the pockets orbital character deforms differently by

introducing the s-wave orbital order component, and the d-wave term is in itself anisotropic in the B.Z. This expands the central hole pocket, enlarges the X pocket and deforms the Y pocket into the number 8-like shape. This will have profound implications on our later QPI studies, as the dominant scattering vectors are fundamentally changed, reflecting this broken symmetry. We include also the tetragonal and nematic phase orbitally resolved spectral weight at the FS ($A^0_{\mu\mu}(k,0)$), displayed in Figure 4.4. Most of the spectral weight resides in the t_{2g} orbitals, and we note that the contribution to the X and Y pockets in **(d-e)** is sharply divided between the xz and yz orbitals, while the xy orbitals contributes equally. Other ARPES groups have

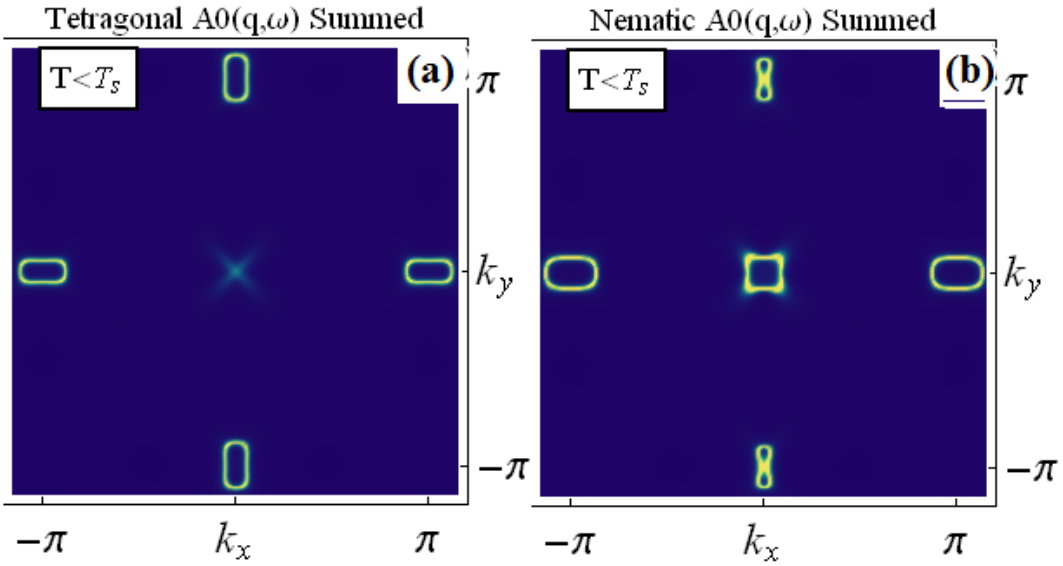

Figure 4.3: Fermi surface in the **(a)** tetragonal ($T > T_s$) and **(b)** nematic ($T < T_s$) phase. The high T FS is C_4 symmetric as expected. Orbital order sets in as we cross the nematic transition, effectively shrinking the electron pocket at the X point and expanding the pocket at the Y point.

presented fits to their data with different orbital order components, e.g. the unidirectional order used in [39] or simply absense of the d-wave component. Our investigations of these proposed band structures indicate that the leading magnetic instability is (π, π) in disagreement with the aforementioned neutron scattering experiments of Wang et al. [18], and sub-optimal for our later investigations into the effect of locally nucleated C_2 magnetic order on QPI. For these reasons we will consistently use the band structure with orbital order as presented above in all further studies.

4.3 Summary of FeSe Band Structure Models

In this chapter we have sought a band structure capable of describing the nematic phase of FeSe. This band structure is not captured by DFT calculations due to the presence of intermediate electronic correlations, but we have presented how the real part of the interaction induced self

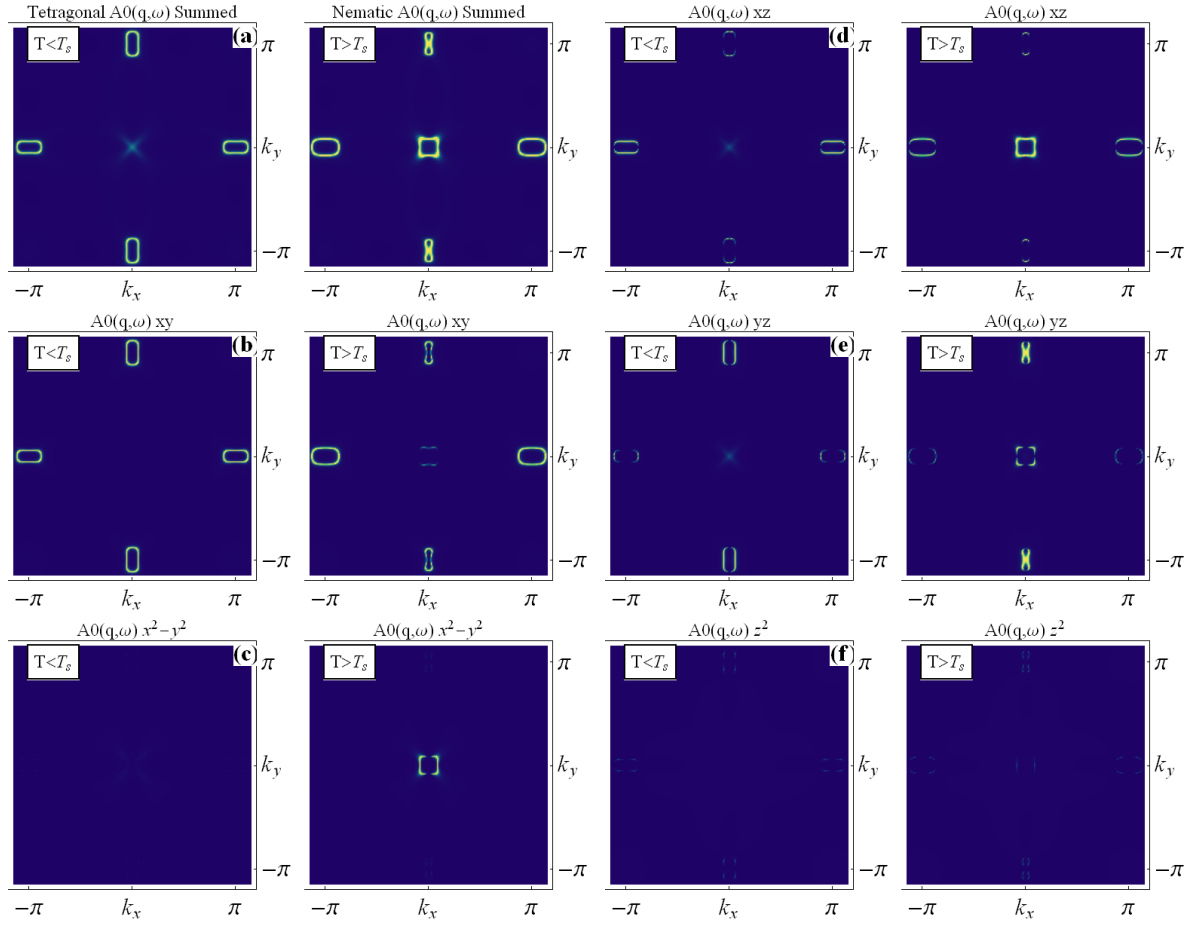

Figure 4.4: Orbitally resolved spectral weight on the Fermi surface $A^0_{\mu\mu}(k, 0)$ in the tetragonal (left) and nematic (right) phase. The contribution at the X and Y points are dominated individually by the xz and yz orbitals, respectively.

energy can be included by renormalizing the hoppings in the tight binding model, yielding bands corresponding with ARPES and quantum oscillation experiments. The nematic phase found under the structural transition in FeSe necessitates the further inclusion of orbital order in the band structure model, which splits the degenerate d_{xz} and d_{yz} and the associated fillings. The structure of this orbital order component is construction to fit ARPES measurements of the orbital splitting at the B.Z. symmetry points, yielding s and d-wave components. Including these terms breaks the tetragonal Fermi surface C_4 symmetry, with fundamental implications for the dominant scattering vectors in QPI. We will investigate this effect in the following chapter.

Chapter 5

Quasiparticle Interference in the Orbitally Ordered FeSe Band

With the CBdG-QPI method established and a band structure model for the nematic phase of FeSe introduced, we are finally ready to attempt the reproduction of the unidirectional features observed in FT-STM experiments. Such C_2 features should follow naturally from dominant scattering vectors connecting points on the nematic phase constant energy contours, which are themselves C_2.
In this chapter we will present the CBdG FT-LDOS results for the five band model introduced in the preceding chapter. We will initially consider the LDOS at and far from the impurity site, and demonstrate the appearance of a resonant state at the impurity site, which can be controlled by the impurity potential. We will then move on to the long range LDOS modulations and their correspondence to the dominant scattering vectors on the constant energy contours. Due to the multiorbital nature of our model the correspondence is less clear than for the octet model, with shifts in the relative peak weight not captured within the JDOS interpretation. The results are then compared directly to the experimental FT-STM.

5.1 LDOS in the Bulk and at the Impurity Site

We have previously demonstrated the validity of the CBdG obtained LDOS in the single band case for a certain number of expansion coefficients. The further complication of the new band structure necessitates a reevaluation of the number of needed coefficients N. In Figure 5.1 we present the evolution of the LDOS in a clean (homogeneous) system of 61×61 lattice sites with N, using a constant broadening of $\eta = \lambda/N = 1\text{meV}$, where λ is the Lorentz kernel control parameter used in the implementation. The LDOS is fully converged at about $N = 3000$ coefficients, with no noticeable change at higher values within for the utilized broadening. We choose this value of N for all further calculations.

Introducing a large central scattering potential $V_0 = 1\text{eV}$ to the system induces both long range QPI modulations as well as local variations in the LDOS at the impurity site itself. Far from the impurity (in the bulk) the LDOS modulations are small, and the LDOS resembles

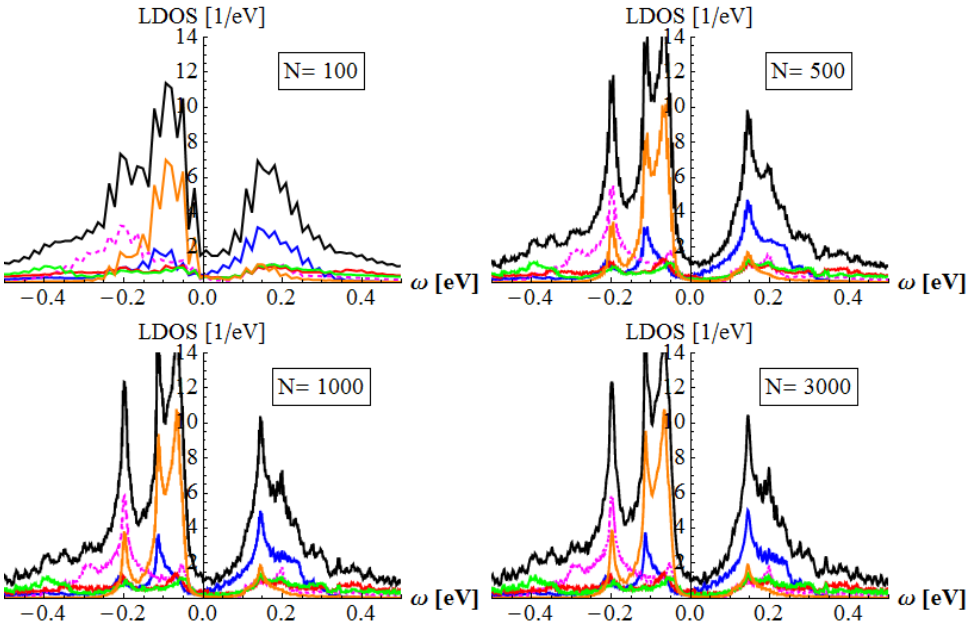

Figure 5.1: LDOS obtained selfconsistently from CBdG in the clean system with 61×61 lattice sites and a constant broadening of 1meV, showing the evolution with the number of expansion coefficients. The black line is the total LDOS ($\sum_\mu A^{\mu\mu}(r_0, \omega)$), while the colored line are the orbitally resolved LDOS components with blue xy, magenta $x^2 - y^2$, red xz, green yz, and orange z^2.

that of the clean system above, as evident in Figure 5.2 **(a)**. The situation is different on the impurity site, with a bound-state like formation at ≈ -25meV dominating the LDOS, shown in Figure 5.2 **(b)**.

The formation of this local feature can be explained in terms of the T-matrix form of the full Green's function, here given for an impurity at the origin $V_0(r) = V_0\delta(r - 0)$,

$$G(r_i, \omega) = G^0(0, \omega) + G^0(r_i - 0, \omega)T(\omega)G^0(0 - r_i, \omega). \tag{5.1}$$

The poles of this function are the usual G^0 poles (the noninteracting system quasiparticle excitations), and poles stemming from the T-matrix, i.e. states induced by the impurity scattering potential. Recalling the definition of the T-matrix, these states are solutions of

$$0 = 1 - V_0 G^0(0, \Omega) \Rightarrow \tag{5.2}$$

$$\frac{1}{V_0} = \mathrm{Re}\, G^0(0, \Omega) - i\pi A^0(0, \Omega), \tag{5.3}$$

equivalent to the conditions $\frac{1}{V_0} = \mathrm{Re}\, G^0(0, \Omega)$ and $A(0, \Omega) = 0$. A gap in the LDOS satisfies the second of these conditions, yielding a bound state when the second condition is simultaneously fulfilled, indicating that the state can be induced or removed by changing this potential.

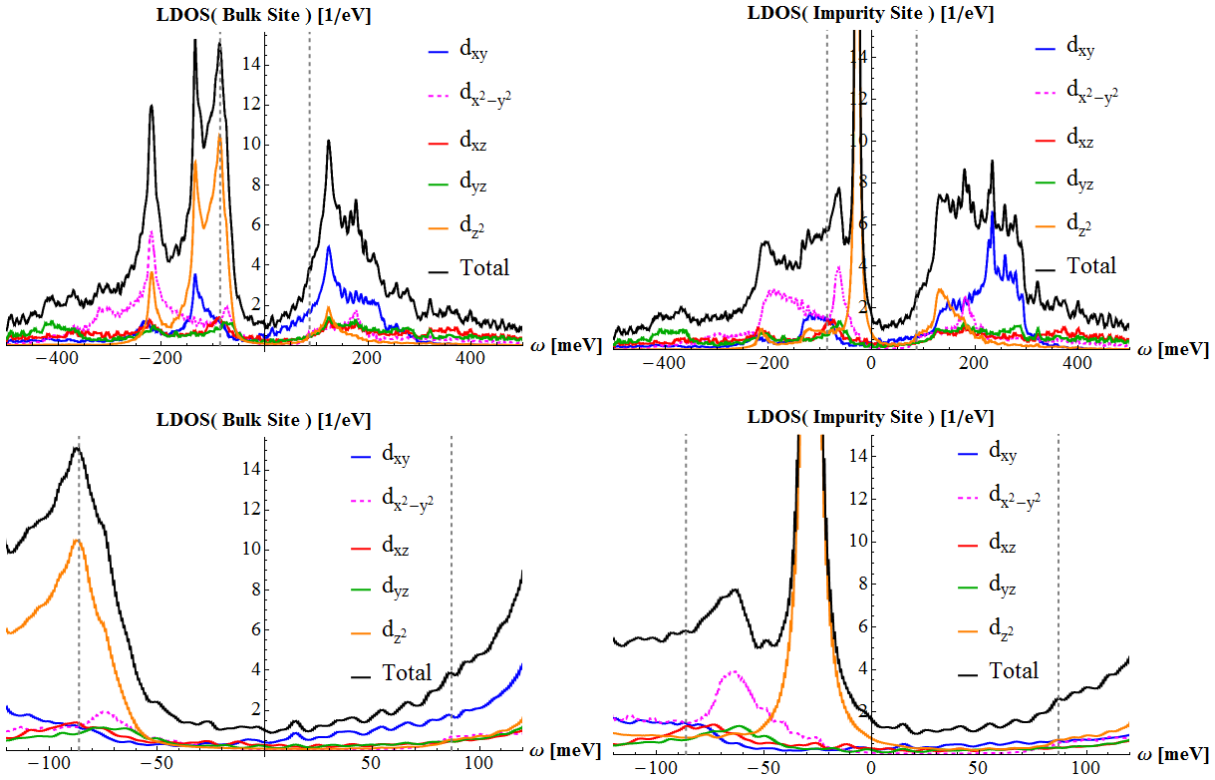

Figure 5.2: LDOS obtained selfconsistently from CBdG in a system of size 61×61 with broadening of 1meV and a large impurity potential $V_0 = 1$eV. Left: Far from the impurity site (Bulk). The vertical gray dotted lines indicate the energy range used in the following QPI study. Right: LDOS at the impurity site. Stronger impurities from resonant states in the nearly gapped d_{z^2} orbital at $\omega = -25meV$.

The LDOS takes a simple form on the impurity site itself

$$A(0,\omega) = A^0(0,\omega) - \frac{1}{\pi}\,\mathrm{Im}\left[(G^0(0,\omega))^2 T(\omega)\right]. \tag{5.4}$$

At the bound state energy the imaginary part of the noninteracting Green's function vanishes, and the only contribution is from the imaginary part of the T-matrix, which has the general form

$$\mathrm{Im}\,T(\omega) = \frac{\pi V_0 A^0(0,\omega)}{(1 - V_0\,\mathrm{Re}\,G^0(0,\omega))^2 + (-\pi V_0 A^0(0,\omega))^2}, \tag{5.5}$$

which is a delta function for the true bound state with $A^0(0,\omega) \to 0$, and a Lorentzian in the absence of the perfect gap, a so-called *resonant state*. As such, there is a contribution to the

LDOS directly at the impurity site of order

$$\delta A(0,\Omega) = (\mathrm{Re}\, G^0(0,\Omega))^2 \frac{\pi V_0 A^0(0,\Omega)}{(1 - V_0\, \mathrm{Re}\, G^0(0,\Omega))^2 + (-\pi V_0 A^0(0,\Omega))^2}. \tag{5.6}$$

Examples of resonant and bound states include the Yu-Shiba-Rusinov (YSR) true bound state in a (fully gapped) s-wave superconductor induced by a magnetic impurity [40], and the resonant state found in a nodal d-wave superconductor induced by a non-magnetic impurity [40]. Our situation is not that simple, since for our band structure the orbitally summed density of states is finite at all relevant energies. However, for the multi-orbital Green's function, equation 5.3 has solutions whenever the density of states in a *single* orbital is gapped [15]. For our band structure model this is true in a wide range for the e_g (z^2 and $x^2 - y^2$) orbitals, allowing the emerging resonant state to form in the z^2 orbital, as was also observed for a slighty different band structure in [15].

The formation of these sharp resonant states from large scattering potentials is an interesting emergent feature in the multi-orbital system, but for our purposes we are interested studying the small scattering potential arising from the iron vacancy. We hence set the scattering potential $V_0 = 10$meV, yielding the new LDOS seen in Figure 5.3, with no major new features at the impurity site, since the resonant state has broadened into the continuum.

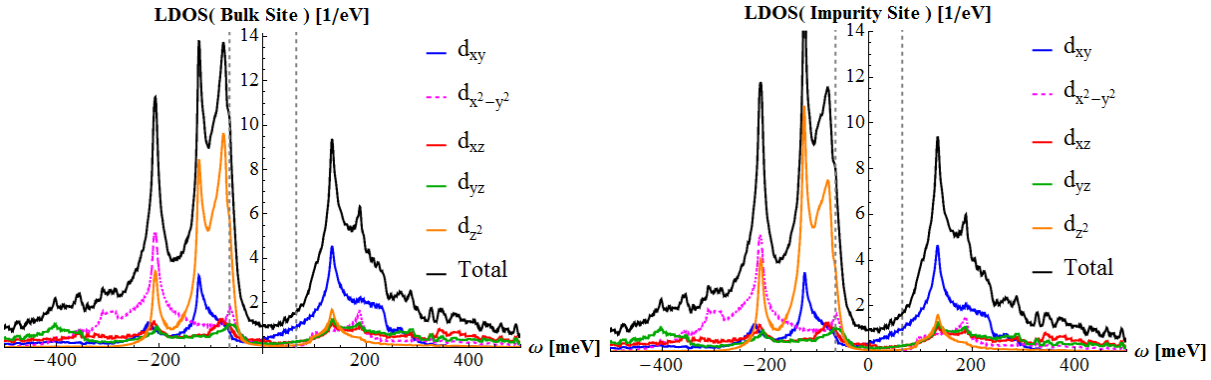

Figure 5.3: LDOS obtained selfconsistently from CBdG in a system of 101×101 lattice sites with spectral broadening 1meV, and a small scattering potential $V_0 = 10$meV. Left: Far from the impurity site (Bulk).The vertical gray dotted indicate the energy range used in the following QPI study. Right: At the impurity site. The resonant state is missing from the impurity site.

5.2 Interpretation of QPI in the Multiorbital System

Before we study the obtained FT-LDOS, we must consider the limits to our interpretation in terms of finding scattering vectors on the Fermi surface. In the five band model all quantities

of interest are 5×5 matrices in orbital space, and the T-matrix result is thus

$$\mathbf{A}(\boldsymbol{q},\omega) = \mathbf{A}^0(\boldsymbol{q},\omega) - \frac{1}{\pi}\,\mathrm{Im}\left[\sum_{\boldsymbol{k}} \mathbf{G}^0(\boldsymbol{k}+\boldsymbol{q},\omega)\mathbf{T}(\omega)\mathbf{G}^0(\boldsymbol{k},\omega)\right], \tag{5.7}$$

and we define the total spectral function as

$$A(\boldsymbol{q},\omega) = \mathrm{Tr}\,\mathbf{A}(\boldsymbol{q},\omega) \tag{5.8}$$

$$= \sum_{\mu} A^{\mu\mu}(\boldsymbol{q},\omega). \tag{5.9}$$

The impurity induced change in the total spectral function is thus the trace of the above matrix product

$$\delta A(\boldsymbol{q},\omega) = -\frac{1}{\pi}\,\mathrm{Tr}\,\mathrm{Im}\left[\sum_{\boldsymbol{k}} \mathbf{G}^0(\boldsymbol{k}+\boldsymbol{q},\omega)\mathbf{T}(\omega)\mathbf{G}^0(\boldsymbol{k},\omega)\right], \tag{5.10}$$

involving all components of the Green's function. This is a fundamentally different quantity than the JDOS, which in the multiorbital case is defined as

$$\delta JDOS(\boldsymbol{q},\omega) = V_0 \sum_{k} \mathrm{Tr}\,\mathbf{A}^0(\boldsymbol{k}+\boldsymbol{q},\omega)\,\mathrm{Tr}\,\mathbf{A}^0(\boldsymbol{k},\omega) \tag{5.11}$$

$$= V_0 \sum_{k} A^0(\boldsymbol{k}+\boldsymbol{q},\omega)A^0(\boldsymbol{k},\omega), \tag{5.12}$$

i.e. the convolution of the total spectral function. In general, the JDOS interpretation in terms of dominant scattering vectors on the Fermi surface is missing not just interference terms of the real part of the Green's function, but also all inherently multiorbital effects in the full matrix product. Hence we should consider the JDOS interpretation as a first step for explaining the obtained $P(\boldsymbol{q},\omega)$, as it is incapable of capturing all features. This is especially important in the nematic phase where we directly tune the orbital content of the constant energy contour pockets.

We note that these quantities (JDOS and T-matrix) can be calculated directly from the tight binding model, in a similar fashion as we used to obtain the spectral weight at the Fermi surface. The discrepancy between the result of these calculations and our real space formalism are minor, as we will reiterate later. The advantage to our selfconsistent real space method is the inclusion of the feedback mechanism from the density modulation around the impurity site, which appears to be a minor effect, and the unique ability to perform calculations in the presence of extended impurity potentials, which we investigate in chapter 7. On the other hand, the advantage of the k-space calculations is higher attainable resolution due to the lack of selfconsistent real space mean field calculations. We stress that all direct k-space calculations of the JDOS referenced in the following chapters have been performed solely by Kreisel [41] or Sprau et al. [28], and not by the author of this thesis.

5.3 FT-LDOS

We perform calculations in a system of 101×101 lattice sites, and iterate until the density is converged to the undoped value of $n_{avg} = 6$. The resulting orbitally resolved density distributions show modulations locally around the impurity with non-degenerate n_{xz} and n_{yz} densities due to the introduction of orbital order. The procedure used to reproduce the octet model in Chapter 3 is repeated, and we show the resulting LDOS and FT-LDOS below in Figure 5.4 alongside the constant energy contours. Not much information is obtained by looking directly at the LDOS, which only demonstrates the existence of Friedel oscillations along the x and y axes. The real structure is shown in the FT-LDOS, where the utilized color scale indicates is yellow for large values and blue for small values in all following figures. The FT-LDOS images are in general not shown on the same color scale, as there is considerable variation in the amplitude.

These images seem quite complicated at a glance, but actually consist of several repeating

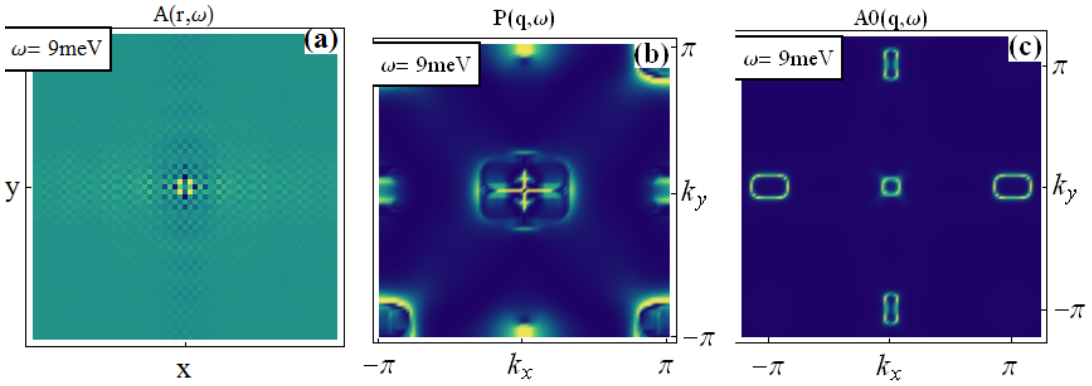

Figure 5.4: Real space selfconsistent calculation of the LDOS and the FT-LDOS. **(a)** LDOS zoomed around the impurity. **(b)** FT-LDOS $P(\boldsymbol{q}, \omega)$. **(c)** Corresponding constant energy contours extended outside the B.Z. $[-\pi, \pi]$ interval to include the full pockets and all scattering vectors.

features. We will start by considering the constant energy contours, shown in Figure 5.5 **(b)**, and identify any nesting vectors. There are inter-pocket scattering vectors connecting the central hole pockets with the X and Y points ($q_{\Gamma \to Y}$), inter-pocket vectors connecting the electron pockets themselves ($q_{X \to Y}$), and intra-pocket vectors inside the electron and hole pockets. We are interested in the k_x/k_y anisotropy, which should be evident mostly in the intra-pocket vectors due to the deformation of the pockets themselves in the nematic phase. Hence we briefly touch on the mostly C_4 large q features in the FT-LDOS, and focus on the small q C_2 features observed in experiment. We remind the reader that the experimental features of interest are characterized by their dispersion as the bias is tuned, extending outwards to approximately the mid point of the B.Z. As such, we will pay special attention to such features below.

Turning to the FT-LDOS in Figure 5.5 **(a)**, the half-circle like features at the X and Y points, as well as at the M points, are quite clearly interpreted as these large q inter-pocket

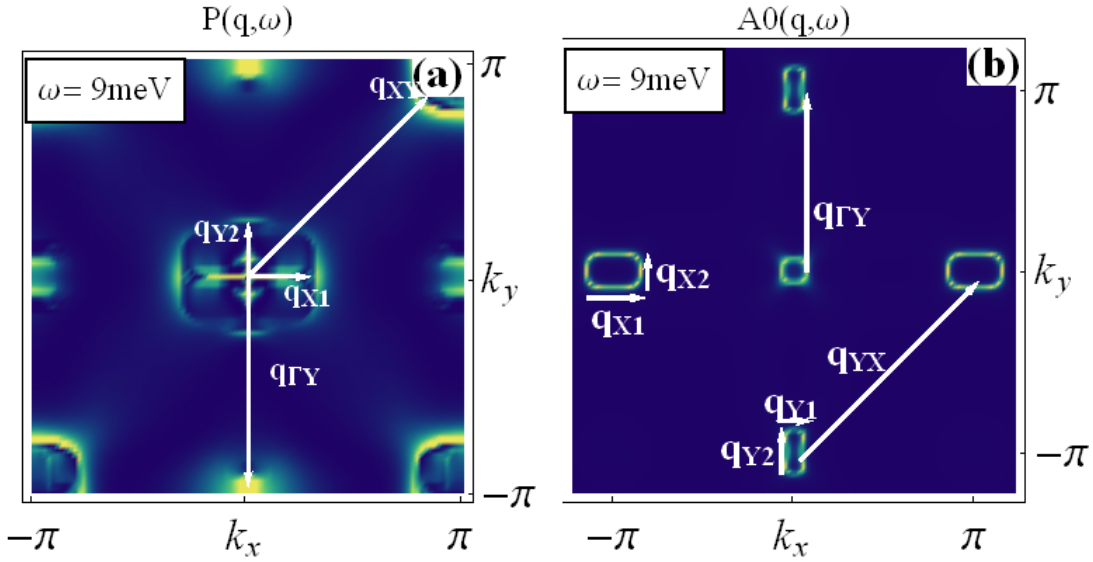

Figure 5.5: The above figure with scattering vectors and corresponding peaks marked. **(a)** FT-LDOS. **(b)** Corresponding constant energy contours extended to include the full pockets and all scattering vectors.

vectors. The small q modulations, on the other hand, correspond to intra-pocket vectors in all five pockets. As the pockets deform in the nematic phase, these small q features become C_2. Corresponding calculations for the tetragonal phase simply yields a C_4 FT-LDOS. The dominant features in the FT-STM, i.e. peaks dispersing inwards along k_x from -50meV to 0meV and then out along k_y from 0meV to 50meV, appears to be reproduced in the full data. We will investigate these two regimes in the following subsections.

5.3.1 QPI from 0 to 50meV

The experimental FT-STM at positive energies include small q strongly C_2 features which disperse outwards along k_x as the energy increases.
In Figure 5.4 we present the small q scattering vectors observed in our calculation of the FT-LDOS. Comparing with the constant energy contours, we observe a small hole pocket and large rectangular pockets at the X and Y point. Orbital order has induced larger pockets at the X points, which are elongated along k_x. Vectors connecting the parallel sides (q_{X1} and q_{X2}) must be the dominant contributions to the QPI pattern. The situation is the same for the Y pocket, but with $q_{Y1} < q_{Y2}$. Scattering vectors from these parallel sides contribute the streak centered on q_{Y2} and q_{X1} points marked on the FT-LDOS.
Longer parallel sides contribute more similar scattering vectors, enhancing the corresponding peak in the FT-LDOS. Long sides also allow slightly tilted vectors connecting slightly regions, resulting in a sharp peak at e.g. $q_{X2} = (\alpha, 0)$ with peaks of decreasing magnitude at $(\alpha \pm \delta_q, 0)$. As such, the longer the parallel side in these rectangular pockets, the sharper the peak at the vector connecting the sides, and the wider the streak centered on this peak. Scattering from a

square pocket is in this sense similar to the Friedel result for a perfect ring on the Fermi surface. The circular pocket with radius k_F creates a circle in the FT-LDOS with radius $2k_F$, and the square pocket with sides a, b create a square feature in the FT-LDOS with sides $2a, 2b$. Both the X and Y pockets contribute such a rectangle in the LDOS of opposite orientation, as can be seen more clearly at higher energies in 5.6 **(b)**, with the combined "propeller" formation. The streak features are the short ends of these rectangles.

Figure 5.6 demonstrates dispersion of these peaks as the energy is increased, alongside the constant energy contours. The X and Y pockets expand, elongating the q_X and q_Y vectors, which causes the streak features in the FT-LDOS to move outwards. The features at $(\pm\pi, 0)$ at $(0, \pm\pi)$ are removed exactly when the central hole pocket disappears, i.e. when the scattering vector $q_{\Gamma\to X}$ disappears.
In this region the observed FT-LDOS appears to coincide with the JDOS interpretation, the observed dispersion of peaks is explainable in terms of the expanding rectangular pockets, and the breaking of C_4 symmetry arises naturally from the different sizes of the X and Y pockets in the nematic state. We finally remark that this nematic response is weak: While the streak positions along k_x and k_y have different amplitude, the dispersing streak along k_y is always present and should be observed in experiment based on our calculation.

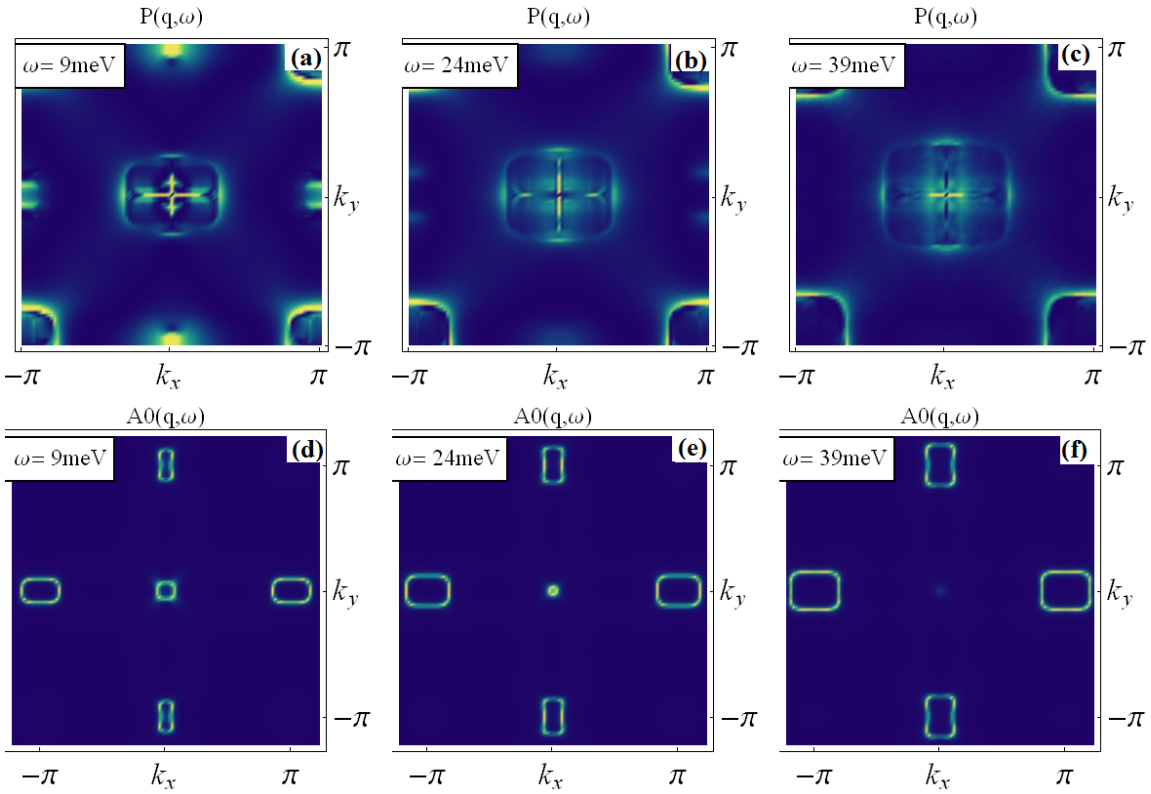

Figure 5.6: Dispersion of the QPI peaks at positive energies. **(b)** FT-LDOS. **(c)** Corresponding constant energy contours extended to include the full pockets and all scattering vectors.

5.3.2 QPI from -50 to 0meV

In this region the dominant FT-STM feature disperses outwards along the orthogonal direction k_y. We consider again a single representative QPI image, shown in Figure 5.7, and identify the dominant scattering vectors. Starting again with nesting vectors on $A^0(q,\omega)$, we should have a small q elliptical contribution from the X pockets in the form of q_{X1} and q_{X2}, similarly to the previous situation. The Y pocket has collapsed to two small pockets, from which we expect a *sharp* contribution at q_{Y2}. The outer Γ pocket has a multitude of intra-pocket scattering vectors, and we have marked the longest of these as $q_{\Gamma 1}$ and $q_{\Gamma 2}$.
Turning to the FT-LDOS, we easily determine the q_{X1} and q_{X2} contribution along k_x. The longer ranged feature along k_y must stem from a combination of q_{Y2} q_Γ vectors due to the extended shape. The Γ pocket retains approximate C_4 symmetry, and we would thus expect to see a similar feature at the same extension along k_x within the JDOS interpretation. As we shall see below this feature is included in the entire region, but it dominated by the corresponding peak along k_y due to the contribution from q_{Y2} along this axis. This contribution should yield a dominant *sharp* peak, yet it appears that the entire extended feature is much larger than the corresponding feature along k_x. This indicates a shift in spectral weight arising from the multiorbital nature of the Green's function, which is not captured fully within the JDOS interpretation.

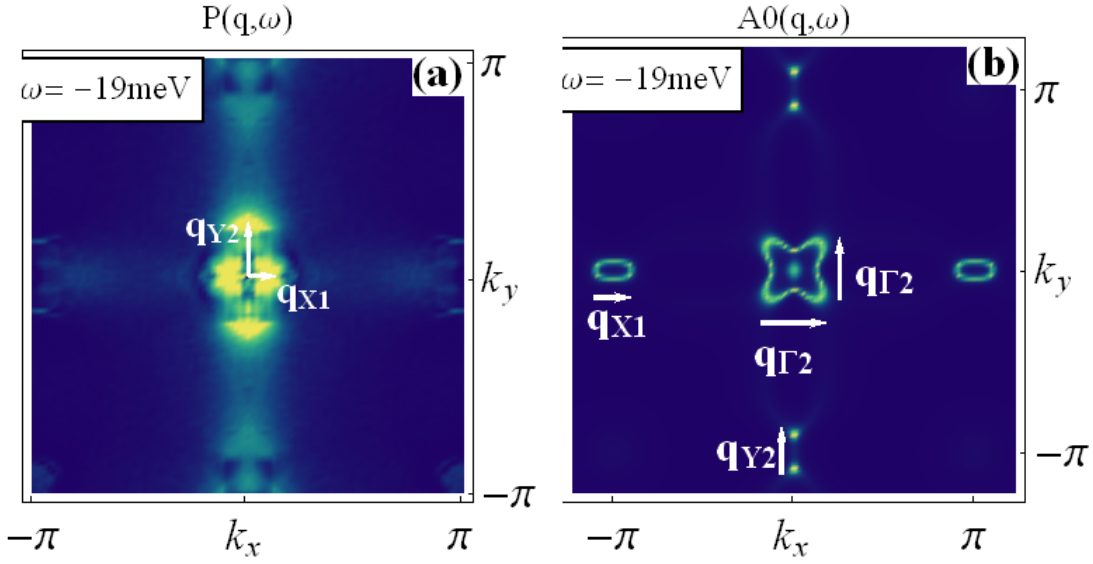

Figure 5.7: A representative FT-LDOS image and corresponding constant energy contours at negative biases. **(a)** FT-LDOS $P(\boldsymbol{q},\omega)$. **(b)** Corresponding constant energy contours extended to include the full pockets and all scattering vectors.

Figure 5.8 tracks the evolution of the FT-LDOS and constant energy contours as the energy is lowered. The collapse of the X pockets removes the feature along k_x, while the emergence of the inner Γ pocket yields a semi-circular central feature. The enhanced feature along k_y dominates the corresponding feature along k_x at all energies, and disperses outwards as expected. The

feature gets broader as the small pockets at Y expand into the time-glass like shape.

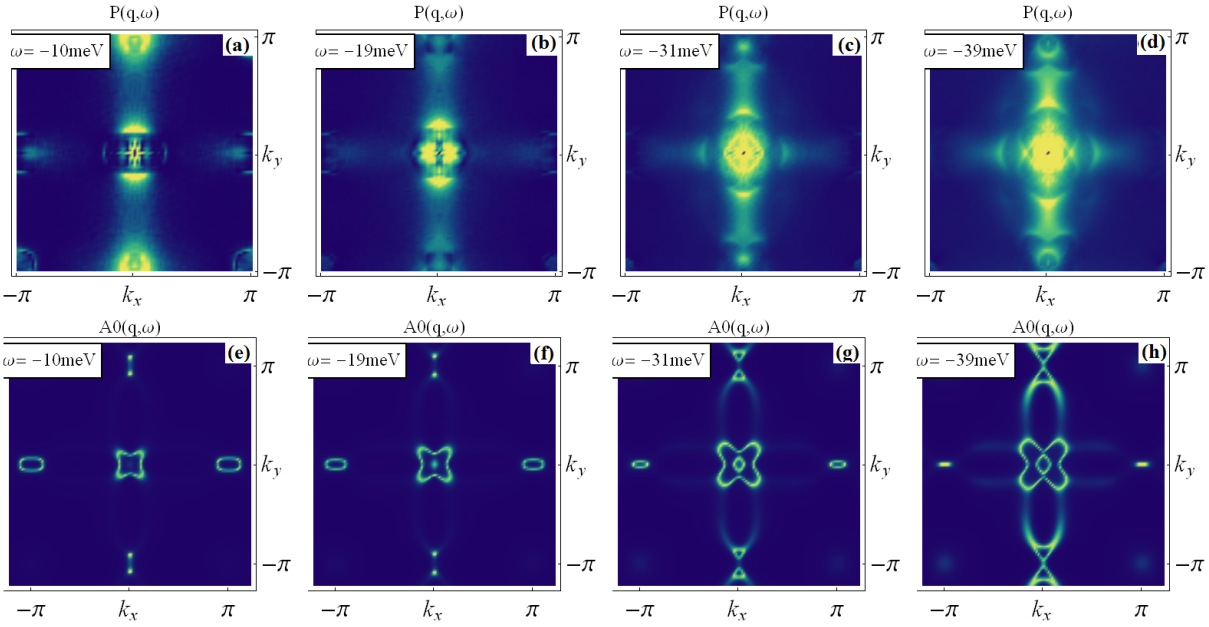

Figure 5.8: Dispersion of the QPI peaks at negative energies. **(b)** FT-LDOS. **(c)** Corresponding constant energy contours extended to include the full pockets and all scattering vectors.

5.4 Dispersion of the Unidirectional Features

We are interested in the unidirectional evolution of the FT-STM pattern with applied bias, i.e. the dispersion of the peaks in $P(\boldsymbol{q}, \omega)$ along k_x and k_y. This is captured in the line cuts introduced in Chapter 2, which should demonstrate the difference in dominant scattering vector length as the Fermi surface is deformed. The result of this procedure for 101 separate bias values in the above system is shown in Figure 5.9, where we also include experimental line cuts for comparison. The line cut thus obtained has large horizontal "rib" like features at small q, consisting of strong scattering peaks which appear and disappear rapidly as the bias changes. We have found this weird behaviour to be a system size effect, as these features are more evident in smaller system sizes for our calculations, and the space between the ribs disappears continously in k-space JDOS calculations when the number of k-points is increased, creating solid formations of instead [41].

The dispersing unidirectional $P(q, \omega)$ peaks show up in these images as diagonal lines moving in from large to small q. For positive energies we saw a peak moving in along k_x, corresponding to the diagonal line in the upper part of 5.9 **(a)**. When compared to the similar diagonal line in **(b)** corresponding to the peak along k_y, we see directly that the peak along k_x is at larger $|q|$ for all energies.
In the lower region of these plots the dominant peak is along k_y, seen moving out as the energy is decreased in **(b)**. A similar line is present along k_x in **(a)**, but much smaller in magnitude. The summary of these features in the FT-LDOS is thus dominant dispersing peaks along k_x for positive energies, and dominant peaks along k_y for negative energies. The experimental FT-STM demonstrate similarly dispersing features, but there is a clear difference in the degree of anisotropy. While our FT-LDOS have stronger peaks along the direction matching the experimental feature, the peak along the other direction is always present with comparable amplitude. The experimental result is much more C_2, with no weaker peak dispersing along the other direction. This is shown in the below experimental line cuts, where the dispersive features are clearly along k_x for positive energies, and along k_y for negative energies.

5.5 Summary and Outlook

In this section we have presented our initial QPI results using the CBdG method. The utilized model of the band structure in the nematic state yield highly C_2 constant energy contours, which map directly to the position of the FT-LDOS peaks, controlling the dispersion pattern. The JDOS convolution interpretation successfully predicts the position of these peaks at all energies, while the peak amplitude varies due to the multiorbital nature of the nematic state quasiparticle interference. The resulting FT-LDOS has similar dispersing features to the experimental FT-STM, but does not fully capture the degree of anisotropy. The close match in the dominant peak dispersion with applied bias between our calculation and the experiment indicates that the discrepancy is due to a shift in the relative weight of different scattering vectors, and not the shape of constant energy contours in the utilized band. In essence, the experimental results appear to have intra-pocket scattering vectors from some pockets enhanced

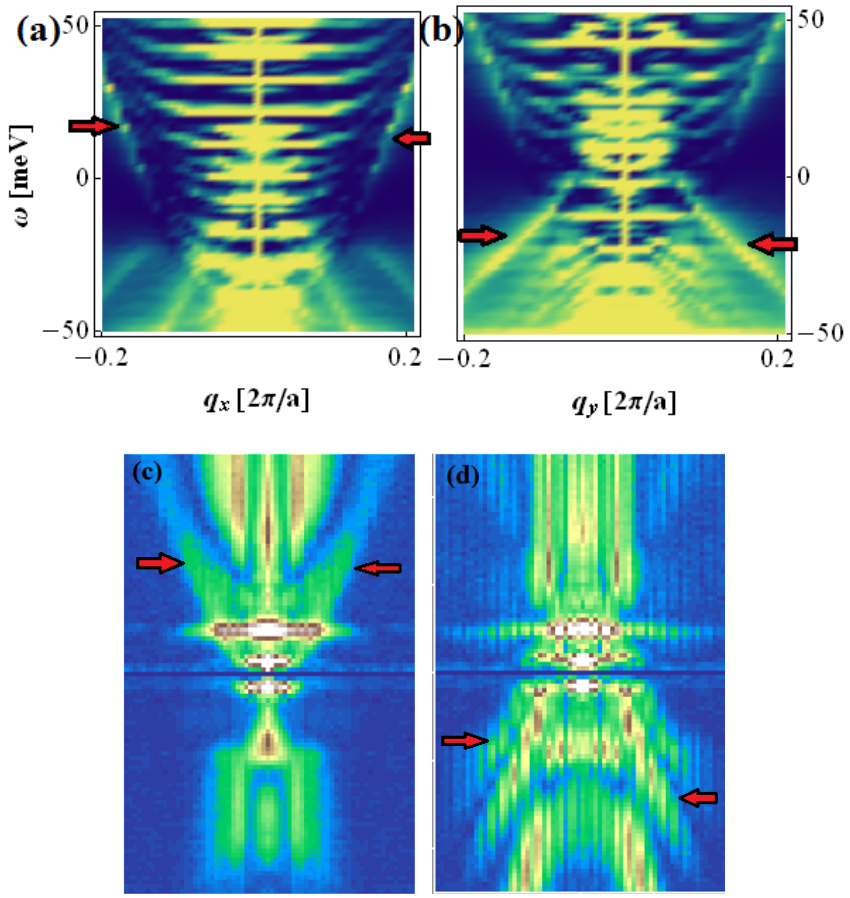

Figure 5.9: Line cuts along constant $(q_x, 0)$ and $(0, q_y)$ of $\mathrm{P}(\mathbf{q}, \omega)$. **(a-b)** Our FT-LDOS line cuts. **(c-d)** FT-STM line cuts from [27].

and scattering vectors from other pockets completely removed. We will devote the following chapters to explaining this phenomenon.

The most simple solution follows from the impurity potential itself. Consider the full T-matrix result in the Born limit, $T \to V_0$, applicable to our small impurity potential,

$$\delta A(\boldsymbol{q}, \omega) = -\frac{1}{\pi} \operatorname{Tr} \operatorname{Im} \left[\sum_{\boldsymbol{k}} \mathbf{G}^0(\boldsymbol{k} + \boldsymbol{q}, \omega) \mathbf{V_0} \mathbf{G}^0(\boldsymbol{k}, \omega) \right], \tag{5.13}$$

where thus far we have considered $\mathbf{V_0}$ diagonal in the orbital basis with equal elements $V_0^{\mu\nu} = V_0 \delta_{\mu,\nu}$. If we instead allow these elements to vary, i.e. by setting $V_0^{yz} > V_0$, we would enhance scattering between points on the constant energy contours of yz character. This is directly

evident in the JDOS approximation

$$\delta JDOS(\boldsymbol{q},\omega) = \sum_{k,\mu} V_0^{\mu\mu} A_0^{\mu\mu}(\boldsymbol{k}+\boldsymbol{q},\omega) A_0^{\mu\mu}(\boldsymbol{k},\omega) \tag{5.14}$$

$$\approx \sum_{k} V_0^{yzyz} A_0^{yzyz}(\boldsymbol{k}+\boldsymbol{q},\omega) A_0^{yzyz}(\boldsymbol{k},\omega), \tag{5.15}$$

i.e. the boost of the yz scattering potential yields dominant contributions to the QPI pattern from the convolution of $A_0^{yzyz}(\boldsymbol{q})$. This *orbitally selective scattering* was suggested independently by Sprau et al. [28] and Hanaguri et al. [27], who performed explicit calculations of the JDOS using a grid of k-points and similar band structures. The line cuts of these JDOS images match closer with the FT-STM. We include supporting high resolution JDOS calculations performed by Kreisel [41] in Figure 5.10, showing line cuts obtained for a diagonal scattering potential $V_0^{\mu\mu} = V_0$ in **(a-b)**, and for a purely yz scattering potential $V_0^{\mu\mu} = \delta_{\mu yz} V_0$. The full JDOS calculation is similar to our real space variant as expected, with dispersing features at both high and low energies in line cuts along both directions. The yz selective JDOS, on the other hand, mirrors closely the anisotropy observed in the experimental line cut of 5.9 **(c-d)**, with broad dispersive features along k_x only for positive energies, and broad dispersive features along k_y only for negative energies. We can consider the origin of this effect using our example above, the FT-LDOS displayed in Figure 5.7. We show the orbitally resolved constant energy contours in the yz and xz orbital in Figure 5.11. The yz weight contributes only to the Y pocket, and orbitally selective scattering will thus only include scattering vectors from this pocket. The corresponding scattering vector yielding peaks along k_x is suppressed in this situation, and the QPI pattern becomes extremely unidirectional as observed in experiment. The JDOS line cuts demonstrate that this situation is replicated in the entire energy range.

Inducing orbitally selective scattering in this manner by tuning the impurity potential components seems intuitive and closely matches experiment, yet the assumption of in-equal scattering potential components used in the JDOS calculations is not well-founded. We have earlier argued that the lattice impurity is an iron site vacancy, and would assume that this should be modeled by a diagonal scattering potential. In order to accept the above QPI explanation we require some way of generating an effective impurity potential with $V_0^{yz} > V_0^{\mu} \; \forall \; \mu$. In the following chapter we will investigate whether such an effective potential can be generated from correlations.

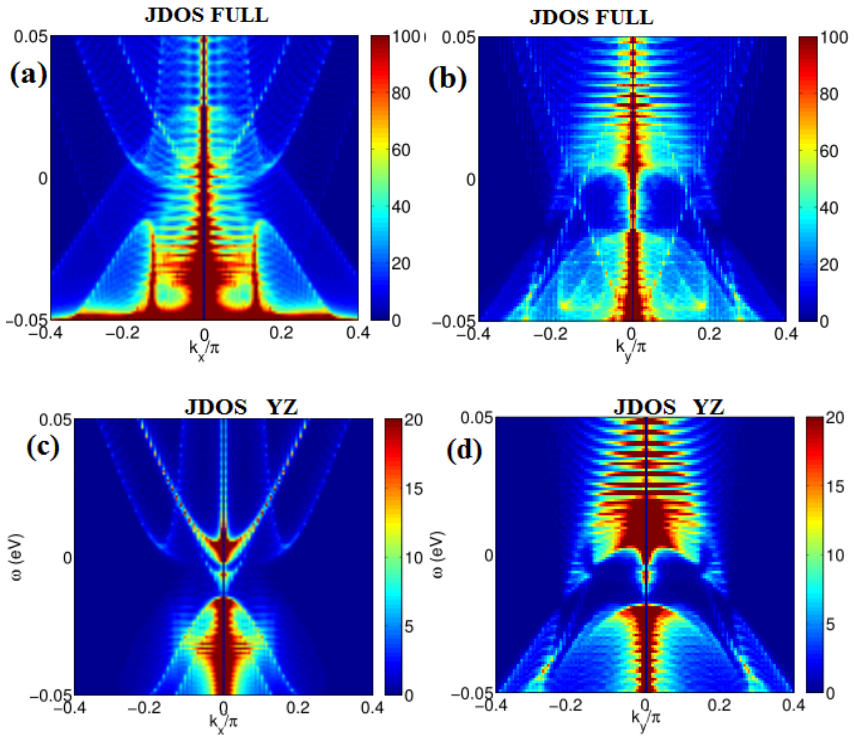

Figure 5.10: k-space direct calculation of the JDOS. **(a-b)** JDOS with a diagonal impurity potential $V_0^{\mu\mu} = V_0$. **(c-d)** JDOS with a purely yz scattering potential $V_0^{\mu\mu} = \delta_{\mu yz} V_0$. Calculation and plots constructed by [41].

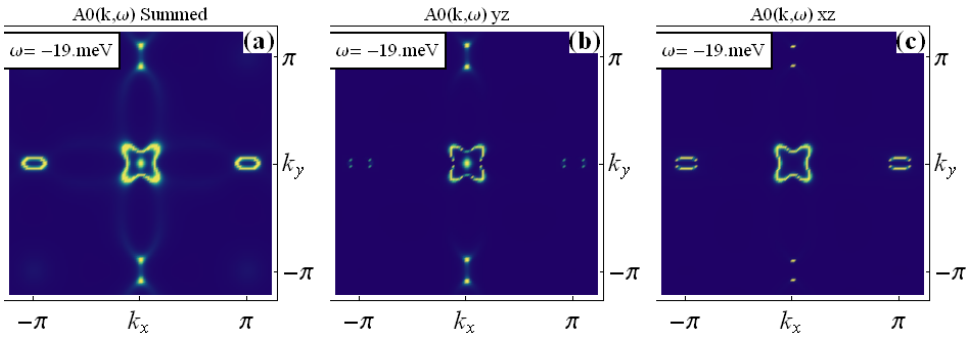

Figure 5.11: The orbitally resolved $A^0(\boldsymbol{q}, \omega)$. Certain scattering vectors are enhanced if the impurity potential selects scattering from the corresponding part of the constant energy contour pockets. **(a)** The summed $A^0(\boldsymbol{q}, \omega)$. **(b)** The yz orbital $A_0^{yzyz}(\boldsymbol{q}, \omega)$. **(c)** The xz orbital $A_0^{xzxz}(\boldsymbol{q}, \omega)$.

Chapter 6

Locally Nucleated Magnetization from Interactions

FeSe does not display the usual magnetic phase under the structural transition of other FeSCs, but still demonstrates dominant $(\pi, 0)$ spin fluctuations. We have so far treated the electron correlations in the metal with an effective band, which is a valid description as long as we do not cross this phase transition. The added impurity potential changes this situation, as it locally changes electronic environment, possibly leading to *local* magnetic order. The correlations are too weak to induce the stripe ordered state on the entire lattice, but the impurity site may nucleate a local magnetization with the same ordering. This local stripe order is inherently C_2, and may be the missing component generating the strongly unidirectional features seen in the FT-STM. We will highlight the differences from long range ordered state, where renormalization to the Fermi surface pocket has been proposed as the origin of the unidirectional features observed in the FT-STM in other FeSCs[42]. This does not explain the corresponding features in FeSe, where the stripe state does not emerge, but motivates the study of local stripe order in relation to QPI.
Our specific goal in this chapter is to induce the local order by including correlations in the form of the Hubbard-Hund model. We will then show how the system with local magnetic order corresponds to the non-interacting system with an effective scattering potential different from the initial delta function scatterer.

6.1 Unidirectional QPI Features Emerging from Magnetic Stripe Order

Unidirectional QPI features are not unique to FeSe. STM measurements in $Ca(Fe_{1-x}Co_x)_2As_2$ by Chuang et al. [43] found similarly dispersing FT-STM features, which we include in Figure 6.1 **(a-j)**. The electronic structure in this system is fundamentally different from the situation in FeSe due to the stripe ordered phase emerging below the nematic transition, a transition shown in **(l)**. Knolle et al. [42] proposed an explanation of these unidirectional QPI features in terms of the altered constant energy contours. The initial Fermi surface, consisting of the four

electron elliptical pockets and the central hole pocket, is folded into a C_2 structure by finite mean fields connecting the X and Γ pockets, preserving the Y pockets. The schematic Fermi surface is shown in **(m)**. This folding creates new scattering vectors along k_x, which we would expect to yield unidirectional dispersing peaks in a T-Matrix calculation. Such a calculation was performed for both potential and magnetic scattering potentials, yielding the dispersing peaks seen in **(n)**-**(o)**. We must reiterate at this point that stripe order is not observed in FeSe, and as such this proposed explanation is not directly applicable to our investigation. Instead, we will locally nucleate a stripe order region of finite extension, which will correspond to an extended scattering potential but does not lead to the Fermi surface renormalization seen in the long range ordered phase. [42].

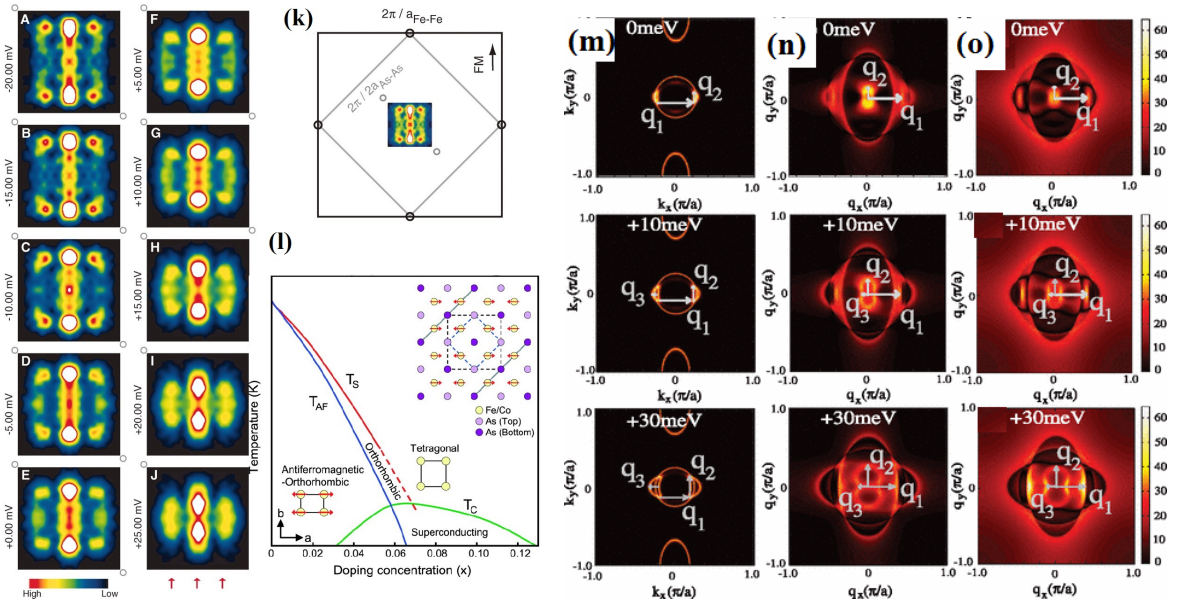

Figure 6.1: **(a)**-**(j)** Unidirectional dispersing features observed in FT-STM in the stripe order phase of $Ca(Fe_{1-x}Co_x)_2As_2$. **(k)** Orientation in the 2Fe B.Z. **(l)** Phase diagram of $Ca(Fe_{1-x}Co_x)_2As_2$ displaying the stripe order phase emerging below the nematic phase. **(m-o)** Explanation of the QPI features by including stripe order in the T-Matrix calculation, demonstrating in **(m)** how the $(\pi, 0)$ stripe order folds the outer electron pockets into the Γ pocket, yielding new dominant scattering vectors. **(n)** Result of the k-space T-matrix calculation for a non-magnetic impurity, demonstrating unidirectional features arising from the folding of the Fermi surface pockets. **(m)** Similar features arise for the purely magnetic scattering potential. Reproduced with slight modifications from [43] and [42].

6.2 Ten band Model for FeSe

The close competition between magnetic orders in the utilized band structure of [19] could potentially destroy our sought after C_2 magnetization if the band implementation is not precise.

To match the band used for the $(\pi, 0)$ peaked spin susceptibility calculation we expand to the ten band model, and include the effects of spin orbit coupling with $\lambda = 20$meV. The two distinct pockets on the resulting Fermi surface are shown below, with the X and Y pockets combined to yield a propeller like formation at the M point. In order to compare with the previous five band results we continue to show physical quantities in the 1Fe coordinate system, and note that the scattering vectors should be similar to the previously obtained results for the five band system. We will demonstrate this fact by including the ten band model FT-LDOS in the noninteracting system in the following chapter. The following investigation of local order could have been performed in the five band model with near-identical results, and we emphasize that the extension to the ten band model was primarely performed in order to include small shifts to the tight binding model and include other variants of the orbital order terms. These alternations to the band structure shifted the magnetic instability to (π, π) and as such were inconsistent with the local stripe order scenario investigated here, prompting us to continue with the unaltered band structure of [19].

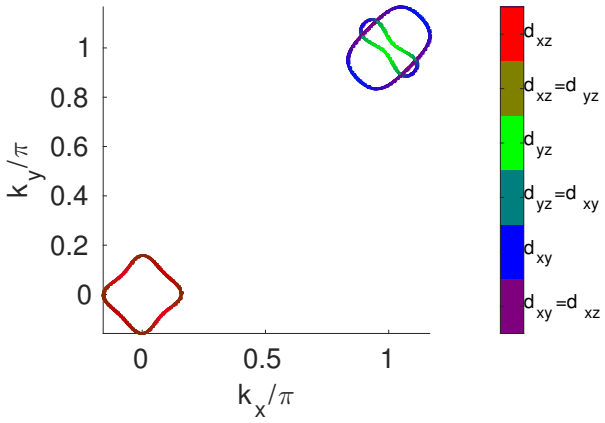

Figure 6.2: Fermi surface in the ten band model. The X and Y points fold on top of each other, creating the combined pocket at the M point. The set of dominant scattering vectors should be similar to that of the five band model, which will be evident in later QPI calculations. Reproduced from [19].

6.3 The Hubbard-Hund model

We have previously introduced the single band Hubbard model, which approximates the full set of electron-electron Coulomb interactions by an effective local repulsion for electrons of opposite spin, setting an energy cost for double occupancy of a single lattice site. The interaction is local or *onsite* because the electronic wavefunction overlap between neighboring sites is considered small, yielding vanishing interactions between e.g. nearest neighbours. We will introduce the extension to multiorbital systems below, following [44].
In the multi-orbital system electrons can occupy the same site in different orbitals, which we

capture by adding to the standard Hubbard term a new repulsive interaction

$$H_{UU'} = U \sum_{i,\mu} n_{i\mu\uparrow} n_{i\mu\downarrow} + \frac{U'}{2} \sum_{i,\mu\neq\nu,\sigma} n_{i\mu\sigma} n_{i\nu\bar{\sigma}}, \tag{6.1}$$

where $U > 0$ disfavors electrons in the same orbital on the same site (and in each orbital), and $U' > 0$ disfavors electrons on the same site in different orbitals.
Two electrons can move around in these orbitals limited by the Pauli principle, yielding an exchange term, the so-called Hund's rule coupling

$$H_J = \frac{J}{2} \sum_{i,\mu\neq\nu,\sigma} c^\dagger_{i\mu\sigma} c^\dagger_{i\nu\bar{\sigma}} c_{i\mu\bar{\sigma}} c_{i\nu\sigma} + c^\dagger_{i\mu\sigma} c^\dagger_{i\nu\sigma} c_{i\mu\sigma} c_{i\nu\sigma} \tag{6.2}$$

$$= \frac{J}{2} \sum_{i,\mu\neq\nu,\sigma} c^\dagger_{i\mu\sigma} c^\dagger_{i\nu\bar{\sigma}} c_{i\mu\bar{\sigma}} c_{i\nu\sigma} - n_{i\mu\sigma} n_{i\nu\sigma}, \tag{6.3}$$

where the sign change follows from the anti-commutation of the fermionic operators. It is evident that the latter part of this expression favors the parallel alignment of spins in different orbitals. We also include an exchange term corresponding to the pair hopping of two electrons in the same orbital (and hence with opposite spins)

$$H_{J'} = \frac{J'}{2} \sum_{i,\mu\neq\nu,\sigma} c^\dagger_{i\nu\sigma} c^\dagger_{i\mu\bar{\sigma}} c_{i\nu\bar{\sigma}} c_{i\nu\sigma}. \tag{6.4}$$

Removing the double counting inherent in the $\mu \neq \nu$ notation and rearranging terms, the full interaction term becomes

$$H_{int} = +U \sum_{i,\mu} n_{i\mu\uparrow} n_{i\mu\downarrow} \tag{6.5}$$

$$+ U' \sum_{i,\mu<\nu,\sigma} n_{i\mu\sigma} n_{i\nu\bar{\sigma}} \tag{6.6}$$

$$+ (U' - J) \sum_{i,\mu<\nu,\sigma} n_{i\mu\sigma} n_{i\nu\sigma} \tag{6.7}$$

$$+ J \sum_{i,\mu<\nu,\sigma} c^\dagger_{i\mu\sigma} c^\dagger_{i\nu\bar{\sigma}} c_{i\mu\bar{\sigma}} c_{i\nu\sigma} \tag{6.8}$$

$$+ J' \sum_{i,\mu<\nu,\sigma} c^\dagger_{i\nu\sigma} c^\dagger_{i\mu\bar{\sigma}} c_{i\nu\bar{\sigma}} c_{i\nu\sigma} \tag{6.9}$$

Indeed this seemingly arbitrary collection of terms is the full onsite interaction Hamiltonian. Interactions between the electrons in a solid are in general described in terms of electronic field operators $\psi_\sigma = \sum_\mu \sum_i \psi_{\mu i}(r) c_{\mu i}$, with $\psi_{\mu i}(r)$ the wave function of an orbital μ in the multiband system on site i, and the sum extends over the full lattice. The electron-electron interaction

Hamiltonian then takes the form

$$H_{ee} = \frac{1}{2}\sum_{\sigma,\sigma'}\int\int \mathrm{d}r\,\mathrm{d}r'\,\psi^\dagger_\sigma(r)\psi^\dagger_{\sigma'}(r')V(r-r')\psi_{\sigma'}(r)\psi_\sigma(r'). \tag{6.10}$$

The well-localized nature of the iron d-orbitals leads us to limit ourselves to onsite interaction, resulting in the above Hamiltonian with four non-vanishing matrix elements (U, U', J, J') due to the symmetries of the d-orbitals.
We fix $J = J' = U/4$ in correspondence with [19], and additionally demand $U' = U - 2J$ due to spin rotation invariance. The model is treated on the mean field level, decoupling in the density and exchange channels in all four fermion operator terms above

$$\left\langle c^\dagger_{m'}c^\dagger_m c_n c_{n'}\right\rangle = +\left\langle c^\dagger_{m'}c_{n'}\right\rangle c^\dagger_m c_n + c^\dagger_{m'}c_{n'}\left\langle c^\dagger_m c_n\right\rangle \tag{6.11}$$

$$-\left\langle c^\dagger_{m'}c_n\right\rangle c^\dagger_m c_{n'} - c^\dagger_{m'}c_n\left\langle c^\dagger_m c_{n'}\right\rangle \tag{6.12}$$

$$+\,\text{constant}, \tag{6.13}$$

yielding

$$H^{MF}_{int} = \sum_{\nu,\sigma}[U\langle n_{\nu\bar\sigma}\rangle + \sum_{\mu\neq\nu}U'\langle n_{\mu\bar\sigma}\rangle + (U-J)\langle n_{\mu\sigma}\rangle]c^\dagger_{\nu\sigma}c_{\nu\sigma} \tag{6.14}$$

$$-\sum_{\mu\neq\nu,\sigma}[(U'-J)\left\langle c^\dagger_{\nu\sigma}c_{\mu\sigma}\right\rangle + J'\left\langle c^\dagger_{\mu\bar\sigma}c_{\nu\bar\sigma}\right\rangle + J\left\langle c^\dagger_{\nu\bar\sigma}c_{\mu\bar\sigma}\right\rangle]c^\dagger_{\mu\sigma}c_{\nu\sigma} \tag{6.15}$$

$$-\sum_{\nu,\sigma}[U\left\langle c^\dagger_{\nu\sigma}c_{\nu\bar\sigma}\right\rangle + J\sum_{\mu\neq\nu}\left\langle c^\dagger_{\mu\sigma}c_{\mu\bar\sigma}\right\rangle]c^\dagger_{\nu\bar\sigma}c_{\nu\sigma} \tag{6.16}$$

$$-\sum_{\mu\neq\nu,\sigma}[U'\left\langle c^\dagger_{\nu\sigma}c_{\mu\bar\sigma}\right\rangle + J'\left\langle c^\dagger_{\mu\sigma}c_{\nu\bar\sigma}\right\rangle]c^\dagger_{\nu\bar\sigma}c_{\nu\sigma}. \tag{6.17}$$

These terms can be implemented in our CBdG model by expanding the Nambu vector to include spin, doubling the full matrix dimension. We will induce local magnetization by tuning the Hubbard U close to the critical value of the magnetic phase transition U_c. The emerging phases are characterized by the set of ordering vectors $\boldsymbol{Q}_i$ with finite amplitude m_{Q_i}, i.e. we write the (in-plane) magnetization

$$m(\boldsymbol{r}) = \sum_{Q_l} m_{\boldsymbol{Q}_l}e^{i\boldsymbol{Q}_l\cdot\boldsymbol{r}}. \tag{6.18}$$

The strength of different ordering components is captured in the Fourier transform

$$m(\boldsymbol{q}) = \sum_{Q_l}\sum_i e^{-i\boldsymbol{q}\boldsymbol{r}_i}m_{\boldsymbol{Q}_l}e^{i\boldsymbol{Q}_l\cdot\boldsymbol{r}_i} \tag{6.19}$$

$$= \sum_{Q_l} m_{\boldsymbol{Q}_l}\delta_{\boldsymbol{q},\boldsymbol{Q}_l}. \tag{6.20}$$

Self-consistent calculation for varying values of this potential in our system of interest yields $U_c = 0.355$eV, defined as the value where the magnetization converges to a finite value. Above this value the system is in the $\boldsymbol{Q} = (\pi, 0)$ phase, as expected for the utilized band structure in the nematic phase.

6.4 Locally Nucleated Magnetization

Our selfconsistent CBdG method provides the onsite orbitally resolved densities and magnetization mean fields. We initialize the system with a central spin polarized ($m_z(r) = m_0$ for $r < 10a$) region and track the convergence of the mean fields, which is reached in approximately 200 iterations. We find a finite local magnetization centered on the impurity for $U > 0.28$eV, which increases as we approach U_c. The spatial distribution of this magnetization is shown for different values of U in Figure 6.3 **(a)** below. The magnetization is initially C_4, and becomes increasingly C_2 as the instability is approached, which is demonstrated in Figure 6.3 **(b)**-**(c)**, where we perform line cuts of the magnetization along $(0, y)$ and $(x, 0)$ which displays a discrepancy in magnitude **(b)** which is plotted directly in **(c)**. The magnetization becomes increasingly anisotropic as the strength of the correlations is increased, which is evident as we move down the rows. We are interested in boosting anisotropic scattering, and thus tune the Hubbard U close to U_c, inducing a local $(\pi, 0)$ stripe order.

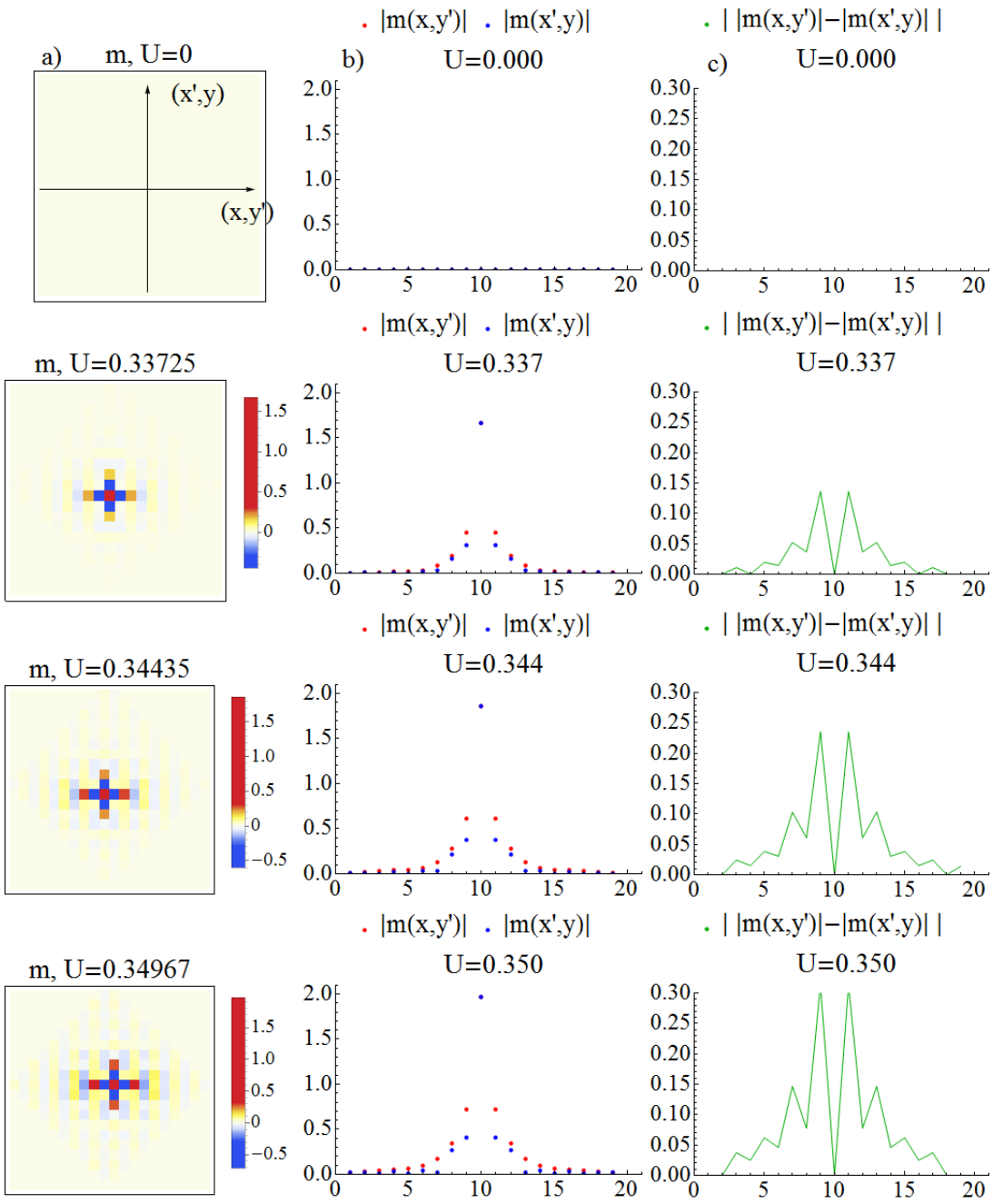

Figure 6.3: **(a)** Locally nucleated magnetization around the impurity site, **(b)** line cuts through the impurity along the x and y axes, and **(c)** the difference in magnetization magnitude along the axes. The rows are different values of the Hubbard U approaching U_c, demonstrating the increase in anisotropy. Nothing is nucleated below a lower critical field $U \approx 0.28$eV.

6.5 Effective Impurity Potentials

The simplest explanation for the anisotropic scattering is the introduction of orbital selectivity by the impurity potential itself. As we have seen, the nearly complete enhancement of $yz - yz$ scattering seems most consistent with the experimental results, and we will thus investigate whether our local stripe order can dress the bare impurity potential and create this effect. This effective impurity potential formalism was proposed in [15], where the disordered interacting system with a local central impurity was mapped to a homogeneous system with new effective magnetic and nonmagnetic scattering potentials.
We consider the full Hamiltonian

$$H = (H_{tb} + H_{OO} + H_{SO}) \tag{6.21}$$
$$+ H_{imp} + H_{int}, \tag{6.22}$$

where the first three terms correspond to H^0, i.e. the homogeneous system. The impurity term disturbs this system, an effect which is boosted by the near-critical interactions. The general form of magnetic and nonmagnetic scattering potentials are

$$H_{imp} = \sum_{\nu,\sigma} V_\nu c^\dagger_{i^*\nu\sigma} c_{i^*\nu\sigma} + I \sum_{\nu,\sigma} \sigma S_\nu c^\dagger_{i^*\nu\sigma} c_{i^*\nu\sigma}, \tag{6.23}$$

where i^* denotes the central impurity site, and we fix $V_\nu = 0.1$ eV and $IS_\nu = 0$ eV $\forall\nu$, since the impurity is most likely a non-magnetic iron-site vacancy.
Following [15], we can rewrite the mean field decoupled Hubbard Hund Hamiltonian in terms of the charge and spin densities

$$n_{i\nu} = \sum_\sigma \langle n_{i\nu\sigma} \rangle , \tag{6.24}$$
$$m_{i\nu} = \sum_\sigma \sigma \langle n_{i\nu\sigma} \rangle , \tag{6.25}$$

which yields

$$H^{MF}_{int} = \frac{1}{2} \sum_{\nu\neq\mu,i\sigma} [U n_{i\nu} + (2U - 5J) n_{i\mu}] c^\dagger_{i\nu\sigma} c_{i\nu\sigma} \tag{6.26}$$
$$- \frac{1}{2} \sum_{\nu\neq\mu,i\sigma} \sigma [U m_{i\nu} + J m_{i\mu}] c^\dagger_{i\nu\sigma} c_{i\nu\sigma}, \tag{6.27}$$

where we limit ourselves to the non-spin flip terms since the induced magnetization is completely collinear, i.e. $\left\langle c^\dagger_\uparrow c_\downarrow \right\rangle = 0$.
We then split the charge and spin densities into homogeneous system values and disorder induced

parts as

$$n_{i\nu} = n^0_{i\nu} + \Delta n_{i\nu}, \tag{6.28}$$
$$m_{i\nu} = m^0_{i\nu} + \Delta m_{i\nu}, \tag{6.29}$$

with the bare spin and charge densities obtained from the site furthest from the central impurity in the interacting system. The full Hamiltonian can then be rewritten

$$H = H^0 + H^{MF}_{int}(n^0, m^0) + H^{MF}_{int}(\Delta n, \Delta m) + H_{imp} \tag{6.30}$$
$$= H^0 + H^0_{int}(n^0, m^0) + \widetilde{H}_{imp}(\Delta n, \Delta m) \tag{6.31}$$

In this way the disordered system is mapped to a homogeneous system with effective impurity potentials

$$\widetilde{V}_{i\nu} = V_\nu \ \delta_{i^* i} + \frac{1}{2}\left(U\Delta n_{i\nu} + (2U - 5J)\sum_{\nu\neq\mu}\Delta n_{i\mu}\right) \tag{6.32}$$
$$= V_\nu \ \delta_{i^* i} + V_{ind,i\nu} \tag{6.33}$$
$$\widetilde{I}\widetilde{S}_{i\nu} = IS_\nu \ \delta_{i^* i} - \frac{1}{2}\left(U\Delta m_{i\nu} + J\sum_{\nu\neq\mu}\Delta m_{i\mu}\right) \tag{6.34}$$
$$= IS_\nu \ \delta_{i^* i} + I_{ind}\Delta s_{i\nu}. \tag{6.35}$$

We are then back on common ground in terms of our QPI analysis, since we consider a homogeneous system with added impurity terms.

In Figure 6.4 we show the spatial distribution of these effective potentials obtained in the systems considered above with two near-critical values of the Hubbard U. **(a-c)** are the effective magnetic potentials shown in the **(a)** xz and **(b)** yz orbitals along with the summed value in **(c)**. These are extended in space, with large values extending out several lattice sites. The potential is approximately C_4, and appears similar in the xz and yz orbitals, mirroring the summed value.
The induced non-magnetic scattering potential is displayed in **(d)-(f)**. The onsite value is negative, which cancels out parts of the bare scattering potential V_0 in the total effective scattering potential $V_{ind}(r) + V_0\delta(r-0)$. Apart form this onsite feature there is a mostly C_4 spatial extension around the impurity site, and resolving the potential in orbital components we see again similar potentials for xz and yz.
This situation is mostly replicated when the Hubbard U is increased, as shown in **(g)-(l)**. The effective potentials are stronger, with the magnetic potential extending further out, but we emphasize that the orbital components are still similar. The magnetic potential retains more of the C_2 character of the stripe magnetization itself, but this effect is still minuscule.

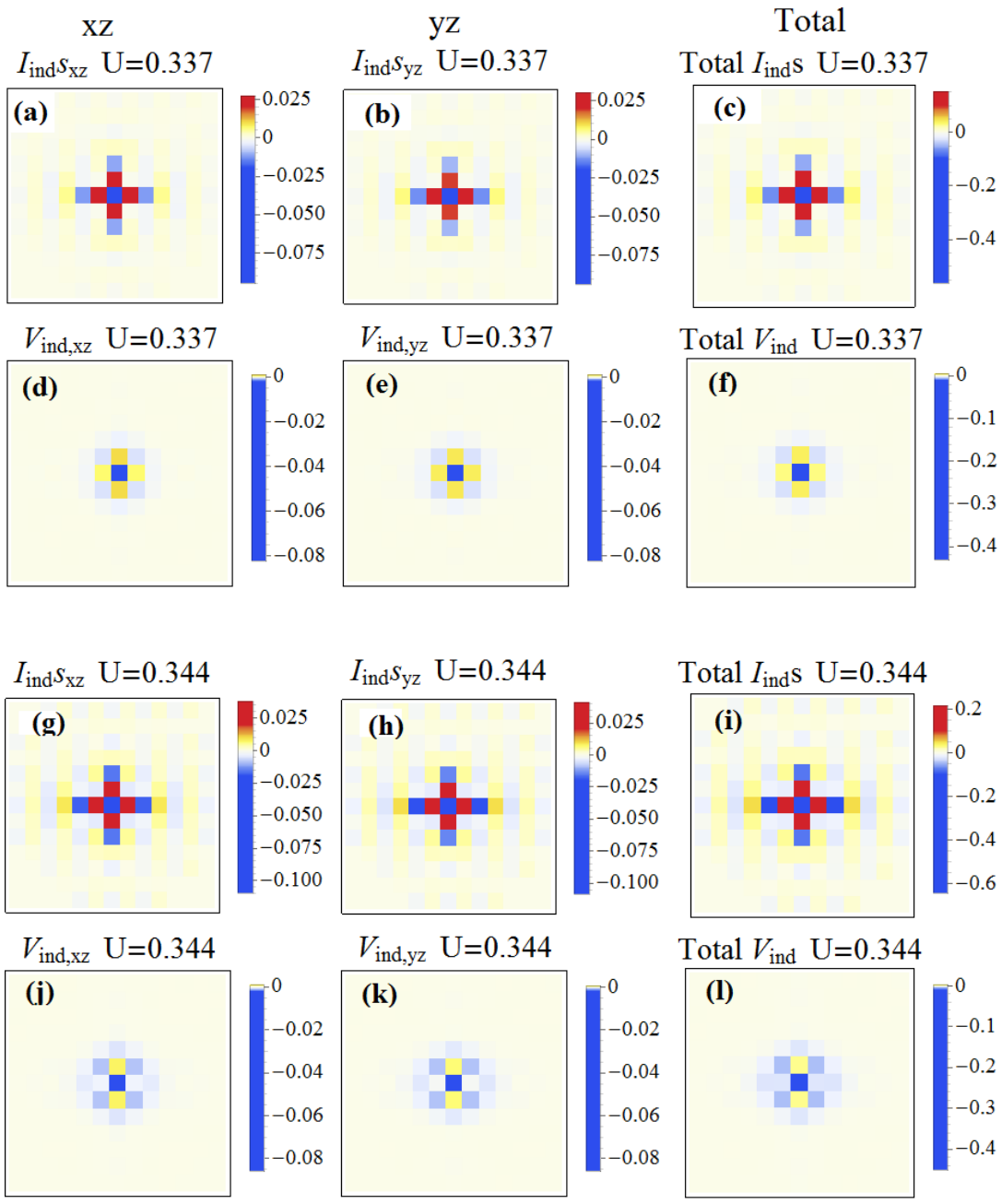

Figure 6.4: Effective nonmagnetic and magnetic xz and yz impurity potentials for two different values of U. The potentials are identical in the xz and yz orbitals

6.6 Summary

In this chapter we have investigated a possible mechanisms for boosting x and y unidirectionality in the FT-LDOS by creating an effective scattering potential. We attempt to induce this effect by successfully nucleating a local stripe order by including interactions in the Hubbard Hund model. The resulting magnetization is clearly $(\pi, 0)$ and the spatial distribution of the magnetization amplitude is C_2 symmetric.
We have demonstrated how this interacting system can be mapped to the noninteracting system with effective magnetic and non-magnetic scattering potentials which are extended in space. The two scattering potentials are of similar magnitude, and show small degrees of unidirectionality in the spatial distribution. Orbitally selective scattering does not appear directly from these effective potentials, as the xz/yz splitting is minuscule.
In the following chapter we will nevertheless continue the analysis by doing the direct QPI calculation using the selfconsistent CBdG method in the presence of the magnetic puddle, which will show whether the anisotropic spatial distribution and addition of a magnetic scattering potential can induce the extremely unidirectional features observed in experiment.

Chapter 7

Quasiparticle Interference with Interactions

We have thus far developed the tools required to study quasiparticle interference in the presence of locally nucleated magnetic order around the central scattering potential. This analysis is efficiently performed in our real space formalism.
In this chapter we initially discuss the ten band FT-LDOS in the non-interacting system for comparison purposes, so as to eliminate effects stemming from the ten band vs five band model when presenting our QPI patterns in the interacting system. We will then present results for the interacting system with local magnetic order, and compare the emerging features to experiment. The extended scattering potential is found to suppress long range features, leaving only a central broad FT-LDOS peak centrally, which is missing the dispersing features seen in the non-interacting system. Additionally we find a ring structure emerging at low energies, a sharp feature which is incompatible with the experimental results. We will argue that this is a strong argument for the absence of local magnetic order in the nematic phase of FeSe.

7.1 Ten band Comparison for the Noninteracting System

We perform calculation in a square lattice of 2-iron unit cells of dimension 42×42, equivalent in number of lattice sites to approximately a 60×60 1-iron unit cell square lattice. When showing physical quantities we rotate this system to align with the five band coordinate system as shown in Figure 7.1 **(a)**, where the rotated system resembles a diamond (marked by the red lines) when rotated to the old coordinate system. The empty regions outside these red lines are simply included for plotting purposes, and do not contain lattice sites. The FT-LDOS ($P(q, \omega)$ is included **(b-c)**, and demonstrates the dispersing streaks seen for the five band model, moving outwards as the energy is increased. The long range features are also reproduced, with the features at $(\pm\pi, 0)$ and $(0, \pm\pi)$ removed when the central hole pockets disappears, in agreement with the five band result. This is what we expected for this calculation, as the five band model generally yields similar results to the full ten band model, including the experimental comparisons performed in [19]. We include it here simply for comparison purposes with the similar calculation in the interacting system, where we can exclude the slightly modified band

structure as the source of discrepancies when discussing novel QPI features.

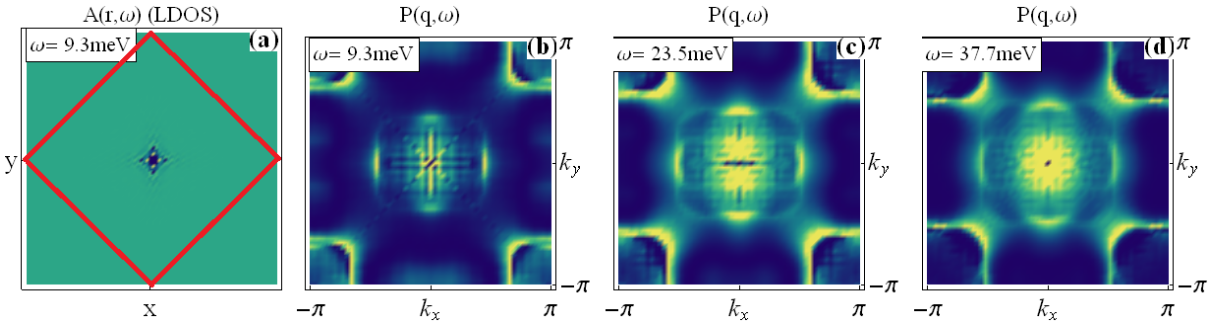

Figure 7.1: The ten band model reproduces the QPI patterns observed for the five band model, as expected. **(a)** LDOS displayed with the axes aligned with the 1Fe unit cell. **(b)-(d)** FT-LDOS at positive energies demonstrating dispersing peaks.

7.2 Quasiparticle Interference from Nematogen Scattering

Turning to the interacting system, we repeat the procedure of the preceding chapter, inducing a local magnetic order centered on the impurity site. This magnetic puddle is shown in Figure 7.2 **(a)** along with the Fourier transform, which has peaks at $(\pi, 0)$ in **(b)**, demonstrating the stripe nature of the local magnetic order. Line cuts of the magnetization and the relative magnetization amplitude in **(c,d)** show the spatial extension of this puddle, which has an extended bell-like shape centered on the impurity, slightly elongated along k_x. This elongation is still a minor feature at this near-critical value of U, and we expect unidirectional effects in the FT-LDOS to arise from the anisotropic nature of the stripe order itself.

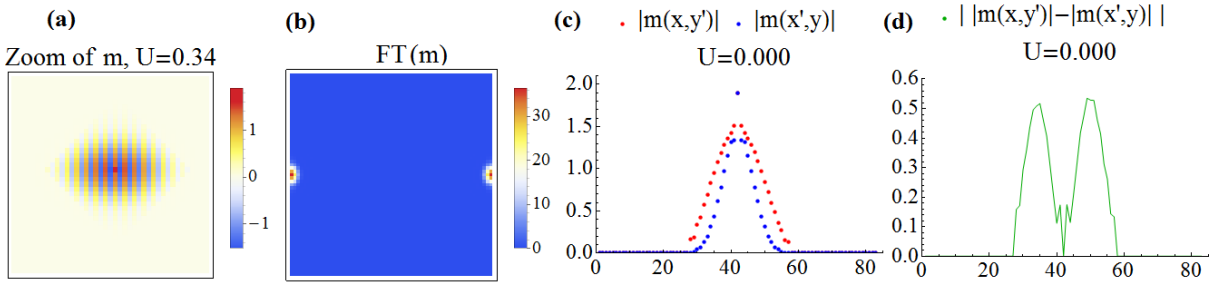

Figure 7.2: Real space image of the nucleated magnetization on the central impurity in the interacting system, the Fourier transform of this magnetization displaying peaks at $(\pm\pi, 0)$, and line cuts through the central impurity demonstrating the unidirectionality.

The selfconsistent CBdG-QPI procedure introduced previously is repeated for the system

of converged mean fields, yielding the local density of states on each site. This is then Fourier transformed, and the amplitude is plotted as $P(\boldsymbol{q}, \omega)$. The obtained LDOS for decreasing energies is shown in Figure 7.3 **(a)**-**(f)**, along with the FT-LDOS. For high energies, in **(a)**-**(c)**, the LDOS is dominated by the strong enhancement near the locally nucleated magnetization. We note that the lack of long ranged features is not a color scale issue, since line cuts through the impurity site demonstrate that the LDOS far from the impurity site is featureless. The corresponding FT-LDOS has none of the features previously found, and consists of a single sharp Gaussian peak at the Γ point, and small weight at the M points. These features appear inconsistent with experiment, with no long range dispersing features.
Decreasing the bias further we find new features emerging in **(d)**, with a periodic modulation in the LDOS, and a corresponding circular feature in the FT-LDOS. This circle expands in **(e)**-**(f)**, revealing a weak central propeller-like structure inside. This novel feature is also in disagreement with the experimental QPI data, where the similar FT-STM pattern consist of a broad central peak with dispersing features moving out along k_y. Additional calculations including scattering from smaller effective potentials indicate the universality of this feature, which consistently emerges at ≈ -18meV.

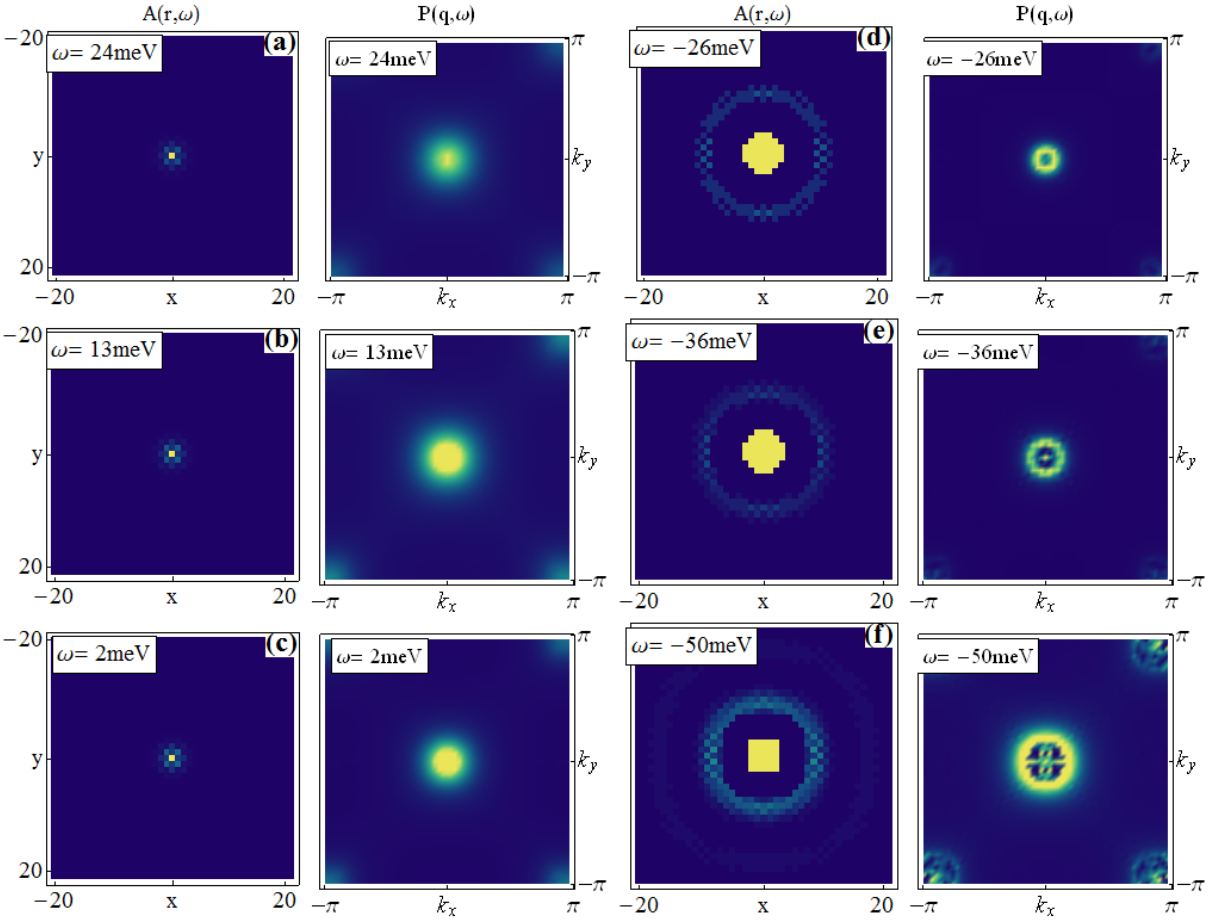

Figure 7.3: LDOS and corresponding FT-LDOS obtained from the interacting system including the central local stripe order. The sharp peak at the center at high biases expands into a circle at low energies. These features are inconsistent with the experimental results presented earlier.

7.3 Interpretation in Terms of the Effective Scattering Potentials

Our inclusion of locally nucleated magnetic order does not appear to enhance anisotropic scattering as was found for the bulk ordered phase, yielding mostly C_4 features in the FT-LDOS. At high energies the long range inter pocket and medium range intra pocket dispersing features which we found for the noninteracting system in both the five and ten band models are missing, in clear disagreement with the experimental FT-STM patterns. We can interpret the absence of these features in terms of the extending form of the effective scattering potentials, produced using the formalism of the preceding chapter.
For our calculations in the non-interacting system we modeled the impurity by a delta function

potential, which scatters equally to all points in k-space,

$$V(\boldsymbol{q}) = \sum_{r_i} e^{-i\boldsymbol{k}\cdot\boldsymbol{r}_i}\delta(\boldsymbol{r}-0)V_0 \tag{7.1}$$

$$= V_0. \tag{7.2}$$

In the T-Matrix (Born) formulation this removes impurity potential effects in the spectral function,

$$\delta A(\boldsymbol{q},\omega) \propto V(\boldsymbol{q}) \sum_k \operatorname{Im} G^0(\boldsymbol{k}+\boldsymbol{q},\omega) G^0(\boldsymbol{k}+\boldsymbol{q},\omega) \tag{7.3}$$

$$= V_0 \operatorname{Im} G^0(\boldsymbol{k}+\boldsymbol{q},\omega) G^0(\boldsymbol{k}+\boldsymbol{q},\omega), \tag{7.4}$$

i.e. $P(\boldsymbol{q},\omega)$ modulations arises solely from the quasiparticle interference of the Green's function product. If the effective potential has real space structure, i.e. a broad Gaussian peak centered at the origin, the Fourier transform will be a *sharp* Gaussian k-space potential

$$V(\boldsymbol{r}) = \frac{1}{\sqrt{2\pi\sigma^2}} e^{-\boldsymbol{r}^2/(2\sigma^2)} \Rightarrow \tag{7.5}$$

$$V(\boldsymbol{q}) = e^{-\frac{1}{2}\sigma^2\boldsymbol{q}^2}. \tag{7.6}$$

This superimposes a structure on the FT-LDOS

$$\delta A(\boldsymbol{q},\omega) \propto V(\boldsymbol{q}) \sum_k \operatorname{Im} G^0(\boldsymbol{k}+\boldsymbol{q},\omega) G^0(\boldsymbol{k}+\boldsymbol{q},\omega), \tag{7.7}$$

which in this specific case enhances QPI features in a sharp peak at the center. This masks information about dominant scattering vectors at larger q than the width of this distribution, and would explain the above lack of features.

A more quantitative analysis obtained by considering the exact shape of the effective potentials, which are included in Figure 7.4, showing the non-magnetic **(a)** and magnetic **(c)** parts. The non-magnetic potential ($V(r)$) is the superposition of the bare scattering potential $V_0(r) = \sum_\mu V_0^\mu \delta(r-0)$, and a induced negative Gaussian peak centered on the impurity site. This diminishes the delta function scattering potential on the impurity site itself. By the above argument this Gaussian background leaves the FT-LDOS with a central sharp peak which dominates all other features, i.e. it dominates the scattering induced by the diminished constant contribution ($V_0 - |V_{ind}(0)|$). The exact form of $V(\boldsymbol{q})$ is included in **(b)**, demonstrating the sharp central peak and a small constant contribution (black in the figure is slight above 0). The real space anisotropy which leaves the potential elongated along x induces a k-space potential which is narrower along q_x than q_y, as expected.

Turning to the magnetic potential we have to add an additional structure to the real space

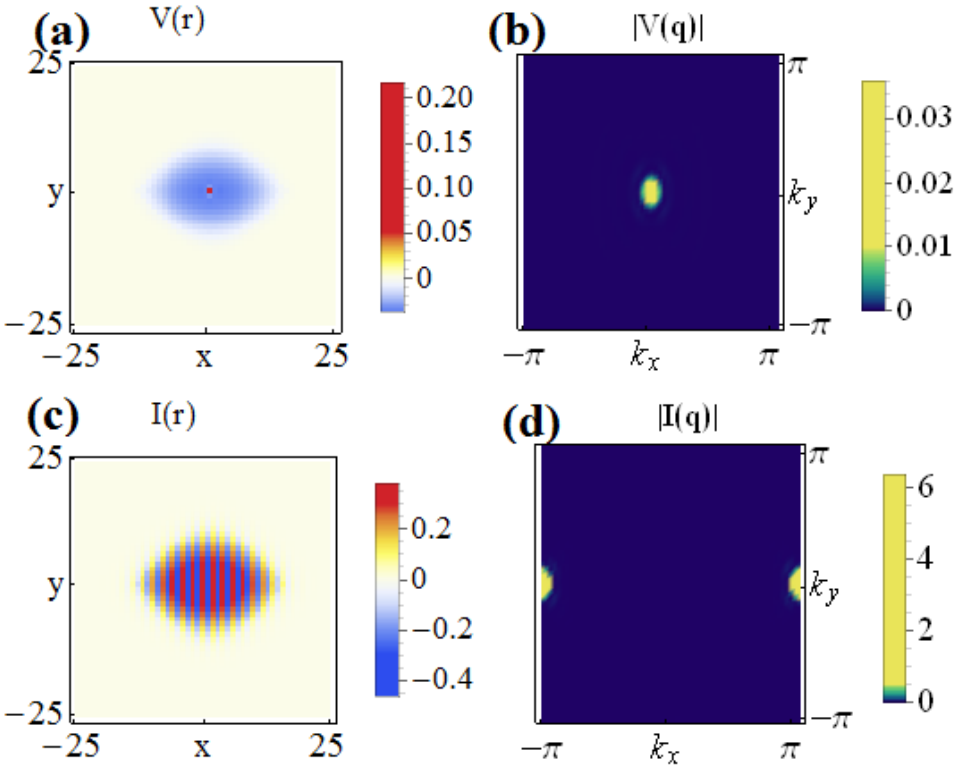

Figure 7.4: Effective **(a)** non-magnetic and **(c)** magnetic scattering potentials. The non-magnetic impurity potential is a broad negative Gaussian distribution with a central positive delta function peak. The bare delta function potential is diminished by the induced effective potential, and the Fourier transform in **(b)** is a small constant potential scattering all over k-space, with a superimposed Gaussian at the center. The magnetic impurity is a broad stripe ordered Gaussian distribution, and the corresponding $I(q)$ is narrowly peaked at $(\pm\pi, 0)$.

potential, i.e. the stripe order. This yields

$$I(\boldsymbol{r}) = \frac{1}{\sqrt{2\pi\sigma^2}} e^{-\boldsymbol{r}^2/(2\sigma^2)} e^{i\boldsymbol{Q}\cdot\boldsymbol{r}} \Rightarrow \tag{7.8}$$

$$I(\boldsymbol{q}) = e^{-\frac{1}{2}\sigma^2(\boldsymbol{q}-(\pi,0))^2}, \tag{7.9}$$

which is a sharp Gaussian extending from $(\pm\pi, 0)$. The exact form of this potential is included in **(d)**, demonstrating the exact extension of these sharp peaks.
This analysis goes a long way in explaining the obtained results, with the extended shape of the non-magnetic potential boosting the central sharp peak seen in the FT-LDOS. The expanding circle at low energies must then arise from the appearance in the constant energy contours of well-nested C_4 symmetric scattering vectors, which will only be visible if the small intra-pocket scattering is missing or diminished.

7.4 Summary and Outlook

In this chapter we have investigated the nucleation of local stripe order as a boosting mechanism for unidirectional QPI features. Our calculations yield sharp central Gaussian peaks at high energies, with no apparent structure and no dispersing large q features. It is possible that structure in these central peaks is hidden by the chosen broadening, but the small extension and C_4 symmetry would still leave them inconsistent with unidirectional features. At low energies an expanding circular feature emerges, which is also not observed in the FT-STM. These novel structures can be interpreted as a consequence of the broad spatial distribution of the effective impurity potentials induced by the local magnetic order, which enhances parts of the quasiparticle interference pattern centered on the Γ point. We conclude that the locally nucleated stripe order scattering scenario is unlikely as the cause for the extremely C_2 QPI features and by extension argue that local magnetic order is not nucleated in FeSe, which we would expect to induce the high energy sharp Gaussian and low energy circular features. Local magnetic order instead seems to induce features with C_4 symmetry in the QPI patterns, in sharp contrast to the experimental result.
This leaves the question of the boosted unidirectional QPI features open. We have previously found good agreement with dispersing scattering vectors in the entire considered energy range, and originally turned to the orbital character of the impurity potential as a way of generating the orbitally selective scattering, which most closely matches experiment in our utilized band structure. There is no reason to assume a large splitting in the orbital components of the bare impurity potential, and our present calculations indicate that this is not generated by nucleation of local magnetic order. We must then turn to the other quantity controlling the QPI features, i.e. the bare Green's function itself. In the following chapter we will analyze this quantity within Fermi liquid theory, and argue that the orbital selectivity arises from a correlation induced orbital splitting in the quasiparticle weight not included in our current model, which leads directly to orbital selectivity within the QPI formalism.

Chapter 8

Orbitally Selective Scattering

Our investigations into the unidirectional quasiparticle interference features observed in the nematic phase of FeSe has led us to the concept of orbitally selective scattering. In effect we propose that the QPI features can be reproduced by our utilized band structure by boosting scattering between constant energy regions of primarily yz character. As we presented in the Chapter 6, the orbitally selective impurity potential was not generated by correlations, with no large xz/yz anisotropy in the potential or magnetic channels. An alternative explanation based on the spatial distribution of the effective scattering potential was proved insufficient in chapter 7, failing to reproduce any experimental features and explicitly predicting new dominant features inconsistent with the FT-STM. This led us to consider orbital selectivity arising from the bare Green's function itself.
In this chapter we will consider the validity of describing excitations in terms of well-defined quasiparticles in the presence of electronic correlations, which is the foundation of Fermi liquid theory. We will present the renormalized form of the Green's function and relate this quantity to quasiparticle interference. Lastly we will present how the lifting of xz/yz orbital degeneracy in the nematic phase can in turn lift the degeneracy of the orbitally resolved quasiparticle weight, which translates directly to orbital selectivity in the QPI.

8.1 Fermi Liquid Theory

We have thus far considered quasiparticle interference using the bare Green's function

$$G^0(\boldsymbol{k},\omega) = \frac{1}{\omega - \xi_k + i\eta}, \tag{8.1}$$

Non-negligible correlations in FeSe have so far been included for this quantity by renormalizing ξ_k to match experimental probes of the band structure. We will presently consider the Green's function in the interacting system in more detail, writing it on the general form

$$G^R(\boldsymbol{k},\omega) = \frac{1}{\omega - \xi_k - \operatorname{Re}\Sigma^R(k,\omega) - i\operatorname{Im}\Sigma^R(k,\omega)}, \tag{8.2}$$

with $\xi_k = \frac{k^2}{2m} - \mu$ the free electron energy, and $\Sigma^R(k,\omega)$ the retarded self energy arising from the electronic correlations. It is immediately clear that the band-tuning procedure outlined in chapter 4 simply amounts to ignoring the energy dependence of real part of the self energy as well as the entire imaginary part, i.e. we have set $\xi_k \to \xi_k - \mathrm{Re}\,\Sigma^R(k,0)$ and fixed the broadening to the constant η. We will consider the validity of this procedure below.
Defining an effective Fermi wave vector $\tilde{k}_F$ by the condition $\xi_k - \mathrm{Re}\,\Sigma^R(\tilde{k}_F,0) = 0$, and expanding to first order around $\omega = 0$ and $k - \tilde{k}_F = 0$, we can write the retarded Green's function as [20]

$$G^R(\boldsymbol{k},\omega) \approx \frac{Z}{\omega - \widetilde{\xi}_k + \frac{i}{2\tau_k(\omega)}}, \tag{8.3}$$

with

$$Z^{-1} = 1 - \partial_\omega \,\mathrm{Re}\,\Sigma^R(\tilde{k}_F,\omega)|_{\omega=0}, \tag{8.4}$$

$$\widetilde{\xi}_k = \frac{1}{m^*}(k - \tilde{k}_F)\tilde{k}_F, \tag{8.5}$$

$$\frac{m}{m^*} = Z\left(1 + \frac{m}{\tilde{k}_F}\partial_k \,\mathrm{Re}\,\Sigma(k,0)|_{k=\tilde{k}_F}\right), \tag{8.6}$$

$$\frac{1}{\tau_k} = -2Z\,\mathrm{Im}\,\Sigma^R(k,\omega). \tag{8.7}$$

Approximating a small broadening $\mathrm{Im}\,\Sigma^R(k,\omega) = \eta << 1$, valid within RPA [20], the spectral function is

$$A(k,\omega) = 2\pi\frac{Z\eta}{(\omega - \widetilde{\xi}_k)^2 + (Z\eta)^2} \tag{8.8}$$

$$\approx 2\pi Z\delta(\omega - \widetilde{\xi}_k), \text{ for } \eta \to 0. \tag{8.9}$$

It is important to note that this is not the full spectral function, as normalization requires

$$\int_{-\infty}^{\infty}\frac{d\omega}{2\pi}A(k,\omega) = 1, \tag{8.10}$$

but

$$\int_{-\infty}^{\infty}\frac{d\omega}{2\pi}2\pi Z\delta(\omega - \widetilde{\xi}_k) = Z < 1, \tag{8.11}$$

which means that we are neglecting part of the spectrum not described by sharp quasiparticle excitations when writing the Green's function in the form of equation 8.3 above. There is thus spectral weight outside the quasiparticle picture, which we describe by some function $A'(k,\omega)$ with weight $(1-Z)$, i.e. we set

$$A(k,\omega) = 2\pi Z\delta(\omega - \widetilde{\xi}_k) + (1-Z)A'(k,\omega) \tag{8.12}$$

We are thus left with a spectrum of quasiparticles with long lifetimes and other excitations which are not well-described by a free particle-like Lorentzian peak [20].

8.2 Influence on QPI patterns

The above propagator describes the system without disorder. Renaming this new Green's function $\tilde{G}^0$, the LDOS modulation is now found by substituting $G^0 \to \tilde{G}^0$ in the earlier T-Matrix result

$$\delta A(\boldsymbol{q},\omega) = -\frac{1}{\pi}\,\mathrm{Im}\left[\tilde{G}^0(\boldsymbol{k}+\boldsymbol{q},\omega)\tilde{T}(\omega)\tilde{G}^0(\boldsymbol{k},\omega)\right], \tag{8.13}$$

where the T-matrix is renormalized by including the new Green's function in the same manner. For small scattering potentials the Born approximation holds, yielding in the multiorbital case

$$\delta A(\boldsymbol{q},\omega) = -\frac{1}{\pi}\,\mathrm{Tr}\,\mathbf{V_0}\,\mathrm{Im}\left[\tilde{\mathbf{G}}^0(\boldsymbol{k}+\boldsymbol{q},\omega)\tilde{\mathbf{G}}^{\mathbf{0}}(\boldsymbol{k},\omega)\right] \tag{8.14}$$

$$= -\frac{1}{\pi}\,\mathrm{Tr}\,\mathbf{Z^2V_0}\,\mathrm{Im}\left[\mathbf{G}^0(\boldsymbol{k}+\boldsymbol{q},\omega)\mathbf{G}^{\mathbf{0}}(\boldsymbol{k},\omega)\right] \tag{8.15}$$

, (8.16)

where we have extracted the quasiparticle weight, leaving our earlier form of the bare Green's function. The quasiparticle weight is a 10×10 matrix in orbital space, and we see that it enters exactly as the impurity potential, directly controlling the orbital selectivity. It follows that if e.g. we set $Z^{yz,yz} >> 1$, the contribution to the total $\delta A(q,\omega)$ would be dominated by $yz-yz$ scattering.

The question then boils down to the matrix elements of the quasiparticle weight in the orbital basis. The quasiparticle weight is in general set by the strength of correlations, with the limits of free particles $Z=1$ and e.g. the Mott insulating state $Z=0$ on opposite ends. Orbital selectivity in the quasiparticle weight is then equivalent to the lifting of degeneracy between the strength of correlations for electrons in different orbitals. Theoretical and experimental investigations of this phenomenon have found a linear relationship between the orbital component of the quasiparticle weight and the filling of the corresponding orbital, i.e. $Z^{\mu,\mu} \propto n_\mu$ [45]. This is illustrated in the theoretical curves of 8.1, where the orbitally resolved fillings and the correspond quasiparticle weight components in a $BaFe_2As_2$ band structure model are plotted for increasing correlation strengths. The inclusion of finite crystal field splitting lifts the degeneracy in fillings between the xy and the xz/yz (still degenerate) orbitals, and these differences expand with the Hubbard U. The orbitally resolved quasiparticle weights follow the density splitting in a linear fashion, leading to large $Z^{xy}-Z^{yz/xz}$ differences in the intermediate correlation regime.
In the nematic phase of FeSe the dominant splitting is between the xz and yz orbitals in the form of orbital order, which indicates a dominant Z^{yz} component. As we have seen, this directly induces orbitally selective scattering, providing the foundation for the calculation performed by

Kreisel [41] in Figure 5.10, which closely matched the experimental line cuts. Quantitative fits of the quasiparticle weight to experimental quantities, such as the observed gap structure, using our initial band structure but including also the Z factor supports this scenario with $Z^{yz} > Z^{xy/x^2-y^2/z^2} > Z^{xz}$. Initial T-Matrix calculations including these Z factors in the fully renomalized bare Green's function indicate consistent unidirectional QPI features matching experiment [41].

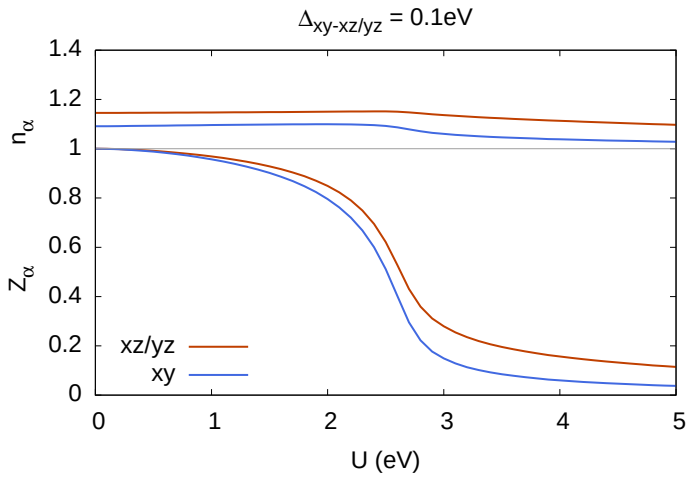

Figure 8.1: Orbitally resolved quasiparticle weight $Z^{\alpha\alpha}$ and orbitally resolved filling n_α (upper curves) as a function of the Hubbard U for a band structure model of $BaFe_2As_2$ with finite crystal field splitting. The orbitally resolved filling degeneracy is lifted by the crystal field, an effect which is increased as the strength of correlation is increased. The quasiparticle weights track these split curves. In FeSe the splitting is between the xz and yz orbitals, yielding dominant Z^{yz} weight and thus orbital selectivity in the quasiparticle interference features. Reproduced from [45]

8.3 Summary

In this chapter we have proposed an origin of orbitally selective scattering in the nematic phase of FeSe in terms of the lifting of orbital degeneracy in the orbitally resolved quasiparticle weight. This mechanism explains the discrepancy between the calculated QPI features for the utilized band and that found in experiment, as this lifted degeneracy between components of Z is an effect outside the tuning of the band. It also elucidates why the anisotropic features appear in the nematic phase of FeSe, by tying the lifting of yz/xz degeneracy directly to the degree of orbital selectivity.

Chapter 9

Conclusions

In this master's thesis we have investigated recent experimental STM results demonstrating long range unidirectional modulations in the local density of states in the nematic phase of FeSe. The unidirectional features are captured in the Fourier transform of the STM, demonstrating small q peaks dispersing in along q_x for positive bias and out along q_y as the applied bias is decreased below 0.
We have interpreted these long range LDOS modulations in terms of the interference of quasiparticles scattering on a central impurity potential. These features arise from enhanced scattering vectors on the constant energy contours, a result first obtained by Friedel and later applied to the superconducting phase of the cuprates with the octet model. We have attempted to capture these effects by using an experimentally tuned 5 band tight binding model for the FeSe layers including the introduction of orbital ordering in the nematic phase, breaking the d_{xz}/d_{yz} degeneracy of the tetragonal phase. As demonstrated, this distorts the constant energy contour pockets, creating unidirectional scattering vectors.

In an effort to obtain QPI patterns comparable to experiment, i.e. the FT-LDOS, we have performed selfconsistent calculations of the LDOS on a lattice using the recently developed Chebyshev-Bogoliubov-de Gennes method. Our new implementation of this method for the study of QPI enables the calculation of QPI features in large systems in finite time, reaching as large as 100×100 systems in the five band model. This enables us to reach the high q-space resolution required for reproducing of the experimental features, which is not possible using the standard BdG real space formalism. Our reproductions of the octet model result of dispersing FT-LDOS peaks indicate that the Chebyshev expansion of the Green's function with controlled broadening is a valid technique for these types of calculations.

Using this method for the FeSe band structure we have presented QPI patterns within the entire experimental energy range. These images include FT-LDOS peaks of different weights dispersing along the q_x and q_y axes in an anisotropic fashion, which can be mapped directly to the anisotropic expansion of constant energy contour pockets. Long range features in the FT-LDOS are also captured in the form of inter-pocket scattering vectors. Line cuts capturing the dispersing peak positions in q-space are similar to the experiment results, but our FT-LDOS

results are found to retain more C_4 character in contrast to the strictly unidirectional dispersion observed in STM. We have concluded that our model provides correct scattering vectors arising from the constant energy contour pockets, which are captured well in the FT-LDOS, and found that the experimental results can be reproduced by inducing orbitally selective scattering dominated by the $yz - yz$ component. This last conclusion was based on the supporting k-space T-Matrix calculation performed by Kreisel [41].
This led to the hypothesis of an orbitally selective scattering potential $V_0 \rightarrow V_{eff}$ with $V_{eff}^{yzyz} > V_0$. We have attempted to induce this effective potential by including local magnetic order nucleated around the impurity site by electronic correlations. Tuning the Hubbard U close to the critical value of the long range stripe $(\pi, 0)$ order we found such magnetization emerging. This inhomogeneous system was then mapped to the earlier system, but including spatially extended non-magnetic and magnetic effective scattering potentials. We found these effective potential to be isotropic in the orbital basis, and thus not directly responsible for orbital selectivity in the FT-LDOS. We nevertheless performed the CBdG-QPI calculations with these extended potentials, but found emerging features inconsistent with experiment. These inconsistent features were explained in terms of the extended scattering potentials, which we found enhance scattering at the Γ point and effectively reduce all large q features.

Failing to induce orbital selectivity from the impurity potential itself, we instead turned to the renormalization of the non-interacting Green's function itself, including the quasiparticle weight not included in the utilized band structure. This Z factor was found to directly control orbital selectivity in a similar manner to the scattering potential. Theoretical and experimental investigations of this quantity in the presence of correlations have found that the orbital components Z^{μ} are proportional to the fillings in the same orbitals n_{μ}. In the nematic phase of FeSe these fillings are split by the introduction of orbital order, favoring the yz orbital. This yields dominant Z^{yz} and thus directly induces orbitally selective scattering. To summarize, this indicates that the experimental QPI can be explained in terms of the FT-LDOS in the orbitally ordered nematic phase band, by including explicitly the splitting of the quasiparticle weight components. We conclude that the unidirectional features we set out to explain can be understood in terms of quasiparticle interference with the nematic band structure including s and d-wave orbital order, when including explicitly the orbitally non-degenerate correlation strengths induced by this same orbital order.

Appendix A

Chebyshev expansion notes

A.1 Positivity of the kernel

Consider the positive 2π periodic function $p(\phi)$,

$$p(\phi) = \left| \sum_{\nu=0}^{N-1} a_v e^{i\nu\phi} \right|^2 \tag{A.1}$$

$$= \sum_{\nu,\mu} a_\nu a_\mu (\cos((\nu-\mu)\phi) + i\sin((\nu-\mu)\phi)) \tag{A.2}$$

$$= \sum_{\nu=0}^{N-1} a_\nu^2 + 2\sum_{n=1}^{N-1}\sum_{\nu=0}^{N-1-n} a_\nu a_{\nu+n}\cos(n\phi) \tag{A.3}$$

$$= g_0 + \sum_{n=1}^{N-1} g_n \cos(n\phi) \tag{A.4}$$

where the odd sine term disappears and the even cosine term is rewritten using $n = \nu - \mu$. Now, p is positive so the following expression is likewise

$$0 \leq \frac{1}{2}[p(\arccos(x) + \arccos(y)) + p(\arccos(x) - \arccos(y))] \tag{A.5}$$

$$= g_0 + \sum_{n=1}^{N-1} g_n [\cos(n(\arccos(x) + \arccos(y))) \tag{A.6}$$

$$+ \cos(n(\arccos(x) - \arccos(y)))]$$

$$= g_0 + \sum_{n=1}^{N-1} g_n \cos(n\arccos(x))\cos(n\arccos(y)) \tag{A.7}$$

$$= g_0 + \sum_{n=1}^{N-1} g_n T_n(x) T_n(y) \tag{A.8}$$

and the kernel is then positive if the moments are on the form $g_n = \sum_{\nu=0}^{N-1} a_\nu a_{\nu+n}$.

A.2 Lorentz kernel coefficients

Setting $a_\nu = e^{-\lambda\nu/N}$, consider the definition of sine hyperbolic, $\sinh(x) = (1 - e^{-2x})/(2e^{-x})$. Summing the geometric series we obtain

$$g_n = \sum_{\nu}^{N-n-1} e^{-\lambda\nu/N} e^{-\lambda(\nu+n)/N} \tag{A.9}$$

$$= e^{-\lambda n/N} \sum_{\nu}^{N-n-1} e^{-2\lambda\nu/N} \tag{A.10}$$

$$= e^{-\lambda+\lambda(1-n/N)} \frac{1 - e^{-2\lambda(1-n/N)}}{1 - e^{-2\lambda/N}} \tag{A.11}$$

$$= \frac{e^{-\lambda}}{1 - e^{-2\lambda/N}} \frac{2}{2} \frac{1 - e^{-2\lambda(1-n/N)}}{e^{-\lambda(1-n/N)}} \tag{A.12}$$

$$= \frac{\sinh(\lambda(1 - n/N))}{\sinh(\lambda)} \tag{A.13}$$

Note that these moments fulfill the normalized kernel requirement, i.e. $g_0 = 1$.'

A.3 CBdG Mean Fields

In this section we will consider in detail how to obtain the CBdG mean fields from the expanded Green's function. This is essentially equivalent to the calculation done in Bruus and Flensberg [20] but was motivated by the unconventional way in which the superconducting order parameter was presented in Möckli and Mello [46], which we were initially unable to reproduce. In essence, the full calculation of mean fields from the Green's function was repeated to reproduce correctly the factor $(1 - 2f(\omega))$. The Green's function to be expanded in Chebyshev polynomials is

$$\bar{G}^{12}(\omega) = \lim_{\eta\to 0} \langle c_\uparrow | \frac{1}{\omega + i\eta - \mathcal{H}} | c_\downarrow \rangle \tag{A.14}$$

$$= G^{12R}(\omega). \tag{A.15}$$

The η limit is utilized to take the limit of a Lorentzian in the expansion.
Define the anomalous Green's functions

$$G^{12>}(t,0) = -i \langle c_\uparrow(t) c_\downarrow(0) \rangle \tag{A.16}$$

$$G^{12<}(t,0) = i \langle c_\downarrow(0) c_\uparrow(t) \rangle \tag{A.17}$$

$$G^{12R}(t,0) = -i\theta(t) \langle \{c_\uparrow(t) c_\downarrow(0)\} \rangle \tag{A.18}$$

$$= \theta(t) \left[G^{12>}(t,0) - G^{12<}(t,0) \right]; \tag{A.19}$$

All operators are in the Heisenberg presentation $A(t) = e^{iHt}Ae^{-iHt}$.
In Lehmann representation:

$$G^{12>}(t,0) = -\frac{i}{Z}\sum_{nn'}\langle n|c_\uparrow e^{-iHt}c_\downarrow|n\rangle\, e^{-\beta E_n}e^{iE_nt} \tag{A.20}$$

$$= -\frac{i}{Z}\sum_{nn'}\langle n|c_\uparrow|n'\rangle\,\langle n'|c_\downarrow|n\rangle\, e^{-\beta E_n}e^{i(E_n-E_{n'})t} \tag{A.21}$$

and

$$G^{12<}(t,0) = \frac{i}{Z}\sum_{nn'}\langle n|c_\downarrow e^{iHt}c_\uparrow|n\rangle\, e^{-\beta E_n}e^{-iE_nt} \tag{A.22}$$

$$= \frac{i}{Z}\sum_{nn'}\langle n|c_\downarrow|n'\rangle\,\langle n'|c_\uparrow|n\rangle\, e^{-\beta E_n}e^{-i(E_n-E_{n'})t} \tag{A.23}$$

$$= \frac{i}{Z}\sum_{nn'}\langle n'|c_\uparrow|n\rangle\,\langle n|c_\downarrow|n'\rangle\, e^{-\beta E_n}e^{-i(E_n-E_{n'})t} \tag{A.24}$$

$$= \frac{i}{Z}\sum_{nn'}\langle n|c_\uparrow|n'\rangle\,\langle n'|c_\downarrow|n\rangle\, e^{-\beta E_{n'}}e^{i(E_n-E_{n'})t} \tag{A.25}$$

$$\tag{A.26}$$

Fourier transforming, we obtain

$$G^{12>}(\omega) = -\frac{2\pi i}{Z}\sum_{nn'}\langle n|c_\uparrow|n'\rangle\,\langle n'|c_\downarrow|n\rangle\, e^{-\beta E_n}\delta(E_n - E_{n'} + \omega) \tag{A.27}$$

and

$$G^{12<}(\omega) = \frac{2\pi i}{Z}\sum_{nn'}\langle n|c_\downarrow|n'\rangle\,\langle n'|c_\uparrow|n\rangle\, e^{-\beta E_n}\delta(E_n - E_{n'} - \omega) \tag{A.28}$$

$$= \frac{2\pi i}{Z}\sum_{nn'}\langle n'|c_\downarrow|n\rangle\,\langle n|c_\uparrow|n'\rangle\, e^{-\beta E_{n'}}\delta(E_{n'} - E_n - \omega) \tag{A.29}$$

$$= \frac{2\pi i}{Z}\sum_{nn'}\langle n|c_\uparrow|n'\rangle\,\langle n'|c_\downarrow|n\rangle\, e^{-\beta(E_n+\omega)}\delta(E_n - E_{n'} + \omega) \tag{A.30}$$

$$= -G^{12>}e^{-\beta\omega} \tag{A.31}$$

Now,

$$G^{12R}(\omega) = \int dt e^{i(\omega+i\eta)t}\theta(t)(G^{12>}(t,0) - G^{12<}(t,0)) \tag{A.32}$$

$$= -\int_0^\infty dt\ e^{i(\omega+i\eta)t}\frac{i}{Z}\sum_{nn'}\langle n|c_\uparrow|n'\rangle\langle n'|c_\downarrow|n\rangle(e^{-\beta E_n} + e^{-\beta E'_n})e^{i(E_n - E_{n'})t} \tag{A.33}$$

$$= \frac{1}{Z}\sum_{nn'}\frac{\langle n|c_\uparrow|n'\rangle\langle n'|c_\downarrow|n\rangle}{\omega + i\eta + E_n - E_{n'}}(e^{-\beta E_n} + e^{-\beta E_{n'}}). \tag{A.34}$$

Using

$$\mathrm{Im}\,\frac{1}{x+i\eta} = -\frac{\eta}{x^2+\eta^2} \to -\pi\delta(x), \tag{A.35}$$

we define a new quantity

$$B(\omega) = -2\,\mathrm{Im}\,G^{12R}(\omega) \tag{A.36}$$

$$= \frac{2\pi}{Z}\sum_{nn'}\langle n|c_\uparrow|n'\rangle\langle n'|c_\downarrow|n\rangle(e^{-\beta E_n} + e^{-\beta E_{n'}})\delta(\omega + E_n - E_{n'}) \tag{A.37}$$

$$= \frac{2\pi}{Z}\sum_{nn'}\langle n|c_\uparrow|n'\rangle\langle n'|c_\downarrow|n\rangle(e^{-\beta E_n} + e^{-\beta(E_n+\omega)})\delta(\omega + E_n - E_{n'}) \tag{A.38}$$

$$= \frac{2\pi}{Z}\sum_{nn'}\langle n|c_\uparrow|n'\rangle\langle n'|c_\downarrow|n\rangle e^{-\beta E_n}(1 + e^{-\beta\omega})\delta(\omega + E_n - E_{n'}) \tag{A.39}$$

$$= -iG^{12>}(\omega)(1 + e^{-\beta\omega}) \tag{A.40}$$

$$= i(1 + e^{\beta\omega})G^{12<}(\omega), \tag{A.41}$$

which yields

$$G^{12>} = -iB(\omega)(1 - f(\omega)), \tag{A.42}$$

$$G^{12<} = iB(\omega)f(\omega). \tag{A.43}$$

The mean field of interest is

$$\Delta/V = \langle c_\uparrow c_\downarrow\rangle \tag{A.44}$$

$$= iG^{12>}(0,0) \tag{A.45}$$

$$= i\int\frac{d\omega}{2\pi}\,G^{12>}(\omega) \tag{A.46}$$

$$= \frac{1}{2\pi}\int d\omega\ B(\omega)(1 - f(\omega)) \tag{A.47}$$

$$= -\frac{1}{\pi}\int d\omega\ \mathrm{Im}\,G^{12R}(\omega)(1 - f(\omega)) \tag{A.48}$$

The singlet order parameter is

$$\langle c_\uparrow c_\downarrow \rangle - \langle c_\downarrow c_\uparrow \rangle = i(G^{12>}(0) + G^{12<}(0)) \tag{A.49}$$

$$= \frac{1}{2\pi} \int d\omega \; B(\omega)((1 - f(\omega)) - f(\omega)) \tag{A.50}$$

$$= -\frac{1}{\pi} \int d\omega \; \operatorname{Im} G^{12R}(\omega)(1 - 2f(\omega)) \tag{A.51}$$

In terms of the order parameter

$$\langle c_\downarrow c_\uparrow \rangle = -\frac{1}{2}[\langle c_\uparrow c_\downarrow \rangle) - \langle c_\downarrow c_\uparrow \rangle)] \tag{A.52}$$

$$= -\frac{1}{2}[-\frac{1}{\pi} \int d\omega \; \operatorname{Im} G^{12R}(\omega)(1 - 2f(\omega))] \tag{A.53}$$

$$= \frac{1}{2\pi} \int d\omega \; \operatorname{Im} G^{12R}(\omega)(1 - 2f(\omega)) \tag{A.54}$$

Which coincides with the result of D. Möckli et. al. [46]

Appendix B

Other

B.1 Spin Orbit Interaction

The $3d^6$ orbitals of iron are written out in terms of $Y_{lm} = |lm\rangle = |m\rangle$, with $l = 2(\text{d})$[47]. The angular momentum operators can now be written in the basis of d orbitals using the known eigenvalues of the Y_{lm} functions above, yielding L_x, L_y, L_z. Finally, the spin orbit interaction in the spin basis becomes.

$$\lambda_{SO} \sum_i \boldsymbol{L} \cdot \boldsymbol{S} = \lambda_{SO} \sum_i \frac{1}{2} \boldsymbol{L} \cdot \boldsymbol{\sigma} \tag{B.1}$$

$$= \frac{1}{2} \lambda_{SO} \begin{pmatrix} L_z & L_x - iL_y \\ L_x + iL_y & -L_z \end{pmatrix} \tag{B.2}$$

which can be directly implemented in the CBdG Hamiltonian.

Bibliography

[1]H. K. Onnes, Commun. Phys. Lab. Univ. Leiden, *120b, 122b, 124c* (1911).

[2]J. Bardeen, L. N. Cooper, and J. R. Schrieffer, Phys. Rev. **108**, 1175–1204 (1957).

[3]M. Sigrist, *Introduction to Unconventional Superconductivity*, Lecture Notes Summer School.

[4]M. R. Norman, arXiv:1302.3176v2, 2013.

[5]D. van Delft, and P. Kes, Phys. Today **63**, 38 (2010).

[6]J. G. Bednorz, and K. A. Müller, Zeitschrift für Physik B Condensed Matter **64**, 189–193 (1986).

[7]Y. Kamihara, T. Watanabe, M. Hirano, and H. Hosono, J. Am. Chem. Soc. **130**, 3296–3297 (2008).

[8]D. N. Basov, and A. V. Chubukov, Nature Physics **7**, 272–276 (2011).

[9]Q. Si, R. Yu, and E. Abrahams, Nature Reviews Materials **1**, 16017 (2016).

[10]P. J. Hirschfeld, M. M. Korshunov, and I. I. Mazin, "Gap symmetry and structure of Fe-based superconductors.", Rep. Prog. Phys. **74**, 124508 (2011).

[11]D. D. Scherer, I. Eremin, and B. M. Andersen, arXiv:1608:03493v1, 2016.

[12]A. Chubukov, "Pairing Mechanism in Fe-based Superconductors", Annu. Rev. Condens. Matt. Phys. **3**, 57–92 (2012).

[13]P. J. Hirschfeld, Comptes Rendus Physique **17**, 197–231 (2016).

[14]J.-H. Chu, H.-H. Kuo, J. G. Analytis, and I. R. Fisher, Science **337**, 710–712 (2012).

[15]M. N. Gastiasoro, F. Bernardini, and B. M. Andersen, arXiv:1606.09495v1, 2016.

[16]R. M. Fernandes, A. V. Chubukov, and J. Schmalian, Nature Physics **10**, 97–104 (2014).

[17]D. J. Singh, Science and Technology of Advanced Materials **13**, 054304 (2012).

[18]Q. Wang, Y. Shen, B. Pan, Y. Hao, M. Ma, F. Zhou, P. Steffens, K. Schmalzl, T. R. Forrest, M. Abdel-Hafiez, X. Chen, D. A. Chareev, A. N. Vasiliev, P. Bourges, Y. Sidis, H. Cao, and J. Zhao, Nature Materials **15**, 159–163 (2015).

[19]A. Kreisel, S. Mukherjee, P. J. Hirschfeld, and B. M. Andersen, Phys. Rev. B **92**, 224515 (2015).

[20]H. Bruus, and K. Flensberg, *Many-Body Quantum Theory in Condensed Matter Physics* (Oxford University Press Inc., New York, 2004).

[21]https://fys.kuleuven.be/iks/nvsf/experimental-facilities/scanning-tunneling-microscopy.

[22]A. Altland, and B. Simons, *Many-Body Quantum Theory in Condensed Matter Physics*, 2th Edition (Cambridge University Press, Cambridge, 2010).

[23]L. Capriotti, D. J. Scalapino, and R. D. Sedgewick, Phys. Rev. B **68**, 014508 (2003).

[24]K. McElroy, G.-H. Gweon, S. Y. Zhou, J. Graf, S. Uchida, H. Eisaki, H. Takagi, T. Sasagawa, D.-H. Lee, and A. Lanzara, Phys. Rev. Lett. **96**, 067005 (2006).

[25]C.-L. Song, Y.-L. Wang, Y.-P. Jiang, L. Wang, K. He, X. Chen, J. E. Hoffman, X.-C. Ma, and Q.-K. Xue, Phys. Rev. Lett. **109**, 137004 (2012).

[26]C.-L. Song, Y.-L. Wang, P. Cheng, Y.-P. Jiang, W. Li, T. Zhang, Z. Li, K. He, L. Wang, J.-F. Jia, H.-H. Hung, C. Wu, X. Ma, X. Chen, and Q.-K. Xue, Science **332**, 1410–1413 (2011).

[27]T. Hanaguri, Y. Kohsaka, K. Iwaya, Y. Fu, T. Watashige, S. Kasahara, D. Watanabe, Y. Mizukami, T. Mikami, Y. Kawamoto, S. Kurata, H. Ikeda, T. Shibauchi, Y. Matsuda, A. Böhmer, T. Wolf, C. Meingast, and H. v. Löhneysen, *Quasi-particle interference and possible orbital order in FeSe*, .pptx from talk by T. Hanaguri at APS 14. Unpublished., 2014.

[28]P. Sprau, A. Kostin, A. Böhmer, P. Canfield, and J. S. Davis, *Nematic Order and Highly Anisotropic QPI in FeSe*, Preliminary results .pptx. Unpublished., 2016.

[29]D. Huang, T. A. Webb, C.-L. Song, C.-Z. Chang, J. S. Moodera, E. Kaxiras, and J. E. Hoffman, arXiv:1606.07057v1, 2016.

[30]E. P. Rosenthal, E. F. Andrade, C. J. Arguello, R. M. Fernandes, L. Y. Xing, X. C. Wang, C. Q. Jin, A. J. Millis, and A. N. Pasupathy, Nature Physics **10**, 225–232 (2014).

[31]L. Covaci, F. M. Peeters, and M. Berciu, Phys. Rev. Lett. **105**, 167006 (2010).

[32]M. Abramowitz, and I. A. Stegun, *Handbook of Mathematical Functions with Formulas, Graphs, and Mathematical Tables* (Dover, New York, 1970).

[33]A. Weisse, G. Wellein, A. Alvermann, and H. Fehske, Mod. Phys. **78**, 275 (2006).

[34]Y. Nagai, Y. Ota, and M. Machida, J. Phys. Soc. Jpn. **81**, 024710 (2012).

[35]R. M. Fernandes, and A. V. Chubukov, arXiv:1607.00865v2, 2016.

[36]H. Eschrig, and K. Koepernik, Phys. Rev. B **80**, 104503 (2009).

[37]S. Mukherjee, A. Kreisel, P. J. Hirschfeld, and B. M. Andersen, Phys. Rev. B **115**, 026402 (2015).

[38]Y. Suzuki, T. Shimojima, T. Sonobe, A. Nakamura, M. Sakano, H. Tsuji, J. Omachi, K. Yoshioka, M. Kuwata-Gonokami, T. Watashige, R. Kobayashi, S. Kasahara, T. Shibauchi, Y. Matsuda, Y. Yamakawa, H. Kontani, and K. Ishizaka, Phys. Rev. B **92**, 205117 (2015).

[39]M. D. Watson, T. K. Kim, L. Rhodes, M. Eschrig, M. Hoesch, A. A. Haghighirad, and A. I. Coldea, arXiv:1603.04545v2, 2016.

[40]B. M. Anderson, *Coexistence of Magnetic and Superconducting Order in the High-T_cMaterials*, Phd. Thesis in Physics, University of Copenhagen, 2004.

[41]A. Kreisel, Private Correspondence with A. Kreisel, Unpublished, 2016.

[42]J. Knolle, I. Eremin, A. Akbari, and R. Moessner, Phys. Rev. Lett. **104**, 257001 (2010).

[43]T.-M. Chuang, M. P. Allan, J. Lee, Y. Xie, N. Ni, S. L. Bud′ko, G. S. Boebinger, P. C. Canfield, and J. C. Davis, Science **327**, 181–184 (2010).

[44]A. M. Oleś, Phys. Rev. B **28**, 327–339 (1983).

[45]L. de Medici, *Weak and strong electronic correlations in Fe superconductors*, arXiv:1506.01678v1, 2015.

[46]D. Möckli, and E. V. L. de Mello, arXiv:1510.00167v1, 2015.

[47]S. Blundell, *Magnetism in Condensed Matter* (Oxford University Press, Oxford, 2001).

[48]P. J. Hirschfeld, D. Altenfeld, I. Eremin, and I. I. Mazin, Phys. Rev. B **92**, 184513 (2015).

[49]L. Zhu, W. A. Atkinson, and P. J. Hirschfeld, Phys. Rev. B **69**, 060503 (2004).

[50]C. Bena, Comptes Rendus Physique **17**, 302–321 (2016).

[51]T. Watashige, Y. Tsutsumi, T. Hanaguri, Y. Kohsaka, S. Kasahara, A. Furusaki, M. Sigrist, C. Meingast, T. Wolf, H. v. Löhneysen, T. Shibauchi, and Y. Matsuda, Phys. Rev. X **5**, 031022 (2015).

[52]M. J. Lawler, K. Fujita, J. Lee, A. R. Schmidt, Y. Kohsaka, C. K. Kim, H. Eisaki, S. Uchida, J. C. Davis, J. P. Sethna, and E.-A. Kim, Nature **466**, 347–351 (2010).

[53]I. Mazin, and J. Schmalian, "Pairing symmetry and pairing state in ferropnictides: Theoretical overview", Physica C: Superconductivity **469**, Superconductivity in Iron-Pnictides, 614–627 (2009).